

Symmetry and Optical Anisotropy
in CdSe/ZnSe Quantum Dots

Dissertation zur Erlangung des
naturwissenschaftlichen Doktorgrades
der Bayerischen Julius-Maximilians-Universität Würzburg

vorgelegt von
Tobias Kießling
aus Würzburg

Würzburg 2009

Eingereicht am 27.07.2009

bei der Fakultät für Physik und Astronomie

Gutachter der Dissertation:

1. Gutachter: Prof. Dr. W. Ossau
2. Gutachter: Prof. Dr. L. W. Molenkamp

Prüfer im Promotionskolloquium:

1. Prüfer: Prof. Dr. W. Ossau
2. Prüfer: Prof. Dr. L. W. Molenkamp
3. Prüfer: Prof. Dr. B. Trauzettel

Tag des Promotionskolloquiums: 29.10.2009

Doktorurkunde ausgehändigt am: ...

Parts of this thesis have been already published :

- S. Mahapatra, C. Schumacher, T. Kiessling, G. V. Astakhov, U. Bass, W. Ossau, J. Geurts and K. Brunner. *CdSe/ZnSe Quantum Dots formed by low temperature epitaxy an In-situ annealing: Properties and growth optimization*. Acta Phys. Pol. A 108, 769 (2005)
- G. V. Astakhov, T. Kiessling, A. V. Platonov, T. Slobodskyy, S. Mahapatra, W. Ossau, G. Schmidt, K. Brunner and L. W. Molenkamp. *Circular-to-linear and linear-to-circular conversion of optical polarization by semiconductor quantum dots*. Phys. Rev. Lett. 96, 027402 (2006)
Selected for Virtual Journal of Nanoscale Science & Technology, 30th January 2006, nanomagnetism and spintronics (<http://www.vjnano.org/>).
- T. Kiessling, G. V. Astakhov, A. V. Platonov, T. Slobodskyy, S. Mahapatra, W. Ossau, G. Schmidt, K. Brunner and L. W. Molenkamp. *Optical anisotropy of CdSe/ZnSe quantum dots*. Phys. Stat. Sol. (c) 3, pp. 912-915 (2006)
- A. V. Platonov, T. Kiessling, G. V. Astakhov, A. A. Maksimov, A. V. Larionov, D. R. Yakovlev, T. Slobodskyy, W. Ossau, G. Schmidt, K. Brunner, M. Bayer and L. W. Molenkamp. *Energy relaxation in CdSe/ZnSe quantum dots under the strong exciton-phonon coupling regime*. Phys. Stat. Sol. (c) 3, pp. 924-927 (2006)
- S. Mahapatra, K. Brunner, C. Schumacher, T. Kiessling, G. V. Astakhov, U. Bass, E. Margapoti, W. Ossau, J. Geurts, L. Worschech, A. Forchel and L. W. Molenkamp. *Comparative study of self-assembled CdSe/ZnSe quantum dots grown by variants of conventional MBE*. Phys. Stat. Sol. (c) 3, pp. 928-932 (2006)
- T. Kiessling, A. V. Platonov, G. V. Astakhov, T. Slobodskyy, S. Mahapatra, W. Ossau, G. Schmidt, K. Brunner and L. W. Molenkamp. *Anomalous in-plane magneto-optical anisotropy of self-assembled quantum dots*. Phys. Rev. B 74, 041301R (2006)
Selected for Virtual Journal of Nanoscale Science & Technology, 24th July 2006, quantum coherence, computing, and information storage (<http://www.vjnano.org/>).
- T. Kiessling, A. V. Platonov, G. V. Astakhov, S. Mahapatra, T. Slobodskyy, W. Ossau, G. Schmidt, K. Brunner and L. W. Molenkamp. *Phonon replica fine structure in Cd/Se quantum dots*. Proc. 14th Int. Symp. 'Nanostructures: Physics and Technology' pp. 269, St. Petersburg, Russia, June 26-30, 2006.

- A. V. Platonov, T. Kiessling, G. V. Astakhov, T. Slobodskyy, S. Mahapatra, W. Ossau, G. Schmidt, K. Brunner, L. W. Molenkamp. *Anomalous in-plane magneto-optical anisotropy of self-assembled quantum dots*. Proc. 14th Int. Symp. 'Nanostuctures: Physics and Technology' pp.146-147, St.Petersburg, Russia, June 26-30, 2006.
- S. Mahapatra, T. Kiessling, E. Margapoti, G. V. Astakhov, W. Ossau, L. Worschech, A. Forchel and K. Brunner. *Formation mechanism and properties of CdSe quantum dots on ZnSe by low temperature epitaxy and in-situ annealing*. Appl. Phys. Lett. 89, 043102 (2006)
- S. Mahapatra, T. Kiessling, E. Margapoti, G. V. Astakhov, W. Ossau, L. Worschech, A. Forchel and K. Brunner. *Layer-by-layer growth and island formation in CdSe/ZnSe heteroepitaxy*. J. Crystal Growth 301, 00310 (2007)
- T. Kiessling, G. V. Astakhov, A. V. Platonov, S. Mahapatra, T. Slobodskyy, W. Ossau, G. Schmidt, K. Brunner and L. W. Molenkamp. *Optical studies of structural and magnetic anisotropies in epitaxial CdSe/ZnSe quantum dots*. Phys. Stat. Sol. (c) 4, 3324 (2007).
- S. Mahapatra, T. Kiessling, E. Margapoti, G. V. Astakhov, J. Renner, U. Bass, C. Bougerol, T. Schmidt, A. Bendounan, F. Schmitt, C. Schumacher, L. Worschech, W. Ossau, J. Geurts, L. W. Molenkamp, F. Reinert, A. Forchel and K. Brunner. *CdSe/ZnSe heteroepitaxy: Aspects of growth and self organization of nanostructures*. Phys. Stat. Sol. (c) 4, 3129 (2007).

Further parts of this Thesis are currently prepared for publication.

Further publications under participation of the author :

- G. V. Astakhov, T. Kiessling, D. R. Yakovlev, E. A. Zhukov, M. Bayer, W. Ossau, B. P. Zakharchenya, G. Karczewski, T. Wojtowicz and J. Kossut. *Nanosecond spin memory of electrons in CdTe/CdMgTe quantum wells*. Phys. Stat. Sol. (b) 243, pp. 858-862 (2006).
- H. Hoffmann, G. V. Astakhov, T. Kiessling, W. Ossau, G. Karczewski, T. Wojtowicz, J. Kossut and L. W. Molenkamp. *Optical spin pumping of modulation doped electrons probed by a two-color Kerr rotation technique*. Phys. Rev. B 74, 071407 (2006)
Selected for Virtual Journal of Nanoscale Science & Technology, 4th September 2006, nanomagnetism and spintronics (<http://www.vjnano.org/>).
- G. V. Astakhov, R. I. Dzhioev, K. V. Kavokin, V. L. Korenev, M. V. Lazarev, M. N. Tkachuk, Yu. G. Kusrayev, T. Kiessling, W. Ossau, and L. W. Molenkamp. *Suppression of electron spin relaxation in Mn-doped GaAs*. Phys. Rev. Lett. 101, 076602 (2008).
- G. V. Astakhov, H. Hoffmann, V. L. Korenev, T. Kiessling, J. Schwittek, G. M. Schott, C. Gould, W. Ossau, K. Brunner, and L. W. Molenkamp. *Nonthermal Photocoercivity effect in a low doped (Ga,Mn)As ferromagnetic semiconductor*. Phys. Rev. Lett. 102, 187401 (2009).

Contents

| | |
|---|-----------|
| Zusammenfassung | 1 |
| Summary | 5 |
| 1 Introduction | 9 |
| 2 Fundamental properties of semiconductor quantum dots | 17 |
| 2.1 Discrete energy spectrum of quantum dots | 17 |
| 2.2 Properties of quantum confined solid state systems | 20 |
| 2.3 Modeling of real quantum dots | 24 |
| 3 Optical Properties of epitaxial semiconductor quantum dots | 29 |
| 3.1 Optical properties of direct gap zinc-blende type compound semiconductors | 30 |
| 3.1.1 Crystal symmetry and band structure | 31 |
| 3.1.2 Radiative band-to-band recombination at $k = 0$ | 34 |
| 3.1.3 Excitons and the concept of Poincaré and Bloch spheres | 36 |
| 3.2 Excitons confined to epitaxial QD nanostructures | 39 |
| 3.2.1 Neutral excitons in magnetic fields | 43 |
| 3.2.2 Exciton complexes in the absence of magnetic field | 44 |
| 4 Quantum dot fabrication | 49 |
| 4.1 General remarks on molecular beam heteroepitaxy | 50 |
| 4.2 Self-assembled quantum dot growth | 51 |
| 4.3 Growth variants of CdSe/ZnSe quantum dots | 55 |
| 4.3.1 Conventional MBE growth | 55 |
| 4.3.2 Low temperature epitaxy and in-situ annealing | 57 |
| 4.4 Conventional MBE versus low temperature epitaxy QD luminescence | 60 |
| 5 Electronic Properties of shallow CdSe/ZnSe Quantum Dots | 63 |
| 5.1 Electronic structure and composition | 64 |
| 5.2 Exciton-phonon interaction | 71 |
| 5.2.1 Experimental results | 72 |
| 5.2.2 Analysis and discussion | 75 |

| | | |
|----------|---|------------|
| 6 | Optical anisotropy of CdSe/ZnSe quantum dots | 79 |
| 6.1 | Optical anisotropy in the absence of magnetic fields | 80 |
| 6.1.1 | Optical polarization anisotropy and polarization conversion | 80 |
| 6.1.2 | Optical polarization alignment and ensemble symmetry | 86 |
| 6.2 | Optical anisotropy induced by in-plane magnetic fields | 89 |
| 6.2.1 | Experimental results | 89 |
| 6.2.2 | Qualitative discussion | 94 |
| 6.2.3 | Quantitative analysis | 98 |
| 6.2.4 | Conclusions | 107 |
| 7 | Conclusions and Outlook | 109 |
| | Appendix | 113 |
| A | Setup and experimental methods | 113 |
| A.1 | Experimental setup | 113 |
| A.2 | Optical polarization modulation spectroscopy | 115 |
| B | Angular Momentum Operators | 117 |
| C | List of Abbreviations | 119 |
| | Bibliography | 121 |

Zusammenfassung

Halbleiter Quantenpunkte (engl. **Q**uantum **D**ots - QDs) haben in den letzten zehn Jahren ein immenses Interesse sowohl in der Grundlagen- als auch der anwendungsorientierten Forschung erregt, was sich maßgeblich aus ihrer möglichen Nutzung als Fundamentalbausteine in neuartigen, physikalisch nicht-klassischen Bauelementen ergibt. Ihre vermutlich einfache Integrierbarkeit in bereits bestehende Halbleitertechnologien lässt sie in dem Ruf stehen, kosteneffizient auf Massenproduktion skalierbar zu sein, und hat ihnen auf diese Weise einen Platz unter den Topkandidaten für eine große Zahl von aktuell erforschten technischen Entwürfen zur Quantenlogik und Quanteninformationsverarbeitung eingebracht. Diese beinhalten insbesondere auch die viel gepriesene Nutzung von QDs als gezielt ansteuerbare Lichtquellen zur Erzeugung einzelner Paare polarisationsverschränkter Photonen, was einen Kernbaustein in den momentan intensiv erforschten optischen Quantenkryptographiekonzepten darstellt.

Ein ausgesprochenes Hindernis für eine derartige Nutzung stellen die in allen aktuell verfügbaren Halbleiterquantenpunkten intrinsisch vorhandenen, ausgeprägten Asymmetrien dar. Diese sind eine Begleiterscheinung, die sich aus den selbstorganisierten Wachstumsmethoden der QDs ergibt und die sich in verschiedenen Gestalten, wie Formasymmetrie oder inhomogenen Verspannungsverhältnissen innerhalb der QDs und den damit einhergehenden piezo-elektrischen Feldern, manifestiert. Im Gegenzug verursachen jene Asymmetrien deutliche Anisotropien in den optischen Eigenschaften der QDs, wodurch das optische Ansprechverhalten klassisch beschreibbar wird. Aus Sicht der anwendungsorientierten Forschung stehen Asymmetrien daher im Ruf ungewollte Nebeneffekte zu sein und es wird mit großem Aufwand daran geforscht, diese unter Kontrolle zu bringen. Für die Grundlagenforschung stellen anisotrope QDs jedoch ein sehr interessantes Modellsystem dar, da an ihnen fundamentale Quantenphysik beobachtbar ist, wobei anders als in Atomen die einschnürenden Potentiale nicht zwangsläufig zentralsymmetrisch sein müssen, was, wie im Rahmen dieser Arbeit gezeigt werden wird, zu neuartiger und interessanter Physik führen kann.

Das Materialsystem der Wahl für die in der vorliegenden Arbeit durchgeführten Untersuchungen waren selbstorganisierte CdSe/ZnSe QDs. Diese Wahl begründet sich durch die folgenden beiden Aspekte: Zunächst lassen sich CdSe/ZnSe QDs mit ausgezeichneten optischen Eigenschaften herstellen, was eine Grundvoraussetzung für optische Experimente darstellt. Weiterhin sind in II-VI Verbindungshalbleitern auf Grund des hohen

polaren Charakters der Bindungen die optischen Anisotropien infolge verschiedener Asymmetrien deutlich ausgeprägter als in den jeweiligen III-V oder Gruppe IV Gegenständen. Im Gegensatz zu III-V Halbleitern, in denen die Selbstorganisation von QDs gut durch den Stranski-Krastanow Wachstumsmodus beschrieben ist, sind die Feinheiten der QD Ausbildung in II-VI Legierungen jedoch nicht in letzter Konsequenz geklärt. Für die Zwecke dieser Dissertation wurden daher verschiedene QDs, welche sich bei zwei unterschiedlichen Wachstumsvarianten von Molekularstrahlepitaxie ausbilden, untersucht.

Um eine klare Verknüpfung zwischen den optisch beobachteten Anisotropien und den durch die Wachstumsbedingungen begründeten Asymmetrien in den QDs zu ermöglichen, wird zunächst eine Zusammenfassung aller zur Verfügung stehender struktureller und morphologischer Daten der QDs gegeben. Diese setzen sich aus Untersuchungen mittels Röntgenbeugung, Rasterkraftmikroskopie, hochauflösender Transmissionselektronenmikroskopie und resonanter Ramanstreuung zusammen. Durch ausführliche Messungen mit Photolumineszenz- (engl. **Photoluminescence** - PL) und Photolumineszenzanregungsspektroskopie (engl. **Photoluminescence excitation** - PLE) ergibt sich schließlich ein klares Bild sowohl der Struktur der elektronischen Zustände der in den QDs gebundenen Exzitonen als auch ihrer Relaxation über diese. Dabei zeigt sich, dass in sehr kleinen, stark bindenden QDs die k -Vektor Erhaltung vollständig aufgehoben ist. Die so mögliche Wechselwirkung der Exzitonen mit einem Kontinuum von Phononzuständen sorgt für einen schnellen und effizienten Einfang der Exzitonen in die QDs selbst für Anregungsbedingungen energetisch weit über deren Grundzustand. Es wird gezeigt, wie auf diese Weise ein alternativer Relaxationskanal zu den bekannten Auger-artigen Elektron-Loch Streuprozessen entsteht, anhand dessen die schnelle Relaxation von gebundenen Löchern sowie die generelle Abwesenheit eines "Phonon-Flaschenhals" in der exzitonischen Energielaxation verstanden werden kann.

Auf der Basis dieser Ergebnisse wird dann die Anisotropie des linearen Polarisationsgrades in der Lumineszenzstrahlung (im Folgenden kurz: optische Anisotropie) der an CdSe/ZnSe-QDs gebundenen Exzitonen untersucht, was mit Hilfe winkel- und polarisationsaufgelöster PL durchgeführt wird. Es wird gezeigt, dass die Elektron-Loch Austauschwechselwirkung in asymmetrischen QDs zu einer effektiven Umwandlung linearer in zirkulare Polarisationsanteile und umgekehrt führt. Die experimentellen Befunde lassen sich erfolgreich im Rahmen eines Exziton-Pseudospinformalismus, der auf der durch die Austauschwechselwirkung induzierten Feinstruktur der hellen Exzitonenzustände basiert, beschreiben. Dieser belegt zudem eindeutig, dass die beobachtete Polarisationsumwandlung ein Äquivalent unter Dauerstrichanregung zu den in der Zeitdomäne beobachteten sogenannten "quantum-beats" zwischen den hellen Exzitonenzuständen darstellt. Diese Ergebnisse legen nahe, dass QDs funktionelle Bauelemente in hochintegrierten rein optischen Architekturen jenseits der viel diskutierten nichtklassischen Konzepte darstellen können, insbesondere als optische Polarisationskonverter und/oder -modulatoren.

Im nächsten Schritt wird der Exziton-Pseudospinformalismus in Untersuchungen zur optischen Ausrichtung in QDs genutzt und gezeigt, wie auf diese Weise die anders nicht

direkt messbare Symmetrieverteilung eines Ensembles von QDs detektiert werden kann. Diese Messungen stellen ein wertvolles Bindeglied zwischen optischen und strukturellen Untersuchungen dar, da sie einen direkten experimentellen Zugang zum mit topologischen Methoden nicht einsehbar Anordnungsverhalten eingekapselter QDs liefern.

Im letzten Teil der Arbeit wird dann die optische Anisotropie unter Anlegung eines Magnetfeldes in der QD-Ebene untersucht. Dabei wird beobachtet, dass die Achse der linearen Polarisation der Lumineszenzstrahlung entweder entgegengesetzt zur Magnetfeldrichtung in der Probenebene rotiert oder fest entlang einer gegebenen kristallographischen Achse orientiert ist. Eine qualitative Auswertung der Ergebnisse auf der Basis des exzitonischen Pseudospin-Hamiltonian belegt, dass diese Polarisationsanteile durch isotrope und anisotrope Beiträge des Schwerloch Zeeman Terms begründet werden. Dabei wird gezeigt, dass die anisotropen Anteile für ein kritisches Magnetfeld von $B_C = 0,4$ T gerade die forminduzierten uni-axialen Polarisationsanteile kompensieren, und so ein optisches Verhalten resultiert, das man für hochsymmetrische QDs erwarten würde.

Zur umfassenden quantitativen Beschreibung wurde der vollständige $\mathbf{k}\cdot\mathbf{p}$ -Hamiltonian in der Basis der Schwerlohexzitonzustände numerisch ausgewertet und anhand dessen die optische Polarisation als Funktion der Magnetfeldstärke und -orientierung berechnet. Die Modellrechnungen stimmen mit die gemessenen Daten im Rahmen der experimentellen Unsicherheit mit einem jeweils probenspezifischen Parametersatz quantitativ überein. Dabei wird gezeigt, dass ein Ensemble von QDs ein optisches Signal, das man für hochsymmetrisches QDs erwarten würde, erzeugen kann *ohne* dass eine Symmetrisierung der (in Abwesenheit externer Felder) hellen Exzitonzustände stattfindet, wie sie für nicht-klassische Anwendungen notwendig ist. Die sich daraus ergebenden Folgerungen belegen zweifelsfrei, dass Konzepte, die Magnetfelder in der Probenebene zur Symmetrisierung des optischen Signals nutzen, mindestens die vier stark durchmischten Schwerlohexzitonzustände berücksichtigen müssen und eine Beschreibung, die nur die beiden hellen Exzitonzustände in Abwesenheit magnetischer Felder beinhaltet, zu kurz greift. Im Kontext der kontrovers geführten Diskussion bezüglich aktueller experimenteller Studien zur Erzeugung polarisationsverschränkter Photonen in asymmetrischen QDs [Ste06b, Lin06, Gil07] ist daher zu verstehen, dass von solch einer vereinfachten Beschreibung nicht a priori erwartet werden kann, verlässliche Ergebnisse in Bezug auf exzitonische Bellzustände zu erzeugen.

Summary

Semiconductor Quantum Dots (QDs) have been attracting immense interest over the last decade from both basic and application-orientated research because of their envisioned use as fundamental building blocks in non-classical device architectures. Their presumable ease of integration into existing semiconductor technology has bought them the reputation of being cost-efficiently scalable and renders them a place among the top candidates in a wide range of proposed quantum logic and quantum information processing schemes. These include the highly acclaimed use of QD as triggered sources of single pairs of entangled photons, which is a key ingredient of most of the intensively investigated optical quantum cryptography operations.

A big obstacle towards these goals are the pronounced asymmetries that are intrinsically present in all currently available semiconductor QD systems. They are a natural by-product that stems from the employed self-assembled growth methods and manifest in various forms such as shape-asymmetry, inhomogeneous strain distribution within the QD and concomitant piezo-electric fields. These asymmetries in return give rise to distinct anisotropies in the optical properties of QDs, which in fact render their optical response classic. For device oriented research these anisotropies are therefore typically considered unwanted and actively researched to be controlled. They are, however, interesting from a fundamental point of view, as anisotropic QDs basically provide a testbed system for fundamental atom-like quantum physics with non-centrosymmetric potentials. As shall be shown in the current work, this gives rise to novel and interesting physics in its own right.

The material system of choice for the investigations performed in the frame of this *Thesis* were self-assembled CdSe/ZnSe QDs. The reason for this choice is twofold. First, CdSe/ZnSe QDs can be grown with excellent optical quality, which is a prerequisite for optical studies. Second, due to the polar nature of II-VI compound semiconductors, optical anisotropies induced by various asymmetries are more pronounced than in their III-V or element IV counterparts. Unlike in the III-V materials, where the self-organization of QDs is well described by the Stranski-Krastanow growth mode, the peculiarities of the QD formation are not entirely clear in II-VI alloys. For the purposes of the current work QDs emerging from two variants of Molecular Beam Epitaxy (MBE) growth were studied.

In order to establish a clear connection between the optically observed anisotropies and the growth induced asymmetries in the QDs we start out by summarizing all avail-

able structural and morphological studies that were performed on the resultant QDs, including x-ray diffraction, atomic force microscopy, high resolution transmission electron microscopy and resonant Raman scattering. Extensive investigations by Photoluminescence (PL) and Photoluminescence Excitation (PLE) spectroscopy hence detail the resultant electronic structure of excitons confined to the above QDs as well as their energy relaxation across the latter. We find that for these small-sized strongly confining QDs k -vector conservation is entirely relaxed, which enables interaction of the excitons with a continuum of phonons and explains fast and efficient exciton capture by the QDs, even for excitation conditions far above the ground state. We demonstrate how this provides an alternative fast relaxation channel to Auger-like electron-hole scattering, that may also explain fast hole relaxation and adds to the understanding of the absence of a phonon bottleneck in the energy relaxation in these type of QDs.

With the above analysis as a backbone we turn to the investigation of the optical anisotropy of the radiative recombination of excitons confined to CdSe/ZnSe QDs. This is done by angle-dependent polarization-resolved PL. We demonstrate experimentally that the electron-hole exchange interaction in asymmetric QDs gives rise to an effective conversion of the optical polarization from linear to circular and vice versa. The experiment is successfully modeled in the frame of an exciton pseudospin-formalism that is based on the exchange induced finestructure splitting of the radiative excitonic states and unambiguously proves that the observed polarization conversion is the continuous-wave equivalent to quantum beats between the exchange split states in the time domain. These results indicate that QDs may offer extended functionality beyond non-classical light sources in highly integrated all-optical device schemes, such as polarization converters or modulators.

In a further extension we apply the exciton pseudospin-formalism to optical alignment studies and demonstrate how these can be used to directly measure the otherwise hidden symmetry distribution over an ensemble of QDs. This kind of measurement may be used on future optical studies in order to link optical data more directly to structural investigations, as it yields valuable information on capped QDs that cannot be looked at directly by topological methods.

In the last part of this work we study the influence of an in-plane magnetic field on the optical anisotropy. We find that the optical axis of the linear polarization component of the photoluminescence signal either rotates in the opposite direction to that of the magnetic field or remains fixed to a given crystalline direction. A qualitative theoretical analysis based on the exciton pseudospin Hamiltonian unambiguously demonstrates that these effects are induced by isotropic and anisotropic contributions to the heavy-hole Zeeman term, respectively. The latter is shown to be compensated by a built-in uniaxial anisotropy in a magnetic field $B_C=0.4$ T, resulting in an optical response that would be expected for highly symmetric QDs.

For a comprehensive quantitative analysis the full heavy-hole exciton \mathbf{k}, \mathbf{p} -Hamiltonian is numerically calculated and the resulting optical polarization is modeled. The model is

able to quantitatively describe all experimental results using a single set of parameters. From this model it is explicitly seen that a optical response characteristic for high symmetry QDs may be obtained from an ensemble of asymmetric QDs *without* a crossing of the zero-field bright exciton states, which was required for application of QDs in non-classical light sources. It is clearly demonstrated that any scheme using in-plane magnetic fields to symmetrize the optical response has to take into account at least four optically active states instead of the two observed in the absence of magnetic fields. These findings may explain some of the major disagreement on recent entanglement studies in asymmetric QDs [Ste06b, Lin06, Gil07], as models that do not take the above result into account cannot be a priori expected to provide reliable results on excitonic Bell states.

Chapter 1

Introduction

Information age is the generally accepted term to describe the current economic state of Western society, which highlights like no other expression today's crucial influence of information technology on everyday life. The basis of virtually all modern information-related devices is semiconductor technology, displaying an incredible record of successes over the last 50 years. Its main driving force has been and still is progressive miniaturization by steadily increasing the number of circuits per unit area. Thus we have reached an incredible degree of integration, with today's microchips amassing several hundred million circuits on an area of only a few mm^2 .

This ever-increasing demand for size reduction was naturally accompanied by the technological development of highly sophisticated growth and patterning techniques, which effectively enable fabrication of devices on the nanometer scale. As of November 2007, mass production of chips employing 45 nm technology is standard, with 45 nm referring to the average half pitch of a memory cell, and the international technology roadmap of semiconductors schedules the arrival of the 32 nm standard for the 2009-2010 timeframe[Ste06a]. The establishment of powerful fabrication methods of complex semiconductor nanostructures was a prerequisite for modern semiconductor physics, which is highly focused on the physics of systems of reduced dimensionality. This is a nice display of the mutual interplay of basic research and applied technology, as of course results of half a century of semiconductor physics research form the very heart of today's semiconductor technology.

It is noteworthy that the evolution of information technology was anything but the result of an a forehand planned development. In fact, the path to many of today's achievements was full of detours and unforeseen turns, as more and more insight into the physics of solid state systems was gathered. Especially since most of today's studies are driven by application, the importance of basic research must not be underestimated. Recent research on the physics of truly zero dimensional objects - Quantum Dots (QDs) - should be regarded in the same light. With a plethora of potentially groundbreaking applications predicted, among those the highly acclaimed use as fundamental building block for quantum logic devices, in analogy to classical bits dubbed qubits, the interest of device research in QDs is immense. Yet QDs are a lot more. They represent a unique model system, in

which true quantum mechanical effects can be explored and, moreover, in contrast to real atoms, are tunable. Furthermore, due to the interplay with their solid state environment, completely new physics that are not observable at all in their atomistic counterparts can arise in QDs.

Research on fully confined systems: Experimental prerequisites

In this light it is worthwhile to briefly survey the course to modern research on low dimensional systems and true quantum objects. Being the cornerstone of modern studies of quantum-confined systems, the physics of bulk semiconductors have reached a thorough understanding, going a long way from Bloch's initial introduction of the electronic bandstructure concept for an ideal crystalline solid in 1928[Blo28] and culminating in the groundbreaking invention of the transistor by Bardeen, Shockley and Brattain in 1950[Bri97]. By the late 1950s the idea of studying systems of reduced dimensionality became popular among semiconductor physicists, but the initial work remained purely theoretical due to the lack of working samples on the nanometer scale, which would be able to show effects of size quantization. In order to experimentally observe the latter, almost perfectly reflecting surfaces or interfaces are required for carriers, which at that time were quite simply not yet available. Even though vacuum deposition techniques allowed fabrication of ultra-thin layers of only a few nanometers already in the 1950s, the high interface roughness of these layers essentially ruled out experimental work with regard to low dimensional systems.

Interestingly, some of the concepts that would later turn out to be very successful in non-3D systems were nevertheless already conceived in the early 1960s, despite the lack of experimental evidence. In 1962 Keldysh considered the impact of intense ultrasonic waves on the electron spectrum of solid state systems[Kel62]. In this work he elaborated the motion of electrons in a superimposed periodic potential having a much larger periodicity than the crystal lattice and predicted the appearance of additional forbidden zones, i. e. effective minizones. Directly connected to these ideas is the first notion of what later would come to be known as Quantum Cascade Lasers (QCLs), which moreover also holds testimony as to what should be considered realistic timescales from first scientific idea to market introduction. QCLs were already conceived in 1971 by Kazarinov and Suris [Kaz71], but it took more than 20 years until they were first experimentally demonstrated [Fai94]. Though still facing technological challenges even today, mostly arising from heat dissipation, QCLs are nowadays used as infra-red lasers in the range from 2.7 to 250 μm [Tse06] in a wide range of applications.

With the availability of Molecular Beam Epitaxy (MBE) and somewhat later Metal Organic Chemical Vapor Deposition (MOCVD) semiconductor physics fully embarked on research of systems of reduced dimensionality. With these growth methods introduced in the late 1960s size quantization effects became experimentally accessible. Consequently, in the 1970s and 1980s semiconductor physics were characterized by research on two-

dimensional systems, laying down a long and impressive record of newly observed effects. Most popular among those (at least from the Wuerzburg perspective and here especially from the department of the Experimentelle Physik 3) are certainly the observation of the integer Quantum Hall Effect by von Klitzing in 1980 [vK80] and a little later the fractional Quantum Hall Effect by Tsui, Störmer and Gossard in 1982 [Tsu82]. By the end of the 1980s a decent understanding of quantum wells and superlattices had been achieved and the attention shifted towards systems of further reduced dimensionality - Quantum Wires (QWr) and ultimately Quantum Dots (QDs).

In 1986, Reed and his coworkers [Ree86] reported for the first time on fabrication of all-semiconductor integrated QDs by lithographic patterning and etching of Quantum Wells (QW). Interestingly, this does not really mark the date of arrival of spatially fully confined quantum objects in the physics world. In fact, QDs had been introduced in the form of nano-sized CdSe or CdS inclusions in glass matrices by Rocksby already in 1932 [Roc32] and had been available as sharp cut-off filters in commercial optics for half a century. It was, however, not before 1985 that Ekimov and Onushenko demonstrated quantum confinement effects in such a system experimentally [Eki85]. Yet, the capability of introducing QDs into an all-semiconductor environment immediately rose the subject to a completely new level, as the expected ease of integration of such objects into existing semiconductor technology opened the door for a complete new class of potential applications.

Consequently, initial work concentrated on research on QD fabrication, whereby the various methods used can loosely be classified into two categories. The first one is chemical synthesis of semiconductor crystallites on the nanometer scale, which attracted high interest beginning from the late 1980s [Bru91]. The ability to make these nanocrystallites water soluble and target them to specific biomolecules in addition to their often superior optical properties has gained these QDs a reputation of highly perspective candidates for *in-vivo* fluorophores in medical or more general biological investigations [Med05]. The full potential of these materials is just about to be realized. In the context of semiconductor technology chemically synthesized nanoparticles are usually of minor importance due to the organic shells in which they are enclosed, which imposes serious complications upon integrating the nanocrystals into a semiconductor environment.

The second class of fabrication relies on epitaxial growth and processing of semiconductor heterostructures. Here, the early efforts were based on the aforementioned lithographic patterning and etching of QWs or selective intermixing of QWs [Wer89]. Over the last 15 years so called *self-organized* or *self-assembled* methods have become popular among growers. If the lattice constant of the substrate and the crystallized material deviate considerably, only a few atomic monolayers will deposit in the form of an epitaxial, heavily strained layer with its lattice constant equal to that of the substrate material. Further material deposition exceeding a critical thickness, depending on the material specifics, will cause a breakdown of the ordered layer and result in the spontaneous creation of randomly distributed islands, in order to relieve the strain. The average size and shape of

such formed islands depends on the material system and the growth details, which are still subject to recent research of semiconductor nanostructures [Mah07c] (this will be further detailed in chapter 4).

There are multiple reasons as to why self-organized growth is particularly attractive. First off, no complicated post growth treatment and chemical processing are required, which enables time- and cost-effective growth. Several well studied material systems meet the requirements of self-assembled QD fabrication, among those Ge on Si (001) substrates, which is by far the best studied semiconductor material. Further, a variety of combinations of III-V and II-VI compound semiconductors has proven to be suitable for self-assembly, e. g. InAs on GaAs, CdTe on ZnTe or CdSe on ZnSe. In all of the above, small and most important defect free (i. e. crystallographically coherent) QDs have been successfully realized. Their superior optical quality, allowing for both in depth research as well as high performance optical application, together with their ease of integration into existing semiconductor technology is unique to the current day.

It is therefore, that QDs have been and still are both in the focus of fundamental research, for the powerful model system that they are, as well as applied research, where initially possible application in laser systems stood out. In 1982 Arakawa and Sakaki pointed out that lasers using QD active layers should have a less temperature sensitive performance and further should not show degradation at elevated temperatures [Ara82]. Moreover, Asada *et al.* predicted in 1986 that QD lasers should exhibit strongly reduced current thresholds and increased differential gain, simply put more efficient laser operation [Asa86]. The early experiments on QDs consequently concentrated mostly on their optical properties. This work, performed in the 1990s elucidated important aspects such as the internal energetic structure of real QDs, its dependence on the shape, strain, external magnetic and electric fields, binding of exciton complexes and their rich internal structure and interaction of the latter with lattice phonons. Comprehensive reviews on this studies are given by U. Woggon (chemically synthesized nanocrystals) [Wog97] and D. Bimberg *et al.* (epitaxially grown QDs) [Bim99].

Recent topics: Spin phenomena and qubits

With the 21st century closing in, the center of gravity of the research on QDs shifted to spin-related effects of carriers confined to QDs. This development takes us somewhat back to where we started this introduction. There is a fundamental lower limit to the degree of miniaturization of the current technology imposed by quantum nature of all matter. It is further just a matter of simple Algebra to realize that it is only a question of time, and probably not in the distant future, until this barrier is reached. With this in mind it is all-evident that *some* disruptive technology will be required at some point to maintain or even increase the steady pace at which information technology is developing. Among the many discussed possibilities are several which propose to encode the spin degree of freedom of elemental particles, itinerant or localized, as information carriers. This so-called field

of *spintronics* is currently taking huge efforts to establish ways of manipulating spins in the frame of integrated devices much like the classical electron charge in old-fashioned circuits [Wol01]. Other proposals are even more far-reaching suggesting to directly use the quantum nature of spins in what is referred to as quantum computation or quantum information processing [Nie00]. While in fact little is known about the full potential of such architectures, it is established that the parallelism of quantum logic operations would enable the implementation of algorithms that may outdo their classical counterparts by a large margin. The maybe most famous example of such an algorithm is the one proposed by Alan Shor, which addresses the renowned problem of prime factoring [Sho94] and demonstrates that this task would be polynomial in time as opposed to exponential in a classical architecture.

In 1998, D. Loss and D. P. DiVincenzo proposed a qubit-scheme in which the spin of electrons confined to QDs is used as the fundamental building block [Los98]. As it was soon established that spin coherence could be extremely long-lived in epitaxial QDs [Sch03b, Mac04], this work triggered a surge of studies on coherent control of spins confined to QDs. Li *et al.* finally demonstrated an all-optical quantum gate in a semiconductor QD [Li03] based on coherent optical control of a biexciton confined to a single QD. While their scheme is a mere demonstrator and should be considered rather a proof-of-concept than a real device proposal, it nevertheless is a highly important result for two reasons. First off, it *experimentally* verifies that non-classical logic operations can indeed be performed by QDs. Further, it proves the feasibility of all-optical coherent control schemes.

This latter point is most interesting, as QDs have also been proposed as sources of non-classical photons *on demand* by O. Benson and co-workers, using the so-called biexciton cascade as key ingredient [Ben00]. Both schemes rely on the fact that optical transitions in QDs are sequential, which can give rise to correlated states of the emitted photons. In fact, the optical polarization state of a photon emitted upon radiative recombination of excitons, the fundamental optical two-particle excitation in a QD, and the exciton spin state are naturally intertwined. Vice versa, by appropriately choosing the optical polarization state of an exciting photon it is possible to set the spin state of the exciton, which is ultimately why all-optical schemes are so powerful. To exploit the full potential of these methods it is, however, inherently necessary to achieve a high degree of control on the energetic finestructure of the resulting exciton states.

The exciton energetic structure itself sensitively depends on the exact chemical composition, the shape and the crystal environment of the confining QD. In particular deviations from high symmetry are known to have considerable influence on the exciton energies and give rise to pronounced optical anisotropies. While this is a well established experimental fact, exactly how the crystal asymmetry affects the optical anisotropy has so far not really been studied thoroughly. As any scalable scheme that uses QDs as active elements will require this knowledge, this information is of fundamental relevance. It is further of key interest for basic research on the fundamental properties of 0D semiconductor heterostructures.

This Thesis

The aim of this *Thesis* is to explore the interplay of QD optical properties, their physical shape and their crystal environment. It is investigated how external magnetic fields could be used to gain control over the optical properties of low-symmetric epitaxial QDs. This is done by careful studies on the optical anisotropies inevitably present in all currently available QD-systems. For that purpose, CdSe/ZnSe QDs grown by different variants of molecular beam epitaxy are investigated. The reason for this choice is twofold. First, CdSe/ZnSe QDs are of excellent optical quality, such that optical methods are an ideal tool for studies on their physical properties. Second, they are known to exhibit pronounced asymmetries in shape, which due to the polar nature of II-VI compound semiconductor materials is expected to have an even greater impact on the optical anisotropy than in their III-V or IV-IV counterparts. The outline of this *Thesis* is as follows:

In **Chapter 2** the fundamental properties of epitaxial semiconductor QDs grown from semiconductors of cubic symmetry are discussed. It is conceptually motivated how the quantum-confined energetic structure arises from the bulk band structure and a brief introduction to the current state of the theoretic modeling of real QDs is given.

Chapter 3 details the optical properties of epitaxial QDs of reduced symmetry. This is done from fundamental symmetry considerations, starting from cubic bulk semiconductors and consequently evolving the situation encountered in low-symmetry QDs. It is then discussed how the exciton spin and the optical polarization of exciting/emitted photons intercorrelate, in the absence and in the presence of external magnetic fields.

In **Chapter 4** the QD fabrication method is detailed. As the term “quantum dot” is unfortunately used for a wide range of systems with utterly different physical properties in the literature, it is important to detail the peculiarities of the CdSe/ZnSe material system. This chapter is therefore connecting the optical results to the morphological properties of the studied QDs and carefully summarizes all accessible information on the structural characteristics of our QD system, which also explains the choice of the individual samples for the forthcoming chapters.

Chapter 5 is the first of the two experimental result chapters and establishes the exciton energetic structure and formation dynamics in strongly confining CdSe/ZnSe epitaxial QDs. It thus forms the backbone for the investigations on the optical anisotropy studies performed in chapter six as it details how the optical excitation interconnects with the exciton properties. The chapter is concluded with the investigation of the interaction of excitons with phonons in the host matrix, which is markedly different from what has been observed for systems of higher dimensionality and, moreover, has not yet been clearly elaborated experimentally.

In **Chapter 6** the optical anisotropy that arises from the low symmetry nature of excitons confined to shape-anisotropic QDs is studied. First, effects based solely on the electron-hole exchange interaction that have been obtained in the absence of external fields are presented. From the optical anisotropy it is experimentally evidenced and successfully modeled in the frame of an exciton pseudospin-formalism, how the low symmetry of QDs gives rise to an effective conversion of the optical polarization from linear to circular states and vice versa. Applying the same formalism to optical alignment studies it is demonstrated how the optical data yield full information of the symmetry distribution of a QD ensemble.

Further, the influence of in-plane magnetic fields on the optical anisotropy is investigated. The resulting highly non-trivial polarization response is first qualitatively discussed in the frame of a band pseudo-spin formalism that is capable of describing the experimental findings in the high magnetic field limit. For a comprehensive quantitative analysis the full heavy-hole exciton **k.p**-Hamiltonian is numerically calculated and the resulting optical polarization is modeled. The model is able to quantitatively describe all experimental results using a single set of parameters and is then used to discuss important implications in the light of possible quantum applications.

Chapter 7 summarizes the important experimental results and based on the successfully applied models draws conclusions on the current understanding of epitaxial QDs. It is finally pointed out, how the herein used tools are capable of addressing open questions beyond the scope of the present work.

Chapter 2

Fundamental properties of semiconductor quantum dots

In this chapter we shall lay down the fundamental physical properties of a semiconductor system that is referred to as quantum dot. Unfortunately, the term Quantum Dot (QD) is routinely used in the literature for a variety of systems that can have quite different electronic and optical properties. In order to establish a clear cut terminology we therefore start from basic considerations that will hold for all QD systems and evolve this picture carefully for the situation encountered in semiconductors of cubic symmetry. In particular, the electronic properties of QDs based on zinc-blende type semiconductors, which is the crystal structure of the vast majority of III-V and II-VI compounds, shall be detailed. The chapter is closed by summarizing the current state of theoretic approaches to describe real QDs on a microscopic level, highlighting open questions and limitations to the present understanding of QDs.

2.1 Discrete energy spectrum of quantum dots

The optical and electronic properties of a given semiconductor system are very strongly determined by the available electronic states per energy per unit volume. This so called *density of states* $g(E)$ largely determines important characteristics like the optical absorption or the energetic distribution of carriers in a semiconductor. The standard textbook approach for the calculation of $g(E)$ starts from the energy-momentum dispersion of a parabolic band (see e. g. [Ash76]), which is a good approximation in the vicinity of the Γ -point of the Brillouin zone in a great number of low doped III-V and II-VI compound semiconductors. Hence,

$$E = \frac{\hbar^2 \mathbf{k}^2}{2m^*} \tag{2.1}$$

where \mathbf{k} is the corresponding wave vector to a given energy E , and m^* is the effective mass of the respective quasiparticle. In a cubic system¹ according to Bloch's theorem the components of the wave vector \mathbf{k} must be of the form

$$\mathbf{k} = \sum_{i=x,y,z} \frac{2\pi n_i}{L} \quad n_i \text{ integral} \quad (2.2)$$

where L is the length of the unit cell. The task is then to determine how many unit volumes of \mathbf{k} -space are contained in an energy interval E and $E + dE$, in order to obtain the density of states per unit energy. Thus, one effectively looks for the number of allowed states $g(\mathbf{k})d\mathbf{k}$ between surfaces of constant energy in \mathbf{k} -space, i. e. between \mathbf{k} and $\mathbf{k} + d\mathbf{k}$. In the 3D scenario for a bulk semiconductor the constant energy surfaces are defined by spheres in \mathbf{k} -space. The volume $v_{\mathbf{k}}$ between spheres of radius \mathbf{k} and $\mathbf{k} + d\mathbf{k}$ is found by

$$v_{\mathbf{k}}d\mathbf{k} = 4\pi|\mathbf{k}|^2d\mathbf{k} \quad (2.3)$$

and accounting for spin the number of states $g(\mathbf{k})_{3D}d\mathbf{k}$ is consequently given by

$$g(\mathbf{k})_{3D}d\mathbf{k} = 2 \times \frac{v_{\mathbf{k}}}{V_{3D}}d\mathbf{k} \quad (2.4)$$

where $V_{3D} = (\frac{2\pi}{L})^3$ is the volume occupied by a single energy state in \mathbf{k} -space for our cubic system. Combining Eq. 2.1 and Eq. 2.4 finally yields

$$g(E)_{3D}dE = \frac{1}{2\pi^2} \left(\frac{2m^*}{\hbar^2} \right)^{3/2} E^{1/2}dE \propto \sqrt{E}dE \quad (2.5)$$

The latter proportionality is of general nature for a 3D scenario and will also hold for non cubic systems[Jac98]. The situation is however completely changed if the quasiparticles are confined in one or several directions. How such a system can be achieved in a real semiconductor will be discussed in the following section. For the moment it suffices to consider an ideal particle in a box with infinite barriers. If so, the energy states along the confinement direction are quantized with discrete energy states and the sum of Eq. 2.2 accordingly reduces over the unrestricted directions. The calculation of $g(E)$ is done in complete analogy to the 3D case. Thus, for a 2D scenario in a Quantum Well (QW) one obtains

$$g(E)_{2D}dE = \frac{m^*}{\pi\hbar^2} \sum_i \Theta(E - E_i)dE \propto \sum_i \Theta(E - E_i)dE \quad (2.6)$$

where $\Theta(E - E_i)$ is the Heaviside step function and the index i runs over the available confined states in the QW. Further reduction of the dimensionality to the 1D case of Quantum Wires results in

$$g(E)_{1D}dE = \frac{1}{\pi} \left(\frac{2m^*}{\hbar^2} \right)^{1/2} \sum_i \left(\frac{n_i \Theta(E - E_i)}{\sqrt{E - E_i}} \right) dE \quad (2.7)$$

¹All semiconductor systems relevant to this Thesis are of cubic symmetry, justifying this assumption

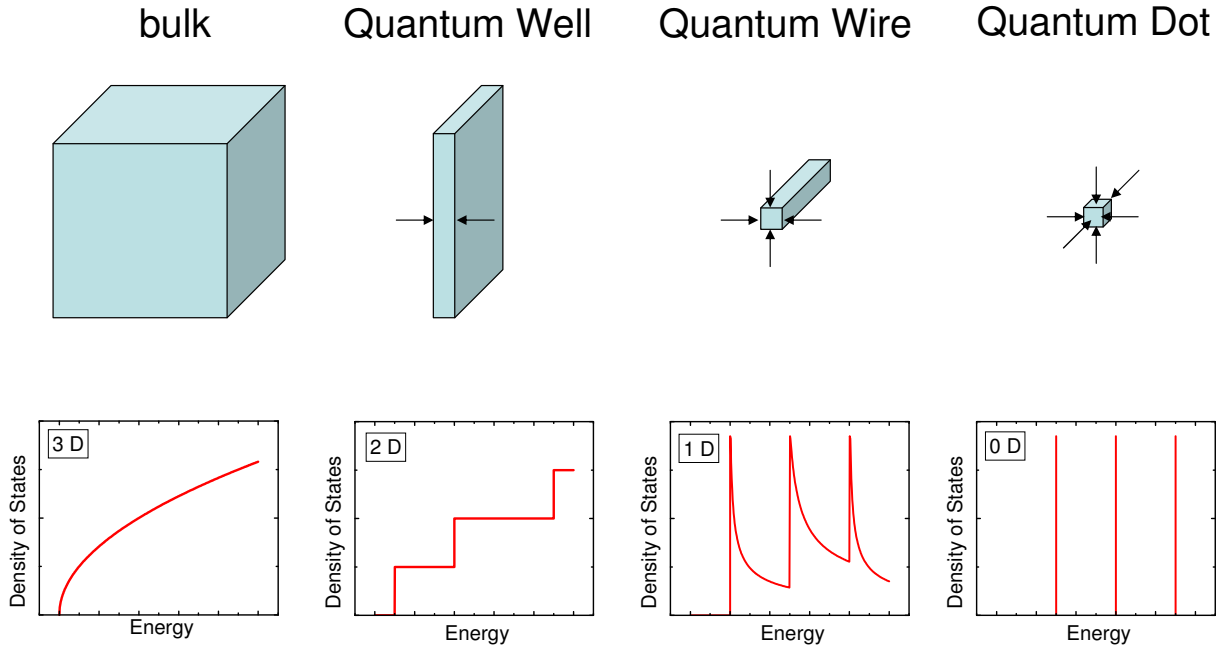


Fig. 2.1: Evolution of the density of states $g(E)$ as the dimensionality of the system is reduced from a bulk or 3D scenario for itinerant carriers to a Quantum Well with one confinement axis, further to the situation of a Quantum Wire with carrier confinement along two axes and ultimately to the 0D scenario of a Quantum Dot, where no free carrier motion is possible at all.

where again $\Theta(E - E_i)$ is the Heaviside step function. The index i now runs over all the quantized states in the two confined directions and the degeneracy factor n_i accounts for the fact that depending on the parameters several of the quantized energy states might coincide.

If the carriers are confined along all three spatial directions, no free motion is possible and as a direct consequence there is no \mathbf{k} -space to be filled up with carriers. The *density of states* for a 0D system is therefore discrete and given by

$$g(E)_{0D}dE = 2 \sum_i \delta(E - E_i)dE \quad (2.8)$$

where $\delta(E - E_i)$ is the Dirac function. The evolution of $g(E)$ as the dimensionality is reduced is summarized in Fig. 2.1.

In principle, all solid state objects realizing quantum confinement in all spatial directions are termed Quantum Dot, regardless of their specific properties. Because of their discrete energy spectrum they are also frequently dubbed “artificial atoms”. While QDs in fact exhibit certain aspects that justify this reference beyond their energy spectrum, this analogy should however be treated with extreme caution, as there are distinct and decisive differences between QDs and atoms. For one, the typical energy scales are vastly different, being on the 10 eV scale for the inter-level spacing in atoms as opposed to only some 10 meV in QDs. Further, isolated atoms exhibit centro-symmetric potentials, which usually only holds for idealized QDs. Real QDs generally display complicated internal

potentials arising from the interaction with their solid state environment, which critically depends on their material composition, size, shape, strain and strain-related effects like piezo-electricity. Thus, real QDs rarely ever exhibit true atom-like properties and are rather complex entities to understand from first principles. This shall be detailed in the following two sections.

2.2 Properties of quantum confined solid state systems

Quantum confinement comes into effect if the characteristic length-scales decrease below the extent of the *De Broglie wavelength* λ_{DB} , that is defined by

$$\lambda_{DB} = \frac{h}{\sqrt{2m^*k_B T}} \quad (2.9)$$

where h is the Planck constant, m^* is again the effective mass of the respective quasiparticle, k_B is the Boltzmann constant and T is the temperature of the system. For electrons in the conduction band of III-V or II-VI compound semiconductors m^* is approximately 10 % of the free electron mass and hence λ_{DB} is on the order of 20 nm at a temperature of 300 K. In order to obtain QDs the task is now to construct potential traps whose physical size is well below this limit in all spatial directions. With today's semiconductor technology this is achieved by implementing nanometer sized inclusions of a low bandgap semiconductor into the matrix of a semiconductor with a larger bandgap. This seemingly straightforward approach produces a wide range of differently shaped and sized QDs depending on the materials used and the exact growth conditions. Although this includes almost perfectly spherical chemically synthesized nanoparticles [Mur93], QDs grown by Metal-Organic Chemical Vapor phase Deposition (MOVCD) or Molecular Beam Epitaxy (MBE) usually exhibit lower symmetry, including lens-shaped [Leo97], pyramid-shaped [Fuk91], prism-shaped QDs [Guo97] and a wealth of QDs that display even further reduced shape-symmetry [Mas02]. The QD fabrication shall be further detailed in Chapter 4.

The resulting single-particle energy states for idealized potentials depending on the shape alone have been calculated for a large set of geometries and are available from the literature (see e. g. [Wog97, Bim99, Mic03]). We shall exemplify here the treatment of a perfectly spherical QD, which provides a good starting point. The corresponding problem of a noninteracting single quasiparticle in a centrosymmetric hard wall potential with finite barriers, having different effective masses m_1^* in the QD and m_2^* in the embedding matrix, is described by the following Hamiltonian [Tho90]

$$\mathcal{H}_i = -\frac{\hbar^2 \nabla_i^2}{2m_i^*} + V_i(\mathbf{r}_i) \quad \text{with} \quad V_i(\mathbf{r}_i) = \begin{cases} 0 & \text{for } r_i \leq R_0 \\ V_{0,i} & \text{for } r_i > R_0 \end{cases} \quad (2.10)$$

The index $i = e, h$ labels the electron or hole state, \mathbf{r}_i denotes the quasiparticle position, R_0 is the QD radius and V_0 is given by respective band offset. As such, any potential

contribution arising from the heterointerface is currently neglected. Like for all centrosymmetric potentials the wavefunction solution is separable into radial and angular components, i. e. $\Psi(\mathbf{r}) = R_{nml}(r)Y_{lm}(\vartheta, \phi)$, where Y_{lm} are the spherical harmonic functions. For the groundstate $n = 1$, $l = m = 0$ and the solution for the radial part of the wavefunction is found by

$$R_i(r_i) = \begin{cases} \frac{\sin(k_i r_i)}{k_i r_i} & \text{for } r_i \leq R_0 \\ \frac{\sin(k_i R_0)}{k_i r_i} e^{-\kappa_i(r_i - R_0)} & \text{for } r_i > R_0 \end{cases} \quad (2.11)$$

with the definitions of

$$k_i^2 = \frac{2m_{1,i}^*(V_{0,i} - E)}{\hbar^2} \quad \text{and} \quad \kappa_i^2 = \frac{2m_{2,i}^*(E)}{\hbar^2} \quad (2.12)$$

The boundary conditions that $R_i(r_i)$ and $(1/m_i^*)[\partial R_i(r_i)/\partial r_i]$ both have to be continuous at $r_i = R_0$ give rise to the transcendental equation

$$\tan(k_i R_0) = \frac{k_i R_0}{1 - \frac{m_{1,i}^*}{m_{2,i}^*}(1 + \kappa_i R_0)} \quad (2.13)$$

from which the energy of the single particle ground state in a spherical QD is obtained. Employing variational computation similar transcendental equations can be established for the QD excited states [Tho90]. Consequently, one can construct single particle energy shells in the spirit of atomistic energy levels, which is largely where the analogy to atoms stems from. It is readily seen in this picture, that the number of excited states found for the respective quasiparticles is determined by the magnitude of the band-offset, whereas the energetic interlevel spacing is set by the QD size. Also, for this strict spherical potential plain dipole transition selection rules will hold.

Even though the above treatment can describe some close to ideal systems like e. g. spherical CdS nanocrystals [Wel86, Tho90] to a reasonable extent, it is completely insufficient in order to treat the situation encountered in semiconductor hetero-nanostructures. For the lower symmetric shapes found for these objects, the wavefunction becomes non-separable and the Schrödinger equation usually has to be solved numerically. Further, the crude approximations made above, which essentially drop all contributions on the confining potential apart from the QD shape, are by no means valid for a realistic modeling. Arising from self-organized growth, whose main driving force is strain and the relaxation of the latter, QDs are heavily and sometimes inhomogenously strained, which naturally affects the QD potential geometry. This strain in return gives rise to internal electric fields due to piezoelectricity, which is especially important in II-VI compounds due to the highly polar bonds in this class of materials. According to recent theoretical work based on empirical pseudopotential calculations, even second order effects have to be taken into account when evaluating the impact of piezoelectricity on the QD potential in zinc-blende

type semiconductors [Bes06]. On an atomistic level one further has to consider effects of interface potentials, and for non-ideal growth also effects of alloy admixture of the QD and the corresponding barrier material, which can lead to a complete breakdown of any symmetry on the mesoscopic scale of the QD.

While all of the above significantly complicates the situation for electrons already, the scenario for holes is even more complex due to the p -like symmetry of the atomic orbital functions of holes. Within the effective mass approximation the resulting valence band states are classified as heavy-hole (HH), light-hole (LH) and split-off (SO) bands according to their respective angular momentum projection [Yu03]. Whereas the SO-band is always energetically split towards lower energies by the spin-orbit coupling, the HH and LH bands are degenerate at the Brillouin zone Γ -point for the bulk case². In QDs this degeneracy is lifted by strain and in particular by quantum confinement, which is easily conceived conceptually by Eq. 2.13. Due to the different effective masses of the LH and HH quasi-particles, their confinement energies are necessarily different and consequently will render the HH states the energetic ground state. In the case of compressive deformation (which is the situation encountered in all QD-heterosystems) the strain-induced change for the energetic ground state further follows the same trend. A progressing symmetry reduction by either natural shape asymmetry, strain, piezoelectricity, alloy admixture or a combination of all the above will cause a mixing of, at least, the HH and LH bands. For materials that exhibit a small spin-orbit coupling energy Δ_0 , like InP or CdS, the admixture will include even the SO band [Fu97]. As a consequence, the QD hole wavefunctions are fundamentally different from their bulk counterparts with respect to energetic position and symmetry. Moreover, it was recently established that holes in InAs/GaAs QDs do not obey the Aufbau principle upon charging multiple carriers into the confined valence band states of the QD [Reu05, He05, He06], accompanied by Coulombic hole-hole interactions that cannot be treated perturbatively and do not have an analogue in atomic physics [Edi07]. This is evidence that many-body effects may be important for holes in QDs, which are not covered at all using standard effective mass approximation based modeling. On balance, a thorough construction of the hole wavefunctions is a formidable task, that is still subject to a lively debate among theorists.

Further, QDs can bind electrons and holes *simultaneously*. The then present Coulombic electron-hole interaction greatly modifies the situation as it leads to the formation of bound electron-hole complexes - excitons. The complete Hamiltonian for the exciton is hence given by

$$\hat{H}_0 = \mathcal{H}_e + \mathcal{H}_h + \mathcal{H}_{Coulomb} \quad (2.14)$$

The Coulomb part of the Hamiltonian can further be decomposed into “direct” and “ex-

²Again, only bulk systems of cubic symmetry are considered

change” contributions. The former is given by [Fra97]

$$\mathcal{H}_{Coulomb}^{Direct} = \frac{e^2}{4\pi\epsilon_r\epsilon_0} \sum_{\sigma_e, \sigma_h} \int \frac{|\psi_h(\mathbf{r}_h, \sigma_h)|^2 |\psi_e(\mathbf{r}_e, \sigma_e)|^2}{|\mathbf{r}_h - \mathbf{r}_e|} d^3r_h d^3r_e \quad (2.15)$$

where ϵ_0 is the free space dielectric permittivity, ϵ_r is the relative dielectric permittivity of the QD and ψ_e and ψ_h are the microscopic electron and hole single particle wavefunctions of spin σ . This term yields the classical Coulomb attraction/repulsion and is the energetically dominating contribution to the formation of the excitonic multi-particle complex. In terms of absolute energy this term is heavily dependent on dimensionality, with the binding energies increasing from bulk to the QD case [Bry88]. In principle the exciton binding energy can be determined from intersubband transitions of single particle states in appropriately doped material. In QDs it is mainly a theoretical construct as there is no uncorrelated ground state of simultaneously present electrons and holes inside a QD. As such, the electron-hole attraction gives rise to bound states of the relative motion of the exciton. It is therefore, that another quantity is feasible upon considering the strength of the quantum confinement, which is the bulk exciton Bohr radius defined by

$$a_B = \frac{4\pi\epsilon_r\epsilon_0\hbar^2}{\mu_r^*e^2} \quad (2.16)$$

where $\mu_r^* = m_e^*m_h^*/(m_e^* + m_h^*)$. In general one can distinguish three regimes by considering the relative importance of effects arising from quantization of the kinetic energy and effects due to Coulomb attraction, which are [Bim99]:

- (a) The strong confinement regime, which is met when Coulomb effects are only small corrections to the quantization of the kinetic energy of the single particle states. This is the case if the energetic intersublevel spacing is much larger than the Coulomb energy E_C for both electrons and holes, i. e. $\Delta E_e \gg E_C$ and $\Delta E_h \gg E_C$. In this regime the electron and hole wavefunctions are largely uncorrelated. It occurs if the radius of the confining potential R_{QD} is much smaller than the bulk exciton Bohr radius a_B , i. e. $R_{QD} \ll a_B$. In this case \mathbf{k} conservation is completely lifted, as \mathbf{k} is no longer a good quantum number [Gru02].
- (b) The intermediate confinement regime applies if size quantization effects and Coulomb effects are of equal importance. This scenario can arise because of the difference in the effective masses of electrons and holes, and is usually met for $R_{QD} \approx a_B$, which implies $\Delta E_e \gg E_C$ but $\Delta E_h \lesssim E_C$. In this situation higher subband states are mixed into the exciton ground state. Further, excited states with respect to the relative motion of the exciton need to be included in the exciton wave function [Mas02].
- (c) The weak confinement regime is entered if Coulomb effects dominate over quantization effects of the kinetic energy. It is introduced if $R_{QD} \gg a_B$ and in this case only

the center-of-mass motion of the exciton is regarded as quantized. In this regime an almost continuous distribution of the quantized subbands occurs.

Since a_B is heavily dependent on the relative dielectric permittivity ϵ_r , the situation can be utterly different for comparable QD sizes in different materials. In the III-V compound semiconductors ϵ_r is relatively small and thus the bulk exciton Bohr radius is typically on the order of some 10 nm (e. g. $a_B \sim 36.3$ nm for InAs [Fu99]). On the contrary the II-VIs are highly polar materials and as a consequence of the resulting high ϵ_r the bulk exciton Bohr radius is typically on the order of a few nm only ($a_B(\text{CdSe}) \sim 5.6$ nm [Nir94]).

The second component of the Coulomb Hamiltonian in Eq. 2.14, the “exchange” part, is given by [Fra97, Tak00]

$$\mathcal{H}_{Coulomb}^{Exchange} = \frac{e^2}{4\pi\epsilon_r\epsilon_0} \sum_{\sigma_e, \sigma_h} \text{Re} \int \frac{\psi_h^*(\mathbf{r}_h, \sigma_h) \psi_e^*(\mathbf{r}_e, \sigma_e) \psi_h(\mathbf{r}_e, \sigma_e) \psi_e(\mathbf{r}_h, \sigma_h)}{|\mathbf{r}_h - \mathbf{r}_e|} d^3r_h d^3r_e \quad (2.17)$$

As a result of the quantum confinement and the subsequent enlarged overlap of the electron and hole wavefunctions within the small volume of the QD, this term is also enhanced with respect to the bulk case. Upon evaluating its impact on the internal energetic structure of the exciton, which is substantial, it is for technical reasons further decomposed into two contributions, which can be done either in real or in \mathbf{k} -space. For the calculations on the optical properties this is mostly done in real space, where it can be divided in a short range contribution, which represents the probability of finding both the electron and the hole within the same unit cell, and the long range part, which is given by the probability of finding them in different cells [Mas02]. The interplay of the QD confining potential symmetry and electron-hole exchange interaction has tremendous impact on the internal energetic structure of confined excitons, which is directly correlated to the optical polarization state of photons emitted upon radiative decay of the excitons and shall be described in great detail in chapter 3.

2.3 Modeling of real quantum dots

From the above it is obvious that a comprehensive theoretical description of semiconductor QDs is a challenging task, as it likely requires a description that goes beyond widely applied effective mass approximation (EMA) methods, which have been outstandingly successful upon describing bulk or 2D semiconductor systems. Especially two band EMA modeling, despite having frequently been used for describing experimental results, is certainly inappropriate and rather an expanded fitting procedure than a realistic description of a QD system.

On the other hand, for typical sizes of some ten nanometers a single QD consists of 10^5 to 10^6 atoms. For starting from the atomistic potentials and only considering the sp^3 orbitals, i. e. eight electrons per atom, this already requires taking $10^6 - 10^7$ electrons into

account, which is beyond present computational capabilities. Both tight binding approaches and ab initio methods necessarily include delicate approximations.

Despite these fundamental difficulties, a variety of theoretical descriptions of realistic QDs have evolved over the past ten years, including eight band $\mathbf{k} \cdot \mathbf{p}$, tight binding and empirical pseudopotential based first principle methods. While by no means presenting a complete description, they shall briefly be reviewed and compared in terms of their capabilities and limitations. For more in-depth information the reader is referred to the nice review of P. Hawrylak and M. Korkusiński [Mic03].

Eight-band $\mathbf{k} \cdot \mathbf{p}$ methods. These approaches start out from the assumption that the quasiparticle picture of electrons in the conduction band and holes and the valence band worked eminently successful in bulk and 2D semiconductors and should therefore likely represent a valid representation for semiconductor QDs as well. The calculation of the single particle states is done according to the envelope function ansatz, which is the key ingredient of the $\mathbf{k} \cdot \mathbf{p}$ approximation [Bas88]. By Bloch's theorem [Blo28] the electron wave function in a periodic lattice displaying translational symmetry can be separated into a fast oscillating part with the atomistic distance as a period (Bloch part) and a slowly oscillating, smooth envelope function part, which is varying at most on mesoscopic scales. According to Löwdin perturbation theory the fast oscillating Bloch part can be eliminated from the electron Hamiltonian such that only quantum mechanical equations of motion for the envelope function remain. In the vicinity of the Γ -point of a cubic system the electron wavefunction are s -type for the conduction band and p -type for the valence band. Incorporating spin, it requires eight Bloch functions to form the basis states for the corresponding bands, denoted $s \uparrow, x \uparrow, y \uparrow, z \uparrow, s \downarrow, x \downarrow, y \downarrow$ and $z \downarrow$, with x, y and z being the p -type Bloch functions along the corresponding principal crystal axes. The envelope functions to this eight Bloch functions form the basis for the Hamiltonian in the eight-band Kane model [Kan57].

The determination of the single particle eigenstates and energies then starts out with the appropriate choice of the QD shape and the calculation of the resulting strain tensor matrix elements. This is usually done from the continuum mechanical model (CMM) [Saa89]. O. Stier *et al.* [Sti99] compared the results obtained in this approach with calculations based on the valence force field model (VFF) [Kea66] and concluded that, while the differences inside the QD are insignificant, at the interfaces the CMM is yielding results closer to reality when compared to the experiment. The strain information is applied to determine the piezoelectric charge density, from which the piezoelectric potential is calculated [Sti97]. The resulting potentials are hence fed back into the Hamiltonian which is then numerically diagonalized [Pry97, Sti97]. Exciton binding energy and few particle states are finally determined by the Hartree-Fock approximation taking into account Coulomb interaction and correlation effects.

The apparent advantage of $\mathbf{k} \cdot \mathbf{p}$ models is their dependence on only a few (about 20) parameters which enter the calculation and therefore their relatively low computational expense. They have been successfully applied to larger sized III-V QDs [Pry97, Sti99],

with InAs/GaAs QDs being the most prominent and best studied example [Mic03]. For these QDs, which generally fall into the strong confinement regime, good agreement is reached between experiment and the model [Gru02]. It is especially useful for analyzing the microscopic origin of the peculiarities of the optical properties of QDs, such as the excitonic finestructure splitting (see chapter 3)[Seg05].

The model has, however, some inherent limitations, which arise from the fundamental assumptions. For one, the $\mathbf{k} \cdot \mathbf{p}$ scheme is only valid in the direct vicinity of the Brillouin zone Γ -point and therefore is increasingly inaccurate for smaller QD sizes. Second, as the Bloch functions are taken to be identical throughout the complete heterostructure, any contributions arising from the interface, alloy fluctuation or strain variation are necessarily screened out and do not enter the model. These limitations do not exist in microscopic approaches. Maybe the biggest disadvantage of $\mathbf{k} \cdot \mathbf{p}$ models, however, is their critical dependence on the input parameters of shape and size of the modeled QDs, which are generally not very accurately known from experiments when the QDs are capped by additional semiconductor material (see chapter 4). The large scatter in the reported experimental results imposes serious limitations to the predictive powers of this approach.

Empirical tight binding methods. While EMA theory treats QDs as confined bulk systems, pseudopotential theory is targeted at a detailed atomistic description of the wave functions. Empirical tight-binding methods (ETB) fall in between these two essentially opposite approaches by limiting the local degrees of freedom to only a small basis set within the frame of an atomistic description. In the tight binding approach one generally selects only the most relevant orbitals of the atoms, each of which is aligned according to the underlying crystal symmetry. The wavefunction of the studied system is then expanded in the basis of these localized orbitals, usually taking into account only nearest neighbour interactions.

In the ETB sp^3s^* method first introduced by Vogl *et al.* [Vog83] each atom situated on its respective position in a zinc-blende type lattice is described by the real space atomic basis orbitals s, p_x, p_y, p_z and a fictitious s^* orbital that is used to mimic effects of higher lying states, e. g. the influence of d -bands on the bandstructure. The empirical single particle Hamiltonian is hence constructed by adjusting the matrix elements to reproduce the experimentally determined band gaps and effective masses of the bulk band structure [Bry01]. As a consequence of this empirical adjustment there is no direct way to calculate Coulomb and exchange matrix elements. Lee *et al.* derived the energies of the exciton states by diagonalizing the configuration-interaction matrix obtained from the energetically lowest electron and hole states [Lee01]. They found that their calculated excitonic gaps agree within 5 % error with photoluminescence data, yet concluded that their results sensitively depend on the choice of the atomic orbitals and are only reliable as long as the QD size exceeds ~ 2 nm.

A somewhat simplified version of the tight binding model, the empirical bond orbital model (EBOM) was introduced and initially applied to superlattices by Chang [Cha88]. For minimum computational cost, only one s -like antibonding orbital for the conduction

band and three p -like bonding orbital for the valence band are considered. The interactions between these four orbitals are then chosen such that the band structures of the constituent bulk materials near the Brillouin zone Γ -point are identical to those obtained from $\mathbf{k} \cdot \mathbf{p}$ theory. In this sense the EBOM is a real space equivalent of the $\mathbf{k} \cdot \mathbf{p}$ model, which properly reproduces effective masses, but also captures atomistic aspects. Strain is incorporated using the VFF model, as it yields a strain tensor on an atomistic level, rendering it more suitable for atomistic approaches. As in the $\mathbf{k} \cdot \mathbf{p}$ approach, piezoelectricity arising from the shear strain is included in the Hamiltonian and exciton states are determined by the Hartree approximation. The energetic structure, charge distribution and exciton binding energies obtained from EBOM for pyramidal InAs/GaAs QDs are, not surprisingly, in good agreement with those obtained from $\mathbf{k} \cdot \mathbf{p}$ calculations [Sun00].

On balance, ETB methods represent computationally affordable models capable of describing even large QDs, up to 25 nm size, without restricting atomic-scale variations on the wave functions considerably. However, as the tight-binding matrix elements are adjusted empirically, the incorporation of electron-hole interactions is necessarily accompanied by critical approximations, which can cause considerable deviations from the experimental values. For example, empirical nearest neighbour sp^3s^* calculations overestimate the excitonic band gap of spherical InAs crystallites by almost 200 meV [Lee01]. As such, at present the predictive powers of ETB methods on excitonic properties of QDs are limited.

First principle methods. The only first principle method, which is currently applied to QD heterostructures, is an empirical pseudopotential method employed by Zunger and co-workers. This method is not an “ab-initio” method in the literal sense but rather incorporates a series of thoughtful approximations starting out from the (multi-)million atom problem of a real QD heterostructure. The outline of their method of calculation is the following [Wil00]:

(1) First they assume shape, size and chemical composition of the QD structure under study. In the case of QD heterostructures a supercell is constructed that contains both the QD and a sufficient amount of the surrounding barrier material. Hence, the equilibrium displacements of the atoms are computed by minimizing the strain energy. For the case of QD heterostructures this is done in the frame of a VFF model.

(2) Second, a single particle Schrödinger equation is set up with the relaxed atomic positions $\{\mathbf{R}_{\alpha n}\}$:

$$\hat{H}\psi_i(\mathbf{r}) = \left\{ -\frac{\hbar^2}{2m}\nabla^2 + \sum_{\alpha n} \hat{v}_{\alpha}(\mathbf{r} - \mathbf{R}_{\alpha n}) \right\} \psi_i(\mathbf{r}) = \epsilon_i\psi_i(\mathbf{r}) \quad (2.18)$$

Here, the index n runs over the coordinates of the relaxed atomic positions and α labels the atomic species. As such the many-body problem is reduced to an effective single particle problem in the sense of the Kohn-Sham approximation [Koh65], which can be solved self-consistently. For most of the constituent materials the Kohn-Sham self-consistent orbitals and local density approximation (LDA) potentials are known from the literature. Their

agreement with real material parameters is, however, rather poor, e. g. the band gap of GaAs is overestimated by almost 30 %. For that reason, the atomic pseudopotentials \hat{v}_α are empirically fit to reproduce the bulk band structure, yielding realistic values for energy gaps, effective masses and their anisotropies. This fitting procedure, which is very much in the sense of the fitting procedures used in tight binding approaches, is the key ingredient of the “empirical pseudopotential method”.

(3) Next, the single particle Schrödinger equation is solved using the linear combination of bulk bands method [Wan99].

(4) Further, the dielectric screening function and the interparticle direct Coulomb and Coulomb exchange integrals are computed.

(5) Finally, from the single particle energy levels and the interparticle interactions the many-particle energy states are calculated.

It is obvious that the computational effort of this method is immense, which imposes serious restrictions to its general applicability. Further criticism arises towards the choice of the pseudopotentials, as any results are certainly heavily dependent on these. In light of the accuracy of LDA methods to only several percent, it is arguable whether or not predictions on QD energy states to an accuracy of a few meV are reliable. However, the empirical pseudopotential method has proven its robustness under the test of experimental results and is certainly a very powerful method for the prediction of material-dependent trends in the electronic and optical properties of QDs. For instance, the model quantitatively reproduces the fine structure splitting (FSS) of charge neutral [Bes03] as well as multiply charged excitons [Edi07] in $\text{In}_x\text{Ga}_{1-x}\text{As}/\text{GaAs}$ QDs for different shapes and different compositions. It is further capable of following the complex filling sequence for holes in positively charged excitons [He06], which appear to defy both Hund’s rule and the Aufbau principle, as recently established in experiments [Edi07]. Finally, the obtained quasiparticle wavefunctions are in superb agreement with experimental magnetotunneling results [Bes07] on InAs/GaAs QDs, which can be considered as promising early effort towards wave-function engineering in future QD objects.

Summary. QDs challenge many of the established concepts and methods, which have been successfully applied to semiconductor problems of higher dimensionality. Despite a principle understanding of many QD properties, a comprehensive theoretical description of the sensitive interplay of constituent material, substrate, growth conditions, dot morphology and the resulting electronic and optical properties is far from being reached. A big obstacle towards this goal is the limited availability of structural information on QDs in combination with spectroscopic results. While a wealth of the latter has been published over the last 15 years, often in remarkable quality, it is rarely ever linked directly to structural studies. On the other hand all currently applied models start from the assumption of the QD shape. This obvious discrepancy is not easily lifted, as high quality optical properties of embedded QDs require capping for the passivation of surface states, which otherwise provide nonradiative decay channels. It is a dedicated goal of this work to provide additional experimental insight on this subject.

Chapter 3

Optical Properties of epitaxial semiconductor quantum dots

In this chapter we shall establish the basic optical properties of epitaxial semiconductor QDs, which form the basis from which we start the optical studies presented in this thesis. By epitaxial QDs we explicitly mean embedded QD heterostructures that have been grown by methods of molecular beam epitaxy (MBE). We therefore differentiate from chemically synthesized QD nanoparticles, which will be of no further relevance to the remainder of this thesis, albeit that some of the results obtained in this work will also apply to the latter.

We start out from basic considerations on the bulk electronic energy structure in direct band-gap zinc-blende type semiconductor compounds and establish the polarization properties of optical interband transitions of single particles in this situation from fundamental symmetry considerations. Whereas the sole material system studied in the current work is the CdSe/ZnSe heterosystem, most of the results obtained are only based on symmetry arguments and are therefore valid for all systems of the corresponding symmetry. This includes the widely studied InAs/GaAs and also the CdTe/ZnTe system, which together with CdSe/ZnSe QDs represent the most prominent semiconductor QD systems studied in the light of possible optical applications.

From the single particle picture we evolve the optical properties of excitons in low dimensional systems of reduced symmetry in the absence of external fields. In this context we shall briefly review the concept of the Poincaré and Bloch spheres, which will prove to be very useful in the later on analysis of the experimental data. Further, the wealth of excitonic complexes observable in QDs and their often intriguing optical properties is introduced. We proceed by describing the effect of external magnetic fields on the energetic structure and optical polarization properties on charge neutral excitons in QDs. The chapter is closed by discussing the exciton-phonon interaction in CdSe/ZnSe QDs, which is the only material specific and therefore non-general section of this chapter.

3.1 Optical properties of direct gap zinc-blende type compound semiconductors

The material system under investigation in this work is the CdSe/ZnSe heterosystem, meaning that the QDs on which our studies focus are built from $\text{Zn}_x\text{Cd}_{1-x}\text{Se}$ alloys. The exact composition of the QD nanostructures arising from different variants of MBE growth can vary significantly as a result of material interdiffusion, as shall be detailed in chapter 4. In most cases, however, the QDs will not be formed by pure CdSe. It is therefore important to state that the heteroepitaxy of $\text{Zn}_x\text{Cd}_{1-x}\text{Se}$ on (001)-oriented GaAs by MBE always results in single-phase zinc-blende crystals over the complete composition range from ZnSe to CdSe [Kim94]. This is in contrast to bulk single crystals of the $\text{Zn}_x\text{Cd}_{1-x}\text{Se}$ alloy, which exhibits zinc-blende structure only for $x \leq 0.3$, crystallizes in the hexagonal wurtzite structure for $x \geq 0.5$ and displays mixed phases for $0.3 < x < 0.5$ [Nas89]. As all samples investigated were grown by MBE heteroepitaxy on (001)-GaAs, the microscopic symmetry encountered in all QD nanostructures is the according symmetry of the zinc-blende structure, which is the most commonly occurring crystal structure in binary II-VI and III-V compound semiconductors.

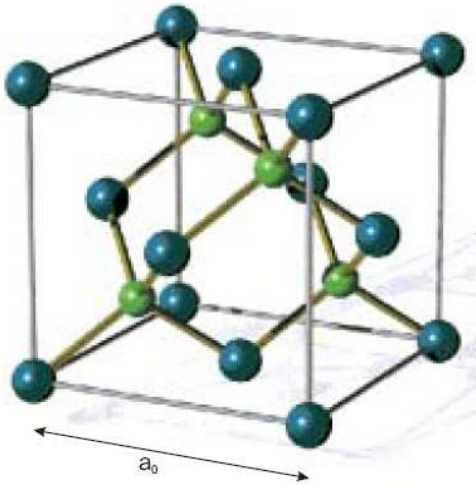


Fig. 3.1: Unit cell of the zinc-blende crystal structure, a_0 represents the lattice constant. Large (blue) and small (green) symbols designate the respective atomic species on the fcc sublattice sites, which are shifted against each other by $\frac{\sqrt{3}}{4}a_0$ in (111) direction. Adopted from [Fie04].

The zinc-blende structure consists of two face-centered cubic (fcc) sublattices, which are displaced against each other by one fourth of the width of the cubic cell in (111) direction (see Fig. 3.1). Each of the corresponding sublattices is populated by one atomic species only, such that every cation is tetrahedrally surrounded by four anions and vice versa. The resulting unit cell of the zinc-blende lattice therefore contains four atoms of both atomic species.

The chemical bonds between adjacent ions are formed by the outer s - and p -valence electrons. The remaining electrons of each kind of atom are highly bound to the nuclei and do not contribute to the electronic properties important for electric transport or optical interband transitions. The resulting sp^3 -hybridized bonds between anions and cations are mainly of covalent nature for III-V, but have reasonable ionic character for II-VI alloys.

3.1.1 Crystal symmetry and band structure

The symmetry of the zinc-blende structure is described by the T_d point group, which is the full symmetry group of the tetrahedron and is a subgroup of the full spherical group O_h . It consists of an overall of 24 elements, which include the 12 elements of group T (group of rotations, which leave a tetrahedron invariant), six reflections in the plane σ_d and six improper rotations s_4 and s_4^3 [Bir74]. In contrast to monoatomic diamond-lattice semiconductors (e. g. silicon), zinc-blende type compound semiconductors do not display inversion symmetry.

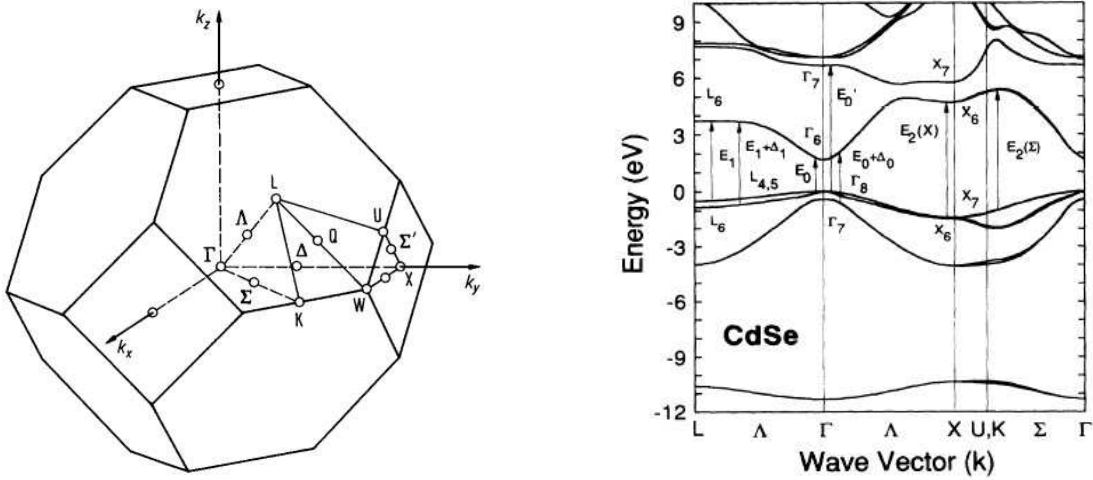


Fig. 3.2: First Brillouin zone of a zinc-blende structure crystal including high symmetry points (left) and corresponding energy band structure of zinc-blende CdSe calculated by Kim *et al.* by the nonlocal empirical pseudopotential method from ellipsometric measurements of the dielectric function (right) [Kim94].

The first Brillouin zone of the zinc-blende structure is represented by the well known truncated octahedron, displayed in Fig. 3.2 including the group theoretically important high symmetry points. Zinc-blende type CdSe falls into the class of direct gap semiconductors, which means that the top of the energetically highest occupied band (termed valence band - VB) coincides with the bottom of the energetically lowest unoccupied band (termed conduction band - CB) at the Brillouin zone center, designated Γ -point in group theory notation. The CB is formed by the antibonding Σ -orbitals, which therefore has an s -like symmetry that is described by the Γ_6 representation in the frame of group theory double group representation that includes spin. The VB is thus formed by the bonding Π -orbitals, accordingly the VB is of p -type symmetry. Inclusion of the spin-orbit coupling splits the otherwise sixfold degenerate VB, whereby the $P_{1/2}$ -states, described by the Γ_7 -representation, are energetically shifted to lower energies by a few 100 meV with respect to the $P_{3/2}$ -states, which fall into the Γ_8 representation. In zinc-blende-type CdSe this splitting is $\Delta_0 = 390$ meV [Kim94]. The $\mathbf{J} = 3/2$ states further decompose into a subband of $J_z = \pm 3/2$ -states termed heavy-hole (HH) band, and a subband of $J_z = \pm 1/2$ -

states designated light-hole (LH) band. In the absence of strain or external fields the HH and LH bands are degenerate at the Γ -point, but energetically split for $\mathbf{k} \neq 0$. Strictly speaking, the bulk inversion asymmetry further results in a quasimomentum dependent magnetic field acting on the quasiparticle spins, which is known as the Dresselhaus effect [Dre55], that gives rise to an energetic splitting of all band-states according to their spin projection. However, this splitting is extremely small for wide-gap materials like CdSe, as it scales with the inverse of the fundamental band gap E_g [Lom88] and can be safely neglected for the remainder of this work.

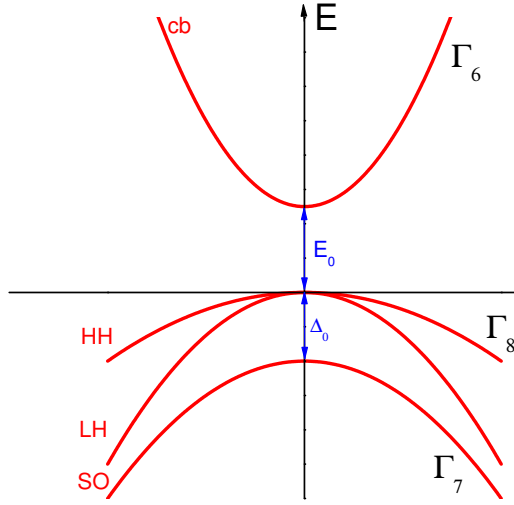


Fig. 3.3: Scheme of the k -dispersion of the bandstructure in T_d symmetry at the Brillouin-zone center. In the direct vicinity of the Γ -point the band dispersion is well approximated parabolic. Due to the energetic shift Δ_0 of the SO bands to lower energies, they do not have measurable impact on the radiative $\mathbf{k} = 0$ interband recombination properties.

From the above we now turn to a formal description of the energetic bandstructure. In a bulk crystal we have to solve the following one-electron Schrödinger equation:

$$\left[\frac{\mathbf{p}^2}{2m_0} + V(\mathbf{r}) + \frac{\hbar}{4m_0^2c^2}(\boldsymbol{\sigma} \times \nabla V)\mathbf{p} \right] \Psi(\mathbf{r}) = \varepsilon\Psi(\mathbf{r}) \quad (3.1)$$

Here m_0 is the free electron mass and $V(\mathbf{r})$ is the crystalline potential, which includes averaged electron-electron interactions and is periodic with periodicity of the underlying Bravais lattice. The third term is a relativistic correction that gives rise to the spin-orbit coupling, where \hbar is the Planck constant over 2π , c is the vacuum speed of light and $\boldsymbol{\sigma}$ is the electron spin operator. According to Bloch's theorem, the wave function of an electron in the crystal periodic potential is given by [Blo28]

$$\Psi(\mathbf{r}) = e^{i\mathbf{k}\mathbf{r}}u_{n\mathbf{k}}(\mathbf{r}) \quad (3.2)$$

where the Bloch function $u_{n\mathbf{k}}(\mathbf{r})$ has the periodicity of the underlying lattice and n is the respective band index. The Bloch functions are rarely ever known explicitly. However, by the von Neumann principle, the physical observables of a system must exhibit the same symmetry as the system itself. We can therefore establish basic considerations on the Bloch band's transformation properties based on group theoretical arguments, without finding explicit solutions. As the CB and VB are formed by the atomic s and p states,

we introduce the states $|s\rangle$, $|x\rangle$, $|y\rangle$ and $|z\rangle$ and require their associated wavefunction to transform in the same way as the atomic s , x , y and z functions under symmetry operations that map the local tetrahedron onto itself. Introducing spin, the eight states $|s\rangle \uparrow$, $|s\rangle \downarrow$, $|x\rangle \uparrow$, $|x\rangle \downarrow$, $|y\rangle \uparrow$, $|y\rangle \downarrow$, $|z\rangle \uparrow$, $|z\rangle \downarrow$ shall be used as basis functions, with \downarrow , \uparrow being the eigenspinors of the operator σ_z ,

$$\uparrow = \begin{pmatrix} 1 \\ 0 \end{pmatrix}, \quad \text{and} \quad \downarrow = \begin{pmatrix} 0 \\ 1 \end{pmatrix} \quad (3.3)$$

By substituting Eq. 3.2 into Eq. 3.1, we obtain that the Bloch functions $u_{n\mathbf{k}}$ are solutions of

$$\left[\frac{\mathbf{p}^2}{2m_0} + V(\mathbf{r}) + \frac{\hbar}{4m_0^2c^2}(\boldsymbol{\sigma} \times \nabla V)\mathbf{p} + \frac{\hbar^2\mathbf{k}^2}{2m_0} + \frac{\hbar}{m_0} \left(\mathbf{k} \cdot \mathbf{p} + \frac{\hbar\mathbf{k}}{4m_0c^2}\boldsymbol{\sigma} \times \nabla V \right) \right] u_{n\mathbf{k}} = \varepsilon u_{n\mathbf{k}} \quad (3.4)$$

This relation is exact. The appearance of the $\mathbf{k} \cdot \mathbf{p}$ term is the reason of the designation of the eponymous method, which is highly feasible in cases, where a global description of the energy band dispersion relation over the complete Brillouin zone is unnecessary, as is our case. One can rearrange Eq. 3.4 into

$$[\mathcal{H}(\mathbf{k} = 0) + \mathcal{W}(\mathbf{k})] u_{n\mathbf{k}} = \varepsilon_{n\mathbf{k}} u_{n\mathbf{k}} \quad (3.5)$$

where $\mathcal{H}(\mathbf{k} = 0)$ is the crystal Hamiltonian with eigenfunctions u_{n0} , i. e.

$$\mathcal{H}(\mathbf{k} = 0)u_{n0} = \varepsilon_{n0}u_{n0} \quad (3.6)$$

The \mathbf{k} -dependent part $\mathcal{W}(\mathbf{k})$ vanishes for $\mathbf{k} = 0$ and is usually treated as a perturbation in the direct vicinity of the Γ -point. It is then straightforward to show (see e. g. [Bas88]) that as long as \mathbf{k} is small, the energy band dispersion relation is parabolic in \mathbf{k} , as displayed in Fig. 3.3. However, due to the presence of spin-orbit interaction and the appearance of the $\mathbf{k} \cdot \mathbf{p}$ term, Eq. 3.4 is non-diagonal in our original basis. As it is desirable to have a diagonal basis at $\mathbf{k} = 0$, because it vastly simplifies the calculation of optical interband transitions, we transform to a new basis such that the total angular momentum $\mathbf{J} = \mathbf{L} + \boldsymbol{\sigma}$ and its projection J_z along the z -axis, which we choose to be the main quantization axis, are diagonal in the new basis. The latter is found by forming linear combinations of the original Bloch function basis as shown by Kane [Kan66] and the resulting states are consequently labeled by $|\mathbf{J}; J_z\rangle$.

For the s -like Γ_6 states $|\frac{1}{2}; -\frac{1}{2}\rangle$, $|\frac{1}{2}; +\frac{1}{2}\rangle$ of the conduction band one finds

$$u_{-1/2}^{\Gamma_6} = i|s\rangle \downarrow, \quad u_{1/2}^{\Gamma_6} = i|s\rangle \uparrow \quad (3.7)$$

Equivalently, the heavy-hole band states $|\frac{3}{2}; -\frac{3}{2}\rangle$, $|\frac{3}{2}; +\frac{3}{2}\rangle$ are found to be

$$u_{-3/2}^{\Gamma_8} = \frac{1}{\sqrt{2}}(|x\rangle - i|y\rangle) \downarrow, \quad u_{3/2}^{\Gamma_8} = \frac{1}{\sqrt{2}}(|x\rangle + i|y\rangle) \uparrow \quad (3.8)$$

and the light hole band states $|\frac{3}{2}; -\frac{1}{2}\rangle, |\frac{3}{2}; +\frac{1}{2}\rangle$ are

$$u_{-1/2}^{\Gamma_8} = \frac{1}{\sqrt{6}}(|x\rangle - i|y\rangle) \downarrow + \sqrt{\frac{2}{3}}|z\rangle \uparrow, \quad u_{1/2}^{\Gamma_8} = \frac{1}{\sqrt{6}}(|x\rangle + i|y\rangle) \uparrow + \sqrt{\frac{2}{3}}|z\rangle \downarrow \quad (3.9)$$

For sake of completeness we give the SO band states $|\frac{1}{2}; -\frac{1}{2}\rangle$ and $|\frac{1}{2}; +\frac{1}{2}\rangle$, which are given by

$$u_{-1/2}^{\Gamma_7} = -\frac{1}{\sqrt{3}}(|x\rangle - i|y\rangle) \uparrow + \sqrt{\frac{1}{3}}|z\rangle \downarrow, \quad u_{1/2}^{\Gamma_7} = -\frac{1}{\sqrt{3}}(|x\rangle + i|y\rangle) \downarrow - \sqrt{\frac{1}{3}}|z\rangle \uparrow \quad (3.10)$$

The SO bands shall be neglected in what is to come, as they are of no relevance for the band edge luminescence studied below.

3.1.2 Radiative band-to-band recombination at $\mathbf{k} = 0$

In a high quality semiconductor optically excited or electrically injected electrons and holes will thermalize and thus accumulate at the conduction and valence band extrema. The radiative decay in a direct semiconductor hence takes place at the Γ -point. The polarization properties of optical interband transitions can be therefore directly established from fundamental considerations regarding the symmetry described above. According to Fermi's Golden Rule, the transition rate W_Γ from the Γ_6 to the Γ_8 states per unit time is given by [Yu03]

$$W_\Gamma \propto \sum_{cv} |P^{cv}|^2 \delta(\varepsilon_{\Gamma_6} - \varepsilon_{\Gamma_8} + \hbar\omega) \quad (3.11)$$

where $\varepsilon_{\Gamma_6}, \varepsilon_{\Gamma_8}$ are the $\mathbf{k} = 0$ energies of the Γ_6 and Γ_8 bands, and $\hbar\omega$ is the energy of the emitted photon. P^{cv} is the transition matrix element, which in the electric dipole approximation is given by

$$P^{cv} = \langle \psi_c | \hat{e} \cdot \mathbf{p} | \psi_v \rangle \quad (3.12)$$

where ψ_c, ψ_v are the conduction and valence band wavefunctions, \mathbf{p} is the dipole momentum operator and \hat{e} is a unit vector pointing along the direction of \mathbf{p} . By inserting Eq. 3.2 into Eq. 3.12 we immediately obtain for $\mathbf{k} = 0$:

$$P^{cv} = \langle u_{c0} | \hat{e} \cdot \mathbf{p} | u_{v0} \rangle \quad (3.13)$$

The u_{c0} functions are given by the Γ_6 Bloch functions established in Eq. 3.7, whereas the u_{v0} functions are the Γ_8 Bloch functions given in Eq. 3.8 and 3.9. Here we directly see that the optical polarization properties of the band-to-band recombination is given by the transformation properties of the band edge Bloch functions, i. e. the symmetry of the crystal lattice. By symmetry it is required that the only nonzero transition matrix elements are:

$$-i\frac{\hbar}{m_0} \langle s | p_x | x \rangle = -i\frac{\hbar}{m_0} \langle s | p_y | y \rangle = -i\frac{\hbar}{m_0} \langle s | p_z | z \rangle = P \quad (3.14)$$

By substituting Eqs. 3.7, 3.8 and 3.9 into Eq. 3.13 and using the orthogonality of the eigenspinors \uparrow and \downarrow , we find the matrix elements of the dipole momentum operator P^{cv} , which are:

$$\begin{array}{c|cccc} \hat{e} \cdot \mathbf{p} & |\frac{3}{2}; +\frac{3}{2}\rangle & |\frac{3}{2}; +\frac{1}{2}\rangle & |\frac{3}{2}; -\frac{1}{2}\rangle & |\frac{3}{2}; -\frac{3}{2}\rangle \\ \langle \frac{1}{2}; +\frac{1}{2}| & -e_-P & +\sqrt{\frac{2}{3}}e_zP & +\sqrt{\frac{1}{3}}e_+P & 0 \\ \langle \frac{1}{2}; -\frac{1}{2}| & 0 & -\sqrt{\frac{1}{3}}e_-P & +\sqrt{\frac{2}{3}}e_zP & +e_+P \end{array}$$

where $e_{\pm} = \frac{1}{\sqrt{2}}(e_x \mp ie_y)$ designates the unit vector of righthanded and lefthanded helicity, respectively. With these, we directly obtain from Eq. 3.11 the polarization properties and relative intensities of optical interband transitions from the Γ_6 to the Γ_8 band at $\mathbf{k} = 0$, which are summarized in Fig. 3.4.

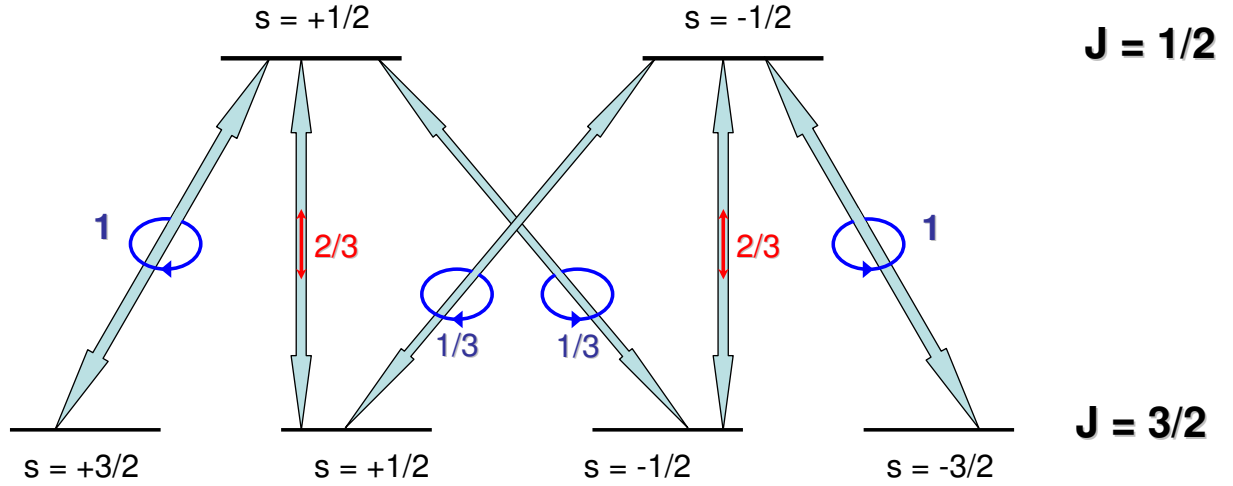


Fig. 3.4: Optical polarization and relative transition probability for interband recombination from the conduction band into $J = 3/2$ valence band states (or absorption vice versa). The transitions are either perfectly circularly (σ^+ , σ^-) or linearly polarized along the z -axis (π^z). The linearly polarized transitions are therefore not observable for light propagating along $\mathbf{k} = k_z$.

We find σ^+ polarization for the $|\frac{1}{2}; -\frac{1}{2}\rangle \rightarrow |\frac{3}{2}; -\frac{3}{2}\rangle$ and $|\frac{1}{2}; +\frac{1}{2}\rangle \rightarrow |\frac{3}{2}; -\frac{1}{2}\rangle$ transitions, σ^- polarization for the $|\frac{1}{2}; +\frac{1}{2}\rangle \rightarrow |\frac{3}{2}; +\frac{3}{2}\rangle$ and $|\frac{1}{2}; -\frac{1}{2}\rangle \rightarrow |\frac{3}{2}; +\frac{1}{2}\rangle$ transitions and linear polarization along z for the $|\frac{1}{2}; +\frac{1}{2}\rangle \rightarrow |\frac{3}{2}; +\frac{1}{2}\rangle$ and $|\frac{1}{2}; -\frac{1}{2}\rangle \rightarrow |\frac{3}{2}; -\frac{1}{2}\rangle$ transitions. The latter are obviously not observable for light propagating along the z -axis.

Note that optical absorption between these two bands obeys the exact same polarization properties, which means that optical excitation with the appropriate polarization enables preparation of required spin states. It is further clear from Fig. 3.4, that in the absence of external fields, strain or quantum confinement, which leaves the above states degenerate for their J_z -projections, the optical polarization degrees compensate each other and the net degree of optical polarization observed for radiative recombination is zero. However, a very important result is that for cubic systems (T_d) plain dipole transition

rules hold at $\mathbf{k} = 0$, despite their lowered symmetry with respect to the full spherical group $SO(3)$. These are:

$$\Delta L = \pm 1, \quad \Delta m = -1, 0, +1 \quad (3.15)$$

where the polarization state of the emitted light is given by Δm according to

$$\begin{aligned} \Delta m = +1 &\leftrightarrow \sigma^+ \\ \Delta m = 0 &\leftrightarrow \pi, \quad \text{with} \quad \Delta m = m_{initial} - m_{final} \\ \Delta m = -1 &\leftrightarrow \sigma^- \end{aligned} \quad (3.16)$$

In group theoretical terms Eq. 3.15 is described by the Γ_{15} representation.

3.1.3 Excitons and the concept of Poincaré and Bloch spheres

So far we have considered the bandstructure in terms of a single particle problem, starting with a completely filled VB and a completely unoccupied CB. In contrast, the elementary excitation in a perfect semiconductor upon absorption of a single photon is already a two particle complex, as we generate a VB hole and CB electron simultaneously. In this situation the Hamiltonian of the system is modified as described in Eq. 2.14 and the Coulomb interparticle interaction leads to the formation of excitons. To good approximation, the exciton has a hydrogen-like energetic structure, and by Eq. 2.16 we obtain that even for the highly polar CdSe the Bohr Radius of the exciton ground state extends over many lattice site. This latter point is crucial, as in this limit we can still describe excitons in terms of Bloch equations. In a direct gap semiconductor the relative motion of the electron, the hole and the center of mass motion of the exciton further become separable and hence, the wave-equation of these so-called Wannier excitons can be schematically formed by [Kli05]

$$\Psi_{exc}(\mathbf{K}, n_B, l, m) = \Omega^{-1/2} e^{i\mathbf{K}\mathbf{R}} \psi_e(\mathbf{r}_e) \psi_h(\mathbf{r}_h) \psi_{n_B, l, m}^{env}(\mathbf{r}_e - \mathbf{r}_h) \quad (3.17)$$

where $\mathbf{K} = \mathbf{k}_e + \mathbf{k}_h$ is the wave vector of the exciton, $\mathbf{R} = (m_e \mathbf{r}_e + m_h \mathbf{r}_h)/(m_e + m_h)$ the exciton center of mass, ψ_e and ψ_h the electron and hole wavefunction, respectively, and $\Omega^{-1/2}$ is the normalization factor. The factor $e^{i\mathbf{K}\mathbf{R}}$ describes the propagation of the exciton in the periodic crystal potential in the same spirit as the plane-wave factor in Eq. 3.2 and the hydrogen-like envelope function $\psi_{n_B, l, m}^{env}$ depicts the relative motion of the electron and the hole. As long as the angular momentum is a good quantum number in the crystal, the envelope function quantum numbers n_B , l and m have the exact same meaning as for the hydrogen atom. The symmetry of the exciton then results from the direct product of the symmetries of the electron, hole and envelope function, i. e.

$$\Gamma_{exciton} = \Gamma_{el} \times \Gamma_h \times \Gamma_{env} \quad (3.18)$$

For the exciton ground state ($n_B = 1$) the symmetry of the envelope function is Γ_1 . We thus find for an exciton formed by a Γ_6 electron and a Γ_8 hole[Ivc95]

$$\Gamma_6 \times \Gamma_8 = \Gamma_{15} + \Gamma_{12} + \Gamma_{25} \quad (3.19)$$

Neglecting exchange interaction for the moment, these three resulting levels are energetically degenerate. While the Γ_{12} and Γ_{25} are dipole-inactive, the Γ_{15} level corresponds to the radiative transitions established in Section 3.1.2. For the moment we will only take into account heavy holes, as in the case of QDs the degeneracy with the light hole states will be lifted. Then Eq. 3.19 is readily understood in the following way:

The Coulomb stabilized heavy hole exciton comprises one electron with spin projection $s = \pm\frac{1}{2}$ and one heavy hole with angular momentum projection $j = \pm\frac{3}{2}$, consequently resulting in four energetically degenerate states with a total angular momentum of $\mathbf{J} = \pm 1; \pm 2$. Out of these four only the two states with $\mathbf{J} = \pm 1$ can couple to the light field and are therefore denoted as *bright excitons*, whereas the states with $\mathbf{J} = \pm 2$ are denoted as *dark excitons*. Since in the QDs we are going to deal exclusively with excitons we introduce the resulting four states $|\pm 1\rangle, |\pm 2\rangle$ as new basis.

For optical experiments it is highly convenient to introduce the concept of the Bloch and the Poincaré sphere, as it enables a straightforward interpretation of the optical data. In general, any superposition of the two bright exciton¹ states can be expressed by

$$|\Psi\rangle = \cos\frac{\theta}{2}|+1\rangle + e^{i\phi}\sin\frac{\theta}{2}|-1\rangle \quad (3.20)$$

where θ and ϕ are real numbers with the natural ranges $0 \leq \theta \leq \pi$ and $0 \leq \phi \leq 2\pi$. The geometric interpretation of this equation is the definition of a point on a three dimensional unit sphere, on whose poles we find the orthogonal pure states $|+1\rangle$ and $|-1\rangle$. This is the concept of the *Bloch sphere*.

On the other hand, the polarization state of an arbitrarily polarized light beam is completely characterized in terms of a Stokes vector \mathbf{S} , which is defined as [Azz87]

$$\mathbf{S} = \begin{bmatrix} S_0 \\ S_1 \\ S_2 \\ S_3 \end{bmatrix}, \quad \text{with} \quad \begin{aligned} S_0 &= I_0 = (I_x + I_y) = (I_{x+45^\circ} + I_{y+45^\circ}) = (I_r + I_l) \\ S_1 &= I_x - I_y \\ S_2 &= I_{x+45^\circ} - I_{y+45^\circ} \\ S_3 &= I_r - I_l \end{aligned} \quad (3.21)$$

Here I_0 is the total intensity of the light beam. I_x, I_y, I_{x+45° and I_{y+45° represent the intensities transmitted by an ideal linear polarizer placed in the beampath being adjusted to transmit along the $x, y, x + 45^\circ$ and $y + 45^\circ$ directions. I_r and I_l finally represent the intensities of right- and leftcircular polarization, respectively. The apparent advantage of this formalism is its connection to directly measurable quantities. Using the above definition it is instantly obtained that (partially) polarized light satisfies the (in)equality

$$S_0 \geq \sqrt{S_1^2 + S_2^2 + S_3^2} \quad (3.22)$$

¹This relation holds for any two orthogonal quantum states and is not specific to excitons

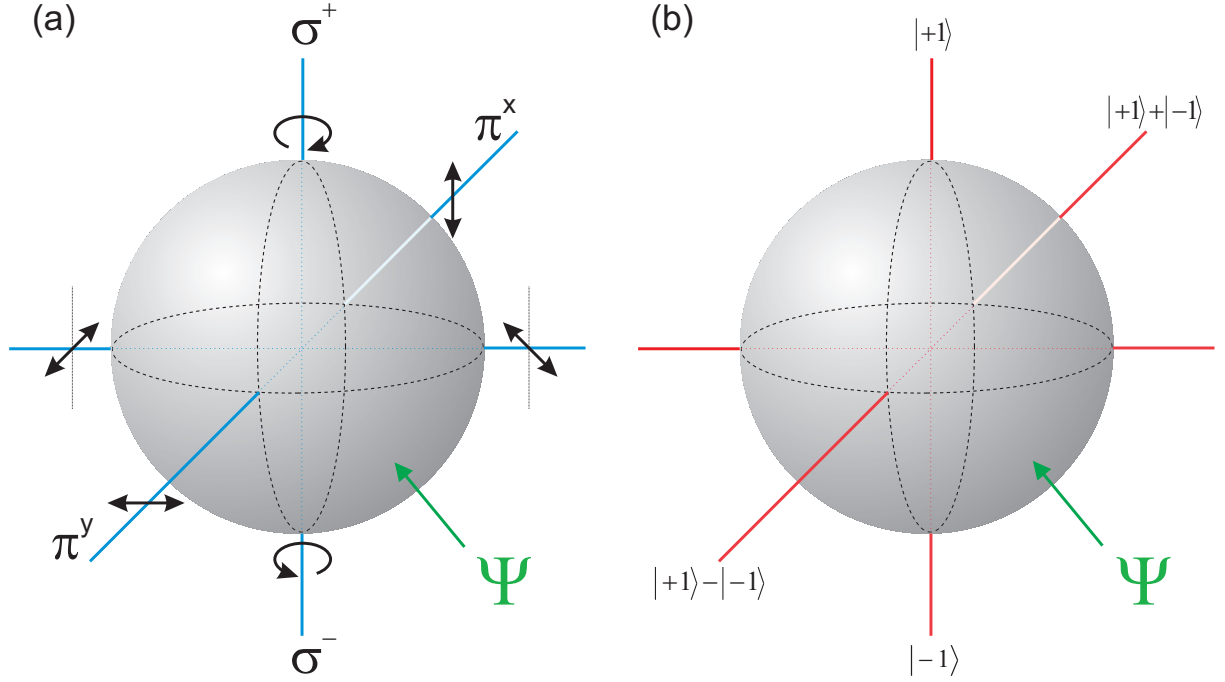


Fig. 3.5: (a) Poincaré sphere representation of a polarized light beam propagating along z -direction: According to the Stokes vector components, the polarization state is described by the π^x , π^y linear polarization components, the $\pm 45^\circ$ slant linear polarization and the σ^+ , σ^- circular polarization components. (b) Bloch sphere representation of the bright exciton states: The state $|+1\rangle$ is represented by the North pole, the state $|-1\rangle$ by the South Pole. The states on the equator correspond to superpositions of $|+1\rangle$ and $|-1\rangle$ with equal weight and different phases. For any given point on the sphere, the diametrically opposite point always describes an orthogonal state

An important quantity in the description of polarized light is further the degree of polarization, which is defined by the ratio of the polarized component and the total intensity. For the three polarization dependent Stokes components one thus finds

$$\rho_v = \frac{I_x - I_y}{I_o}, \quad \rho_l = \frac{I_{x+45^\circ} - I_{y+45^\circ}}{I_o} \quad \text{and} \quad \rho_c = \frac{I_r - I_l}{I_o} \quad (3.23)$$

These states form a convenient basis for the description of the total polarization state of a plane wave. From Eq. 3.22 it is further directly obtained that

$$1 \geq \sqrt{\rho_v^2 + \rho_l^2 + \rho_c^2} \quad (3.24)$$

which means that any polarization state of a given light beam can be described as vector inside of a three-dimensional unit sphere in the above basis. This is the concept of the *Poincaré sphere*.

In the exciton picture the interconnection between these two representation is particularly convenient, as there is a one-to-one correspondance of a given photon state Ψ on the Poincaré sphere and the associated bright exciton state Ψ on the Bloch sphere (see

Fig. 3.5). It is therefore directly recognized, which polarization state is required for a photon in order to generate a distinct exciton state, or - vice versa - which polarization state an emitted photon must have upon recombination of a given exciton state.

3.2 Excitons confined to epitaxial QD nanostructures

Taking into account all of the above we now turn towards excitons confined to embedded QD nanostructures. For perfectly spherical QDs one would expect to observe single, ultra-narrow, only life-time limited transitions. On the contrary, standard photoluminescence (PL) experiments performed at low temperatures yield broadened linewidths with a full width at half maximum (FWHM) varying between 10-100 meV. This effect is readily understood by comparing with topological data of QD structures. As will be shown in Chapter 4 the individual dots that emerge from growth have slightly different properties regarding their size, shape, strain and sometimes even chemical composition. In a standard photoluminescence measurement, one probes $10^8 - 10^{10}$ QDs simultaneously, which naturally gives rise to such an inhomogeneous broadening. The main effect results from the size distribution within such a QD ensemble. In most cases this distribution can be assumed to be Gaussian, in which case it is given by

$$P(R) = \frac{1}{\sqrt{2\pi}\sigma_R} e^{-\frac{(R-R_0)^2}{2\sigma_R^2}} \quad (3.25)$$

where R_0 is the average QD radius with standard deviation $\sigma_R = \sqrt{\langle (R - R_0)^2 \rangle}$. As a consequence the peak position of the broadened spectrum is determined by the average QD size. However, due to the nonlinear dependence of the confinement energy on the QD radius (see Eq. 2.13) the PL energy distribution can become asymmetric. This is most pronounced for very small QD sizes.

A second effect that sometimes contributes to the inhomogeneous broadening is a variation in the QD chemical composition, which gives rise to a shift in the bandgap energies E_0 . Both effects may be present simultaneously. In this case resonant Raman spectroscopy becomes an invaluable tool of analysis, as the compositional fluctuation is accompanied by a variation of intrinsic phonon energies. We will establish later on (chapter 4) how complementary measurements can be used to separate the two effects.

In order to observe single QD emission spectra a variety of experimental techniques have been established over the last 12 years, including sophisticated spectroscopic techniques, such as confocal microscopy and near-field scanning microscopy. Further efforts include advanced growth schemes, which enable a reduction of the areal QD density and therefore increase inter-dot spacing, as well as lithographic patterning of the as-grown dot structures. In the first experiment of this kind on GaAs/AlGaAs QDs, Gammon *et al.* [Gam96] reported the observation of a doublet structure consisting of linearly cross-polarized lines instead of a single sharp exciton ground state transition. This result has

since been confirmed for all investigated epitaxial QD systems and recently even for chemically synthesized nanocrystals (NCs)[Fur06, Hto08]².

It is now well established that this fine structure splitting (FSS) of the exciton arises from the exchange interaction, which couples the spins of the electron and hole (Eq. 2.17). As already pointed out in chapter 2, the exchange term can technically be divided into an analytical short-range term, which describes the probability of finding the electron and the hole in the Wigner-Seitz unit cell, and a nonanalytical long range term, that describes the opposite case. Using the method of invariants first applied to semiconductor systems of reduced dimensionality by van Kesteren *et al.*, the short-range part of the exchange interaction takes the form [vK90, Bla94]

$$\mathcal{H}_{short}^{Exchange} = - \sum_{i=x,y,z} (a_i \hat{J}_i S_{e,i} + b_i \hat{J}_i^3 S_{e,i}) \quad (3.26)$$

where S_e is the electron spin operator, \hat{J}_i are the angular momentum operators (see Appendix B) and a, b are the spin-spin coupling constants. In the basis of the excitonic states $|+1\rangle, |-1\rangle, |+2\rangle$ and $|-2\rangle$ of the heavy-hole subspace, Eq. 3.26 takes the form [Bay02]

$$\mathcal{H}_{short}^{Exchange} = \frac{1}{2} \begin{pmatrix} +\delta_0 & +\delta_1 & 0 & 0 \\ +\delta_1 & +\delta_0 & 0 & 0 \\ 0 & 0 & -\delta_0 & +\delta_2 \\ 0 & 0 & +\delta_2 & -\delta_0 \end{pmatrix} \quad (3.27)$$

with $\delta_0 = 1.5(a_z + 2.25b_z)$, $\delta_1 = 0.75(b_x - b_y)$ and $\delta_2 = 0.75(b_x + b_y)$. From the block diagonal form it is readily seen that the bright and dark exciton states do not mix. As long as the in-plane rotational symmetry is retained (i. e. symmetry $\geq D_{2d}$) one further finds $b_x = b_y$ and therefore $\delta_1 = 0$. In this case the bright exciton states remain energetically degenerate and subsequently decay under emission of $\sigma^{+/-}$ polarized photons. Independently it is found that dark exciton states are energetically split from the bright exciton states. Moreover, they do not remain pure, but rather mix even for high symmetry situations. This is exactly what was already obtained in Eq. 3.19.

If the symmetry is further reduced $b_x \neq b_y$ and therefore $\delta_1 \neq 0$, and as a result the bright exciton states are also energetically split and mixed. In this case, the new eigenstates for the bright excitons are found to be

$$|E1\rangle = \frac{1}{\sqrt{2}}(|+1\rangle + |-1\rangle), \quad \text{and} \quad |E2\rangle = \frac{1}{\sqrt{2}}(|+1\rangle - |-1\rangle) \quad (3.28)$$

which implies that two linearly cross-polarized lines will be present upon radiative recombination. This is exactly what is observed experimentally.

²In contrast to epitaxial QDs, which have a well defined quantization axis due to the growth conditions, NCs are usually randomly oriented, rendering an experimental observation of the splitting challenging

Inclusion of the long range part of the exchange interaction does not change the overall picture, but has an influence on the magnitude of the bright and dark exciton splitting and the splitting of the bright exciton states. The dark exciton states remain unaffected. It can technically be included by replacing the subblock that works on the bright exciton states in Eq. 3.27 with [Bay02]

$$\mathcal{H}_{include\ long}^{Exchange} = \begin{pmatrix} +\Delta_0 & +\Delta_1 \\ +\Delta_1 & +\Delta_0 \end{pmatrix} \quad (3.29)$$

with $\Delta_0 = \delta_0 + \gamma_0$, where γ_0 accounts for the long range contribution of the dark-bright exciton exchange splitting, and $\Delta_1 = \delta_1 + \gamma_1$, with $\gamma_1 = \gamma_x - \gamma_y$. Here γ_x and γ_y are the long range exchange coupling constants of the bright exciton states, which means that γ_1 only becomes important if the dot is shape-asymmetric. The overall energetic structure of heavy-hole excitons confined to QD nanostructure as function the symmetry of the confining potential is summarized in Fig. 3.6.

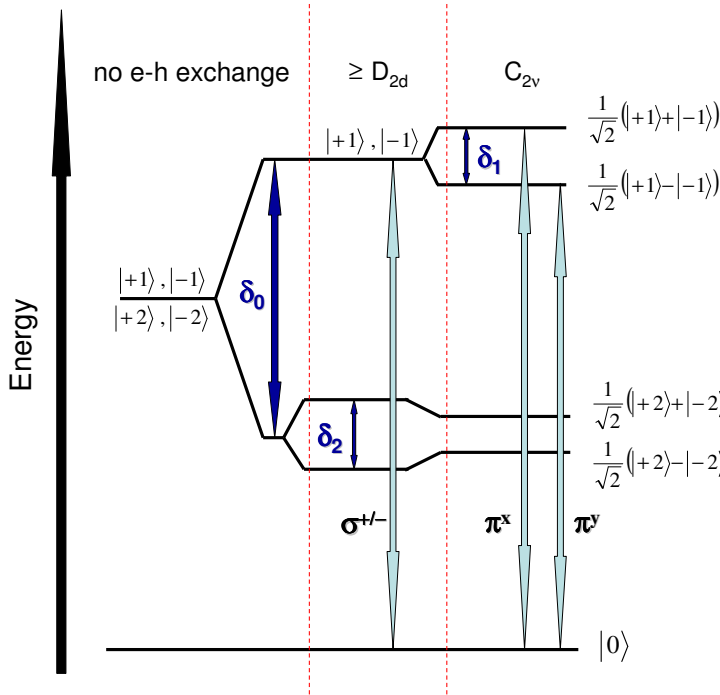


Fig. 3.6: Evolution of the excitonic eigenstates and their relative energetic structure when taking into account the e-h exchange interaction as a function of the underlying symmetry. Light blue arrows indicate radiative recombination from the dipole-active bright exciton levels to the excitonic ground state $|0\rangle$, the respective polarization is labelled accordingly.

From the experimental point of view the short and long range contributions of the exchange interaction are barely separable. Puls *et al.* [Pul99] performed single dot spectroscopy experiments on CdSe/ZnSe QDs in inclined magnetic fields, by which they were able to extract the magnitudes of the splittings of both the dark and bright exciton states (for the bright-dark exciton mixing in magnetic fields see Section 3.2.1). As they found the magnitude of the bright exciton splitting to be one order of magnitude larger, they were able to identify the long range contribution of the exchange interaction to be the dominating contribution for the bright exciton splitting, since from the above it is clear that for the short range contribution $\delta_2 \geq \delta_1$ will hold for all cases.

While the above considerations, which are solely based on symmetry considerations, excellently recover the overall energetic structure of excitons confined to QD nanostructures, the *magnitudes* of the splittings are not easily linked to their microscopic origin and have been subject to a lively debate in recent years. There are numerous reasons that lead to a decreased symmetry of the QD including shape asymmetry, strain, strain-induced piezoelectricity and alloy admixture. The experimentally reported bright exciton splittings scatter on a large scale from only a few μeV up to several meV (see e. g. [Fin02, Lan04]) without establishing any clear trends or material specific energy regions.

Seguin *et al.* [Seg05] determined the bright exciton splitting in InAs/GaAs QDs as a function of QD size and reported a general increase of the absolute magnitude with increasing QD size accompanied by a sign change for small QDs. Their model calculations in the frame of eight-band $\mathbf{k} \cdot \mathbf{p}$ theory pinpointed piezoelectricity as the only effect able to follow this trend. This is consistent with theoretical work by Bester *et al.* [Bes06] in which the magnitude of the splitting was linked to the QD morphology in the frame empirical pseudopotential calculations, signifying the importance of even second order piezoelectric terms in the presence of large strains.

On the other hand Htoon *et al.* [Hto08] report an increase of the FSS with decreasing nanoparticle size scaling as $\frac{1}{\sqrt{V}}$ for QD nanocrystals, which is in agreement with theoretical work when strain and piezoelectricity are negligible [Gou06]. This is highlighting the sensitive interplay of shape, strain, strain-induced piezoelectricity and alloy composition in embedded QD structures and shows, how competing mechanisms following different scaling laws render a quantitative microscopic description of the FSS a formidable task, that is still beyond current capabilities.

Moreover, the reduction of the symmetry is accompanied by a mixing of the HH and LH valence band states. Here, two effects have to be considered. For one, any in-plane asymmetry of the confining potential will introduce nondiagonal terms in the Kohn-Luttinger Hamiltonian [Boc92a]. This mixing results in different oscillator strengths for linearly polarized transitions from the exchange split exciton levels, whose polarization direction is set by the principal axes of the confinement potential. Very large asymmetries of the confining potentials are required for this effect to be important, which means that it is usually only a minor correction in QDs.

A mixing of the HH and LH subbands may further be caused by anisotropic strain in the QD plane through the Bir-Pikus Hamiltonian. This mixing also gives rise to a linear polarization degree. Its respective direction is imposed by the strain distribution, meaning the resultant polarization direction can be rotated with respect to the principal axis of the asymmetric confining potential. This kind of valence band mixing has been found to be significant in MBE grown CdTe/ZnTe QDs [Lég07], which also has important consequences for the magnetic properties, as it gives rise to a large in-plane hole g-factor.

For sake of completeness it shall be noted, that all of the above assumes that angular momentum remains a good quantum number. This situation can change if, by alloy admixture, completely asymmetric strain or totally irregular shape, no recognizable

symmetry of the system remains. In this case one faces a heavy mixing of all states involved and optical interband transitions and their respective polarizations become hard to analyze, if they yield any useful information at all.

3.2.1 Neutral excitons in magnetic fields

The interaction of the electron and the heavy-hole spin with an external magnetic field $\mathbf{B} = (B_x, B_y, B_z)$ of arbitrary strength and orientation is given in its general form by [Pik93, Pik94]

$$\begin{aligned} \mathcal{H}_{Zeeman} = & \frac{1}{2}\mu_B [g_{e\parallel}\sigma_z B_z + g_{e\perp}(\sigma_x B_x + \sigma_y B_y)] \\ & + g_0\mu_B \left\{ \kappa(\hat{J}\mathbf{B}) + q_0 \left[\sum_{i=x,y,z} \hat{J}_i^3 B_i + q_1 (\hat{J}_x^3 B_y + \hat{J}_y^3 B_x) \right] \right\} \end{aligned} \quad (3.30)$$

where μ_B is the Bohr magneton, g_0 , $g_{e\parallel}$ and $g_{e\perp}$ are the g-factors of a free electron and an electron confined to a QD for $\mathbf{B} \parallel z$ and $\mathbf{B} \perp z$ (with z defining the growth direction), $\sigma_{x,y,z}$ are the Pauli-matrices, $\hat{J}_{x,y,z}$ is the angular momentum operator relating to the heavy hole (see Appendix B) and κ and q_0 are the Luttinger coefficients [Lut56]. The factor q_1 is introduced for QDs displaying an in-plane asymmetry for the x and y axis and is C_{2v} -invariant [Pik94]. For QDs of symmetry $\geq D_{2d}$ the factor $q_1 = 0$ and the last term of Eq. 3.30 vanishes.

For the current work we limit the discussion to the case of $\mathbf{B} \perp z$ as we are interested in the in-plane asymmetry of the QDs under study. We further limit ourselves again to excitons consisting of one electron and one heavy-hole, that is we neglect the valence band mixing. We will see in the results that the influence of the LH bands is negligible for small CdSe/ZnSe QDs. With z as the axis of quantization the heavy holes have zero spin projection in the QD plane and therefore the first hole term in Eq. 3.30 becomes zero. In the basis of the excitonic states $|+1\rangle$, $| -1\rangle$, $|+2\rangle$ and $| -2\rangle$ we then find

$$\mathcal{H}_{Zeeman}^{\perp} = \frac{1}{2} \begin{pmatrix} 0 & 0 & \delta_{el} & \delta_{hh} \\ 0 & 0 & \delta_{hh}^* & \delta_{el}^* \\ \delta_{el}^* & \delta_{hh} & 0 & 0 \\ \delta_{hh}^* & \delta_{el} & 0 & 0 \end{pmatrix} \quad (3.31)$$

where $\delta_{el} = \mu_B g_{e\perp} B_{\pm}$ and $\delta_{hh} = \mu_B (g_{hh}^i B_{\pm} + i g_{hh}^a B_{\mp})$ are the in-plane Zeeman terms for electrons and heavy-holes, respectively; $g_{hh}^i = \frac{3}{2} g_0 q_0$ and $g_{hh}^a = \frac{3}{2} g_0 q_1$ are the isotropic and anisotropic contributions of the heavy hole g factor and $B_{\pm} = B e^{\pm i\phi}$ are the effective magnetic fields.

It is readily seen from Eq. 3.31 that in-plane magnetic fields lead to a mixing of the dipole allowed and dipole forbidden states. Explicitly, the precession of the electron spin couples the $|+1\rangle$ to the $|+2\rangle$ and the $| -1\rangle$ to the $| -2\rangle$ exciton, while the precession

of the hole results in a coupling of the $|+1\rangle$ and $|-2\rangle$ states as well as the $|-1\rangle$ and $|+2\rangle$ excitons. By carefully measuring the energetic position and polarization state of the excitonic transitions in dependence of the orientation and magnitude of an external magnetic field, it therefore is possible to restore the full energetic structure of the heavy-hole exciton [Pul99].

As the absolute values of q_0 and q_1 are very small compared to κ , it is sometimes argued that the nonlinear terms in Eq. 3.30 are negligible for inclined magnetic fields (e. g. [Dor03]), which means that $\delta_{hh} = 0$ in Eq. 3.31. We shall show that such an approach even qualitatively fails to describe the polarization behavior of excitons in QDs subject to in-plane magnetic fields, and despite the fact that $q_1 \ll q_0$ only inclusion of q_1 succeeds in explaining the optical response of low symmetric QD to in-plane magnetic fields (see chapter 6).

3.2.2 Exciton complexes in the absence of magnetic field

Besides the elementary two-particle excitation of the above discussed exciton a wealth of excitonic complexes has been discovered in QDs, out of which two shall be discussed briefly in this section. They arise from charging additional carriers, electrons or holes, into QDs and have been subject to intensive studies both experimentally and theoretically in the light of possible QD applications.

Trions. The energetic structure of the exciton is distinctly altered if a single additional carrier is charged into the QD, as its appearance changes the spin of the system from integer to half integer. As such, the energetic fine structure as well as the optical properties are profoundly changed, since regardless of the QD symmetry the eigenstates of the trion must be doublets degenerate in the absence of magnetic fields according to Kramer's theorem. A detailed discussion for the resultant energetic structure has been elaborated by K. V. Kavokin [Kav03], which we shall outline for the case of a singly negatively charged exciton (the situation is, however, interchangeable for singly positively charged excitons). In this configuration the two electrons and the hole can form eight states, out of which two states are singlet states, where both electrons occupy the lowest confined electron state of the QD, and six are triplet states, which require one electron to be in a higher confined QD state and are therefore shifted to much higher energies.

Hence, the singlet ground state of the trion consists of two electrons with antiparallel spin and one hole. As a consequence, the total electron spin S is zero and the electron-hole exchange interaction vanishes, leading to a single nonpolarized transition without finestructure. This change in the optical decay path is most interesting for application, as it enables *electrical* control of the *optical* QD properties upon intentionally charging additional electrons into the QDs, which has been demonstrated in appropriately gated QD structures [Hög04].

The triplet trion states are not directly observable in photoluminescence but can be invoked in the decay path of more complex exciton systems. In this configuration the

electrons with spin $S = 1$; $S_z = 0, \pm 1$ and the heavy hole with angular momentum projection $j_z = \pm 3/2$ form an overall of six states, which are split by the electron-hole exchange interaction into three doublets with $\mathbf{J} = \pm 1/2, \pm 3/2, \pm 5/2$, where $\mathbf{J} = S_z + j_z$. The magnitude of this sublevel splitting has been found to be of the same order of magnitude as the singlet-triplet level splitting [Aki05]. It is therefore massively enhanced with respect to the e-h exchange observed in uncharged excitons, which is attributed to the enhanced anisotropy of the higher order wave functions of the second electron.

Biexcitons. The formation of biexcitons has first been predicted by M. A. Murray in 1958 [Mur58]. Due to the enhanced binding energy of excitonic complexes in QDs biexcitons are robustly observable at low temperatures in a variety of QD material systems. According to Hund's rule the biexciton ground state has a total spin of $\mathbf{J} = 0$, which means that the individual spins of the excitons contained align antiparallel. Like all decay processes in QDs, the biexciton and exciton transition are sequential. In the case of highly symmetric QDs the situation is therefore very similar to polarization-correlated decay cascades observed in atoms [Koc67], which were of central importance in the experimental establishment of the quantum nature of light [Asp81]. The corresponding biexciton cascade is shown schematically in Fig. 3.7.

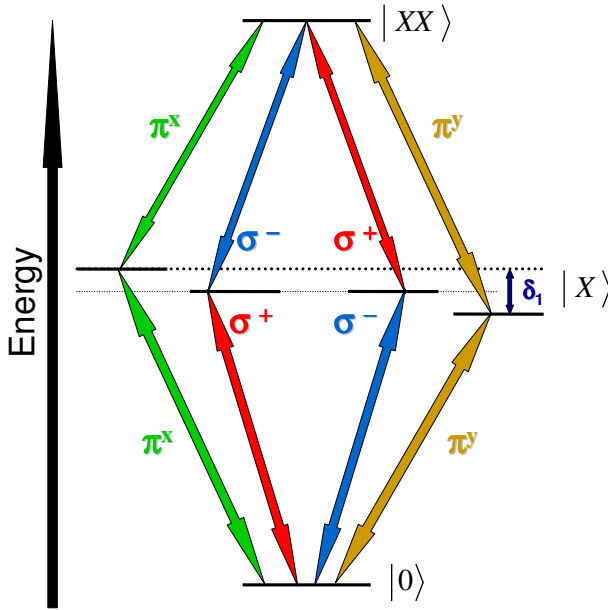


Fig. 3.7: Level scheme of the biexciton cascade in high symmetry (D_{2d}) and low symmetry (C_{2v} or below) QDs. The exciton and biexciton photons have different energies as a result of the additional binding energy of the biexciton, but as long as D_{2d} symmetry is retained their polarization is maximally entangled. For low symmetry QDs the anisotropic exchange interaction δ_1 lifts the degeneracy of the exciton states, which results in two distinguishable recombination paths.

For QDs of symmetry $\geq D_{2d}$ there is equal probability for the $|XX\rangle \rightarrow |X\rangle$ photon to be left- or rightcircularly polarized. The subsequent $|X\rangle \rightarrow |0\rangle$ photon is then necessarily circularly polarized the opposite way. This complete anticorrelation in optical polarization corresponds to a maximally entangled state described by

$$\begin{aligned}
 |\psi\rangle &= \frac{1}{\sqrt{2}} (|\sigma_{xx}^+ \sigma_x^- \rangle + |\sigma_{xx}^- \sigma_x^+ \rangle) \\
 &= \frac{1}{\sqrt{2}} (|H_{xx} H_x \rangle + |V_{xx} V_x \rangle)
 \end{aligned} \tag{3.32}$$

where $\sigma_{xx}^{+/-}$ and $\sigma_x^{+/-}$ are the polarization states of the biexciton and exciton photon, respectively. The second line in Eq. 3.32 describes the same state in the basis of vertical (V) and horizontal (H) linear polarization (this is π^y and π^x). For further information on the interconnection of polarization correlation and entanglement the reader is referred to the nice introduction to Quantum Optics by M. Fox [Fox06].

O. Benson *et al.* were the first to point out that the biexciton cascade could be used to generate non-classical light on demand within a semiconductor device scheme [Ben00]. They proposed a monolithic structure in which a QD active layer was embedded in a $p-i-n$ junction and surrounded by a microcavity. However, as described in the previous section, any real QD is subject to intrinsic asymmetry and the resulting FSS of the exciton states gives rise to two distinguishable decay paths for the biexciton cascade, which are hence classically correlated.

Several methods have been investigated to overcome this obstacle. They can be grouped roughly into two categories. The first is to study ways of manipulating the FSS directly. This is closely related to the subject of the current *Thesis* as it is heavily concerned with the interplay of QD symmetry and optical anisotropy. It was demonstrated in the III-Vs [Lan04] and the II-VIs [Mar07], that the FSS can be substantially reduced by post-growth annealing and eventually even be inverted [You05]. However, annealing will not result in a controlled symmetrization of the QDs. Other approaches rely the application of an external perturbation. Quite recently, it was demonstrated also in the III-Vs that in-plane electric fields are capable of tuning the FSS and even completely suppressing it [Ger07]. So far, no understanding on a microscopic level has been achieved concerning this result. A general flaw of these investigations is also the poor reproducibility, which results from random charging of defects in the vicinity of QDs. In effect, neither direction nor absolute strength of the electric field can be monitored reliably during these experiments. Finally, one can study the interplay of the FSS and in-plane magnetic fields. This is done in-depth in section 6.2 of the current work. In parallel work, Stevenson *et al.* claimed that they had been able to generate anti-correlated photons through the latter [Ste06b]. It was later on demonstrated that in fact their data was insufficient to back that claim [Lin06, Gil07]. On balance, means of manipulating the FSS have not yet led to a convincing demonstrating of the generation of nonclassical light.

The second direction is aimed towards an effective elimination of the 'which-path' information in the FSS biexciton cascade and thereby restoring the indistinguishability between both decay paths. T. M. Stace *et al.* proposed to use a leaky optical cavity with pairs of degenerate cavity modes coinciding with the nondegenerate exciton transition energies [Sta03]. They computed that such a non-ideal cavity would still be able to produce partially entangled photon pairs. A. Akopian *et al.* demonstrated experimentally that the 'which path' information can successfully be erased by spectral filtering [Ako06]. They used a spectrally resolved Hanbury Brown and Twiss setup [HB56], which they tuned into the narrow spectral region where the two FSS exciton states overlap and could show convincingly that the post-selected photon pairs satisfied the Peres criterion

of entanglement [Per96]. This work has to be considered an important proof-of-concept experiment but additional effort is necessary to actually introduce the idea into a real device scheme. Very recently, R. Johne *et al.* suggested to couple the biexciton cascade to the modes of an asymmetric photonic crystal [Joh08]. Their analysis showed, that the resultant polariton modes can be strongly entangled in the case of strong coupling.

Summarizing, the biexciton-exciton decay cascade has recently gained immense interest in the context of nonclassical light sources and is considered a perspective candidate for a technical realization of the latter. It is therefore that the appearance of the e-h exchange induced FSS is mostly reputed unwanted. As shall be shown in the remainder of this work, this general attitude misses the point that in fact other interesting effects may arise from the FSS and novel physics can be observed in an anisotropic fully confined system.

Chapter 4

Quantum dot fabrication

This chapter is dedicated to the details of the quantum dot growth methods used to fabricate the QD nanostructures studied in the present work, which is done by variants of Molecular Beam Epitaxy (MBE). More specific, we have employed different approaches of self-assembled MBE growth, accompanied by structural investigations to provide an efficient understanding of the resultant QD morphology and composition. Unlike in their III-V and group-IV counterparts, the peculiarities of the QD formation are not well understood in the II-VIs. The interconnection of the QD growth and the resultant electronic and optical properties is therefore a key element for the investigations in the current work.

We shall start out with a very brief introduction of the mechanisms of MBE growth in general. In this context the apparatus used in the present work is introduced. From this we briefly summarize important aspects of the present understanding of self-organized QD growth, which stands out as the method of choice for the fabrication of the current semiconductor QD generation. The presumable ease of integration of such grown QD nanostructures into existing semiconductor devices or technologies in addition to time- and cost-effective fabrication when compared to lithographic methods are generally accepted preferences of MBE growth. We hence elaborate on the the formation of II-VI QDs and explicitly show how the CdSe/ZnSe heterosystem distinguishes from the widely studied InAs/GaAs heterosystem.

From this general characteristics we then turn to the details of the growth methods employed for the fabrication of the QDs that were studied in the current work. First, QDs resulting from conventional MBE growth at a growth temperature of 300° C will be presented. Second, a technique that combines low temperature growth and in-situ annealing is discussed. On both structural information is provided concerning the resultant QD shape and composition. The chapter is closed by a comparative survey of the photoluminescence data of the QDs arising from the above methods, which motivates the sample choice for the remainder of the work.

4.1 General remarks on molecular beam heteroepitaxy

With the term *epitaxy* one specifies growth of a single crystalline layer upon (*epi*) a crystalline substrate, by which the orientation order (*taxis*) of the layer is determined by the orientation of the substrate. If the substrate and the deposit layer are identical the process is designated as *homoepitaxy*, if the materials are different the designation is *heteroepitaxy*.

In molecular beam epitaxy the growth is performed via the interaction of one or several atomic or molecular beams on the surface of a single crystalline substrate, which is kept at a defined temperature. The molecular (or atomic) beams are provided by sublimating ultra-pure solid material from an effusion cell, whose idealization is described by the Knudsen cell, into vacuum. Real effusion cells are technically more complex but follow the same conceptual ideas.¹ For the mean free path of the molecular beams to be on the order of the geometrical chamber size and the necessity of ultra low residual background pressures for growing sufficiently clean epilayers, Ultra High Vacuum (UHV) operation is required.

The composition of the layer is controlled by regulating the incoming molecular beams by opening and closing mechanical shutters, whereas the growth rate is determined by carefully varying the temperature of the effusion cells and therefore the flux intensity. To improve growth homogeneity the sample is mounted on a rotating holder. An archetypical MBE-system as used in the present work is displayed in Fig. 4.1.

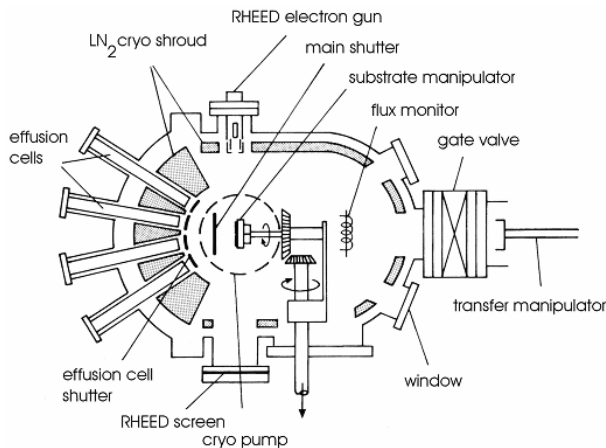


Fig. 4.1: Schematic side view of the MBE chamber (Riber 32 design).

The UHV environment is well suited for in-situ characterization by RHEED (Reflection High Energy Electron Diffraction), which enables realtime monitoring of the layer by layer growth and is further capable of providing valuable information the surface reconstruction. This also holds for in-situ x-ray diffraction, which is, however, not as commonly used.

The MBE cluster operated by the EP3 at the University of Würzburg consists of

¹For a detailed description of the effusion cell see e. g. [Win62] and references therein.

an overall of six MBE chambers, one metallization chamber and one sputter chamber, each of which are interconnected through an UHV transfer module. This setup enables high quality growth of complex structures containing diversified materials by performing sequential growth steps in different, specialized growth environments.

For the QD growth only two chambers are of relevance. All samples studied in this thesis were grown on commercial epi-ready GaAs:Si(001) substrates of Wafer Technology Ltd., UK. Because of air exposure these samples naturally come with an oxide overlayer upon delivery, which has to be removed prior to growth start. To smoothen the then rippled GaAs surface and provide clearly defined growth conditions a 200 nm nominally undoped GaAs buffer layer is grown first. This first step is performed in the GaAs chamber (RIBER 32 design) that is equipped with sources of elemental Ga, Al, Sb, In, Be (for p-type doping), Si (for n-type doping) and As. Evaporation of the latter is done by a special valved cracking effusion cell (VECCO EPI 500 V-S). For the actual QD growth the sample is then transferred to the II-VI chamber, in which all QD samples investigated in this work were grown. This chamber (also RIBER 32 design) is equipped with cells of elemental Zn, Cd, Mg, Te, Se, ZnS, Mn and Al. Both chambers are fully automatized and can be completely controlled via computer. For growth monitoring they are equipped with flux meters and RHEED guns.

4.2 Self-assembled quantum dot growth

The driving force for self-assembled growth of crystallographically coherent, i. e. defect free QDs, is generally assumed to be *elastic* relaxation of strain that is built up in the deposit layer. This strain is a natural result from the heteroepitaxy of two bulk lattice mismatched material systems. During the initial stage of the growth process the deposit layer adopts the lattice constant of the substrate material and as long as no relaxation takes place it is hence *pseudomorphically* strained. Under these conditions the growth is accompanied by a built-up of deformation energy that grows linearly with the thickness of the deposit layer. In case of compressive strain, i.e. if the bulk lattice constant of the epi-material is larger than that of the substrate, a possible relaxation path of the deformation energy is the formation of 3D islands.

Two requirements have therefore to be met for a semiconductor material combination to crystallize nanoscale islands that can confine carriers in all three spatial directions: First, the material which is supposed to form the QDs must have a lower band gap than the embedding material, in order to form confining potentials defined by the difference in band gaps. Second, the QD forming material must have a larger lattice constant than the host material.

These conditions are obviously fulfilled for a variety of combinations of II-VI and III-V compounds and group IV semiconductors, as can be depicted from Fig. 4.2. The most widely investigated material combinations are InAs on GaAs(001) and Ge on Si(001)

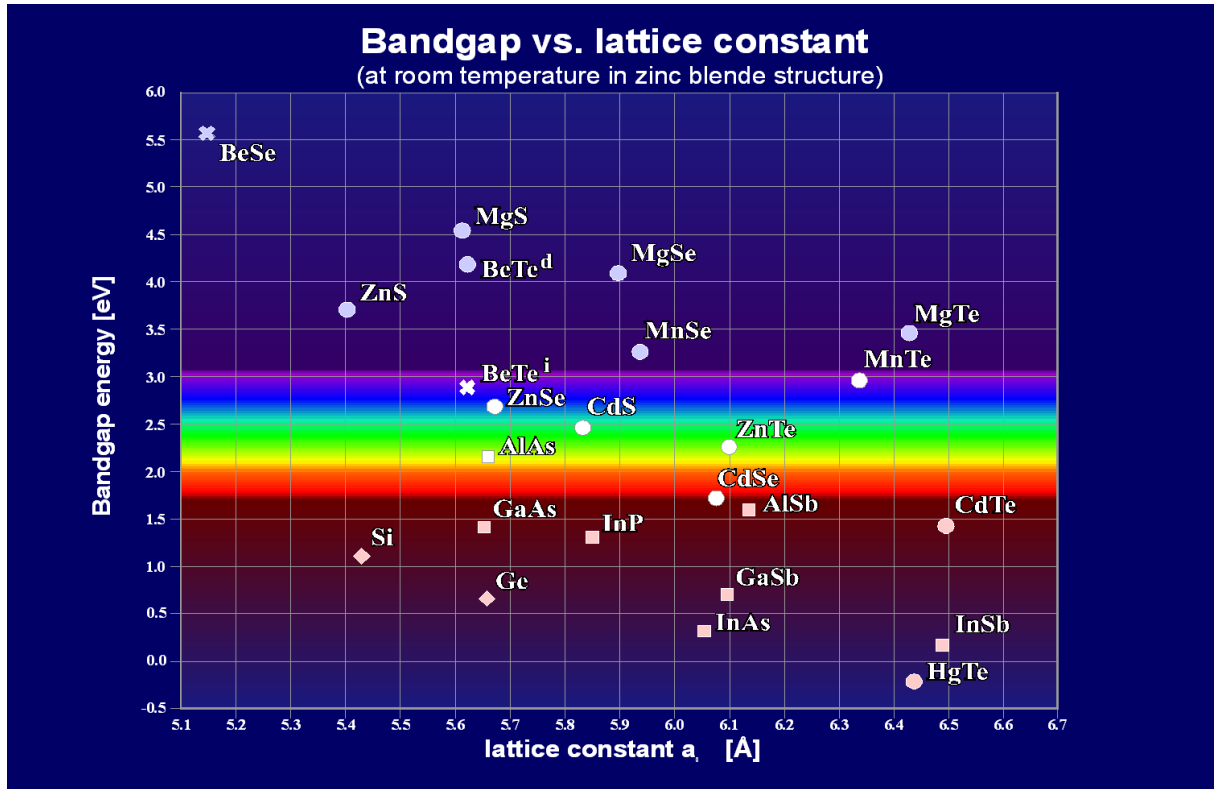


Fig. 4.2: Selected II-VI, III-V compound and elemental group IV semiconductor lattice constants vs. bandgap. Circles denote II-VI compounds, squares III-V compounds and diamonds group IV elements.

and in both systems a profound understanding of the epitaxial growth mechanisms is established today. This is in stark contrast to self-assembled growth of CdSe QDs on ZnSe(001). With a lattice mismatch of 6.7 % at 300 K, the CdSe/ZnSe heterosystem is at first glance very similar to InAs/GaAs. On closer look, however, the systems are distinctly different. First, the III-V bonds are mostly covalent in nature, whereas the II-VI bonds are considerably ionic. Second, InAs and GaAs both crystallize in zinc-blende structure in their bulk phase. While this is also the case for ZnSe, bulk CdSe crystals form in wurtzite phase. Finally, and in this context most important, the vapor pressure of ZnSe and CdSe is by orders of magnitudes larger than that of InAs and GaAs. This results in decisively lower growth temperatures for CdSe on ZnSe, typically 70-250° lower than for InAs on GaAs. For the epitaxy of CdSe on ZnSe we therefore find completely different growth conditions. A detailed survey of the peculiarities of II-VI epitaxy is beyond the scope of the current work, but we shall summarize the major aspects.

The formation of morphological QDs in III-V compound semiconductors is ascribed to the Stranski-Krastanow growth mode, which describes the crystal growth at the thermodynamic equilibrium [Her99]. In this picture the formation of 3D islands is basically a trade-off between the relaxation of deformation energy in the layer and gain of additional surface energy through the formation of the 3D islands, which thus initially acts

as energetic barrier preventing immediate 3D growth. The resulting growth sequence is summarized in Fig. 4.3. In the initial stage a pseudomorphically strained quasi-2D layer (termed *wetting layer*) forms until the deformation energy equals the gain of surface energy. This point signifies the critical layer thickness t_C . Beyond this point the epi-system relaxes the misfit induced elastic energy through the formation of 3D islands.

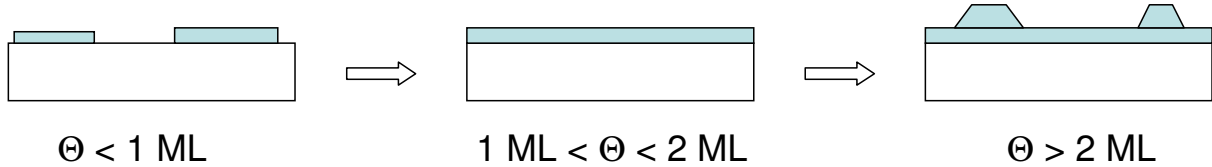


Fig. 4.3: Sequence of equilibrium Stranski-Krastanow growth mode. Here it is explicitly assumed that the critical layer thickness t_C is below two monolayers.

Two experimental observations serve as clear indicators of Stranski-Krastanow-like growth. For one, the structural transition from 2D to 3D is directly observable during growth in the RHEED pattern, which changes from streaky for quasi-2D to spotty for 3D crystallization. Furthermore, the transition is observed in photoluminescence measurements of the QD ensemble, as displayed in Fig. 4.4. Beyond the critical surface coverage, the peak energy of the QD ensemble luminescence undergoes a drastic discontinuous red-shift that is accompanied by a massive spectral broadening, which results from the size distribution of the QDs.

Both features are not always clearly established for the formation of CdSe/ZnSe QDs. While the Stranski-Krastanow mode models growth under thermodynamic equilibrium

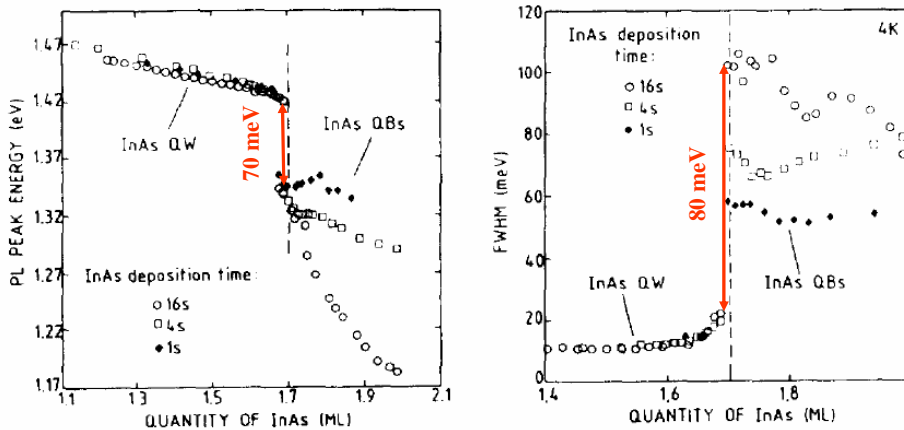


Fig. 4.4: Signature of the Stranski-Krastanow transition in InAs/GaAs detected by photoluminescence. The QD ensemble peak luminescence and full width at half maximum (FWHM) are plotted versus InAs deposition for different deposition times. For material deposition above the critical thickness t_C the ensemble luminescence is massively red-shifted and spectrally broadened. Adopted from [Sei96].

conditions and thus quasi-reversible, real MBE growth is signified by conditions far from the thermodynamic equilibrium. It is therefore evident that a pure thermodynamic description is an oversimplification and one can expect that kinetic effects play a decisive role the QD formation process.

An important alternative pathway for the relaxation of misfit strain is atom interdiffusion between the host and the QD-forming materials. By reducing the bulk lattice mismatch according to Vegard's law, the 2D to 3D growth transition can be delayed or even completely suppressed. Interdiffusion and concomitant alloying have been reported for InAs/GaAs [Joy98], Si/Ge [Cha99] and CdSe/ZnSe [Per00] and are, not surprisingly, found to be heavily dependent on the growth temperature.

A further purely kinetic phenomenon that can also give rise to 3D-like crystallization is mounding. The formation of a complete monolayer is not an instantaneous event but starts with formation of quasi 2D clusters. As these 2D clusters increase in lateral size so does the probability that atoms from the vapor phase crystallize on top of them rather than in between. In order to maintain perfect layer-by-layer growth as assumed in thermodynamic equilibrium, both adatom intra- and interlayer diffusion need to be fast. If the adatom down-climb is hindered for some reason, mounding occurs and one finds the case of multilayer growth. Physically, this scenario can arise due to step edge barriers, also known in the literature as Ehrlich-Schwoebel barriers, which result from dangling bonds at the surface and therefore render it energetically unfavourable for the adatoms to occupy places next to step edges.

Thermodynamic and kinetic aspects of QD growth are usually intertwined and can not generally be separated. Due to the higher growth temperatures in the III-Vs adatom surface diffusion is much more effective than in the II-VI and the system is described well in terms of a thermodynamic equilibrium model. In contrast, kinetic effects have a huge impact on the growth dynamics in the II-VI, eventually to an extent, where the actual QD formation is completely dominated by surface kinetics and strain only plays a minor role. Likewise, QD fabrication by MBE is not entirely understood in the II-VIs, and the resulting QDs can differ significantly concerning their morphological, chemical and consequently electronic and therefore optical properties. It is hence imperative to have a close eye on the QD system under investigation in order to classify experimental results.

Unfortunately, morphological studies of the as-grown QDs are not easily linked with investigations on their electronic and optical properties, which explains the relative lack of such information in the literature. In order to avoid surface recombination centers and to obtain well defined chemical potentials, the QD nanostructures are routinely covered with additional material of the embedding semiconductor. This capping, however, is not at all a simple encapsulation procedure, but instead can modify the QDs significantly. Commonly observed effects are vertical truncation in combination with lateral expansion of the QD nanostructures. In the CdSe/ZnSe system the growth kinetics during capping can further heavily modify the QD material composition. Passow *et al.* performed detailed studies by high resolution x-ray diffraction and high resolution transmission-electron microscopy

in which they established that the actual Cd content in the QD forming layer can be significantly reduced relative to the nominal coverage depending on the exact growth conditions [Pas01]. With growth temperatures below 300° C this observation cannot be ascribed to CdSe desorption, which does not occur up to 330° C. It is however known from previous studies, that the sticking coefficient of Cd is markedly reduced by the presence of Zn in group II rich conditions, which results in a partial replacement of Cd by Zn under Se deficiency conditions [Iva98]. This is readily understood by the ~ 0.7 eV difference in the formation enthalpies of ZnSe and CdSe in favour of ZnSe. Bearing the above in mind the authors explain their observation by a segregation model, that accounts for partial redesorption of Cd during capping. Such a segregation-enhanced etching of Cd during Zn deposition is further corroborated by recent results [Kru07], where the composition of the layer was monitored in real time during growth by time resolved in-situ ellipsometry.

Summarizing, one has to compare data on the morphological, structural and optical properties of the resulting islands with great caution and the establishment of a clear cut picture is most often only possible upon comparing experimental results of complementary methods. It is therefore imperative to summarize the main aspects of the growth conditions before going into the results of the optical studies.

4.3 Growth variants of CdSe/ZnSe quantum dots

The optical properties of QDs emerging from two different MBE growth variants were studied and compared in the current work. In order to establish a comprehensive understanding of the resultant CdSe/ZnSe QD nanostructures, it is necessary to summarize the main aspects of the QD fabrication procedures. We will not dwell into peculiarities of QD formation here but rather summarize the experimentally established structural and morphological properties of the QDs. The details of the growth processes were investigated in great detail and are nicely summarized by S. Mahapatra [Mah07a].

4.3.1 Conventional MBE growth

For all samples grown by this method the growth temperature was set to $T_G = 300^\circ \text{C}$ throughout the complete growth sequence. In the samples designated for optical studies a 300 nm thick lattice matched $\text{Zn}_{0.97}\text{Be}_{0.03}\text{Se}$ layer was grown prior to the QD matrix, which is supposed to act as an energetic barrier to avoid unwanted photocarrier diffusion into the substrate. The QDs were hence formed by the deposition of one to four monolayers (ML) of CdSe on a 50 nm thick pseudomorphic ZnSe(001) layer. After a growth interruption of 10 seconds under Se flux the samples were capped by another 25 nm of ZnSe. Additional uncapped samples were grown for topological studies.

No streaky to spotty RHEED transition was observed for any CdSe coverages, thus the streaky pattern characteristic for the 2×1 reconstruction of a Se terminated quasi

2D CdSe surface persisted through the complete sequence. An Atomic Force Microscope (AFM) picture of the surface of an uncapped one ML sample is displayed in Fig. 4.5.

The nanostructures arising from the above growth sequence are about 1 nm high and below 10nm in lateral dimensioning. The lateral features are likely to be even smaller as the in-plane resolution is limited by the AFM tip size of about 12 nm. The inter-structure distance is extremely small and extrapolating from the AFM picture one obtains a very high areal structure density of above 10^{11} cm $^{-2}$. Most notably, the features exhibit a distinct shape asymmetry, clearly elongating along the [110] crystal axis.

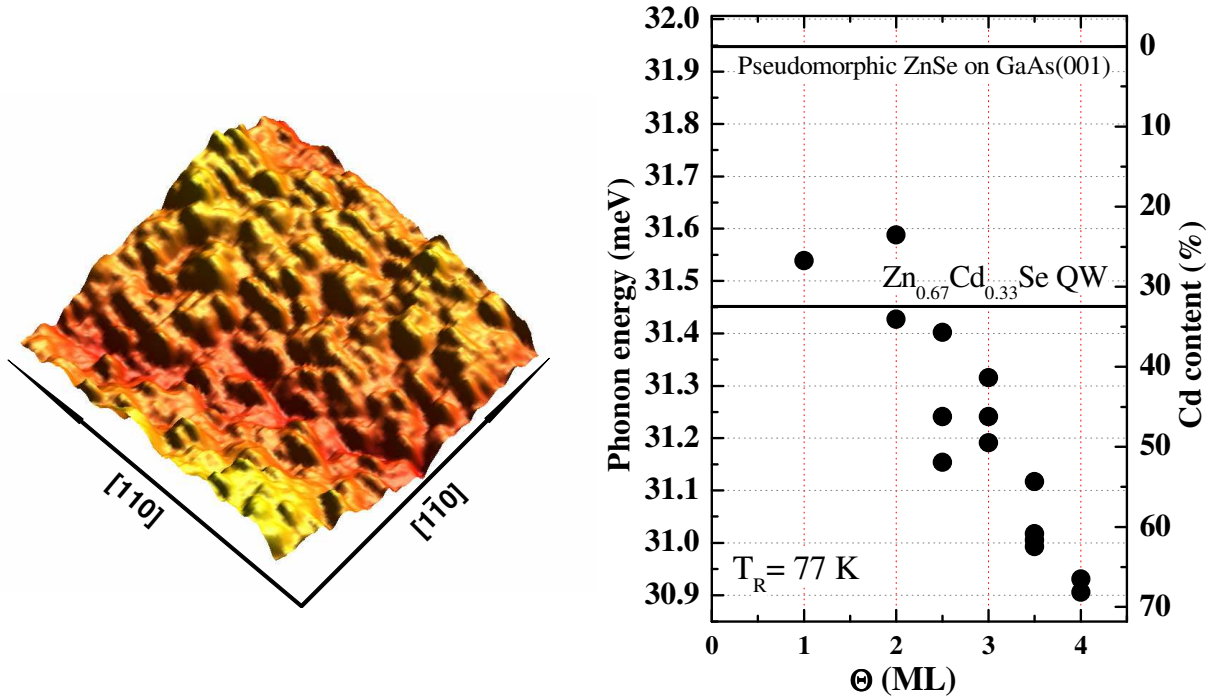


Fig. 4.5: Left panel: Atomic force microscope (AFM) picture (400×400 nm 2) of an uncapped one monolayer CdSe/ZnSe self-assembled QD structure. The QDs clearly elongate along the crystalline [110] direction. Right panel: Phonon energy vs. CdSe ML coverage measured by resonant Raman scattering. For reference, the phonon energies of pseudomorphic ZnSe and a Zn $_{0.33}$ Cd $_{0.67}$ Se Quantum Well on GaAs are included.

On balance, no well-separated, Stranski-Krastanow-like morphological QDs are formed by this method. Cross sectional High Resolution Transmission Electron Microscopy (HRTEM) on capped samples finally yields that instead a ZnCdSe ternary alloy layer with Cd-rich inclusions, which act as confinement centers, is formed. A characteristic HRTEM image of a two ML CdSe coverage sample is displayed in Fig. 4.6. A quantitative analysis of the CdSe content of the Cd-rich inclusions from the HRTEM picture is unfortunately not reliably possible due to the ambiguity of the actual strain conditions, which moreover may be severely altered by the thinning procedure necessary for HRTEM.

An upper boundary of the average Cd-content of the resulting potential traps as function of the Cd coverage was therefore determined by resonant Raman scattering

on as-grown samples and is also displayed in Fig. 4.5. The respective LO(Γ)-phonon energies are affected by both chemical composition and strain. Under the assumption of pseudomorphically (that is hydrostatically) strained nanostructures a maximum Cd content can be estimated. This assumption is justified for one by the absence of a 2D to 3D transition in the RHEED pattern, suggesting that no relaxation occurs. Further, reduced strain would give rise to a blue shift of the phonon energies, in contrast to the red-shift induced by increased Cd-content, rendering the determination of an upper boundary even more valid. The absolute Cd-content is obviously varying from QD to QD, as are their absolute dimensions, but the average Cd content for a given QD sample is almost constant over the ensemble, suggesting that difference in the QD ground state energies arises from size fluctuations of the Cd-rich inclusions.

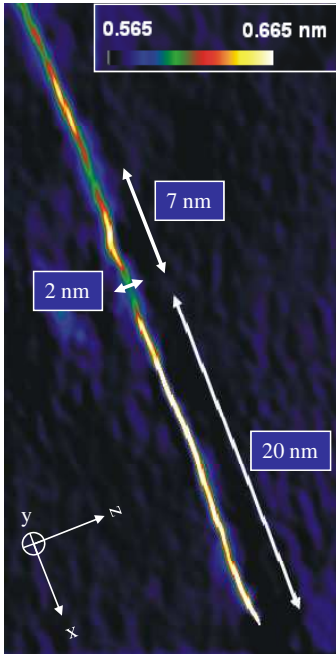


Fig. 4.6: Cross sectional high resolution transmission microscope (HRTEM) image of a two monolayer CdSe coverage QD sample. The color coding maps the variation of the lattice constant along z -direction as indicated in the figure, which coincides with the growth direction. The picture was recorded with a JOEL 4000EX microscope with the electron beam operated at 400 keV. The analysis of the lattice-parameter variation was performed by the geometrical phase method [Hyt98].

In-depth analysis upon variation of the growth parameters finally yields that the structures are formed in multi-layer growth mode, that closely resembles the surface roughness of the buffer layer [Mah07b]. The resulting QDs that form after capping with ZnSe, arise from the alloy fluctuations in the embedded ZnCdSe ternary alloy layer and are essentially Cd-rich inclusions in an inhomogeneous Zn-rich ZnCdSe matrix.

4.3.2 Low temperature epitaxy and in-situ annealing

The growth sequence of this approach is equivalent to conventional MBE up to the actual QD growth. After the deposition of the pseudomorphic ZnSe layer the temperature is ramped down under Se flux to $T_G = 230^\circ \text{C}$. Next, a uniform CdSe layer is grown at T_G . Subsequently the temperature is raised to $T_A = 280 - 310^\circ \text{C}$, at which the sample is annealed for 15 to 20 minutes. Finally the sample is capped with 30-50 nm of ZnSe at

T_A . Again, uncapped samples were grown for topological studies.

This approach is similar to the growth method demonstrated by Rabe *et al.* [Rab98]. During the annealing step a clear streaky to spotty RHEED transition is observed, which suggests formation of 3D surface features. AFM data on uncapped reference samples confirm the formation of well separated 3D islands (see Fig. 4.7).

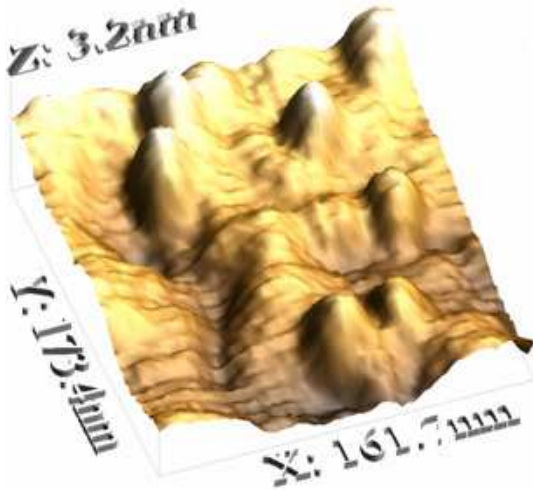


Fig. 4.7: AFM image of uncapped reference sample of in-situ annealed QDs with a CdSe coverage of three monolayers. The Y-axis is set parallel to [110] crystal axis, along which the 3D islands are slightly elongated.

The islands are about 2 nm high and have a diameter of about 20 nm. They are further slightly elongated along the [110] crystal axis and in marked contrast to conventional MBE have a low areal density of $2 - 5 \times 10^{10} \text{ cm}^{-2}$. From these numbers it is straightforward to calculate that these islands incorporate only ~ 0.3 MLs of CdSe, which suggests that one obtains pure CdSe islands on top of a quasi-2D CdSe layer.

The picture clearly changes upon capping the samples during which the RHEED pattern switches back from spotty to streaky. This is consistent with HRTEM studies on the capped samples, which reveal that the resulting QDs are Cd-rich inclusions inside of a ternary alloy ZnCdSe QW, very much like the QDs received from conventional MBE. An exemplary HRTEM image of a 3.8 ML CdSe coverage sample is shown in Fig. 4.8. This is direct evidence that the 3D features observed for uncapped samples by AFM collapse during the capping procedure. In light of previous studies on the influence of the cap on the formation of QDs it is highly likely that this modification arises from segregation of Cd and subsequent Zn-alloying of the previously present surface islands [Per00, Pas01, Kru07]. As a consequence the resulting QDs can be expected to be compositionally similar to the corresponding QD samples grown by conventional MBE. This is further corroborated by resonant Raman spectroscopy, which also yields average Cd contents for the resulting ZnCdSe layer that agree well with the respective conventional MBE grown samples [Mah07a].

Finally, X-ray diffractograms show that no Cd desorption occurs either during annealing or capping up to a coverage of 3.5 MLs of Cd, as the targeted Cd content is clearly achieved (not shown - see [Mah07a]). Above 3.5 MLs, the finite thickness fringes observed

in the X-ray diffractograms start smearing out considerably, which is attributed to the onset of the formation of stacking faults.

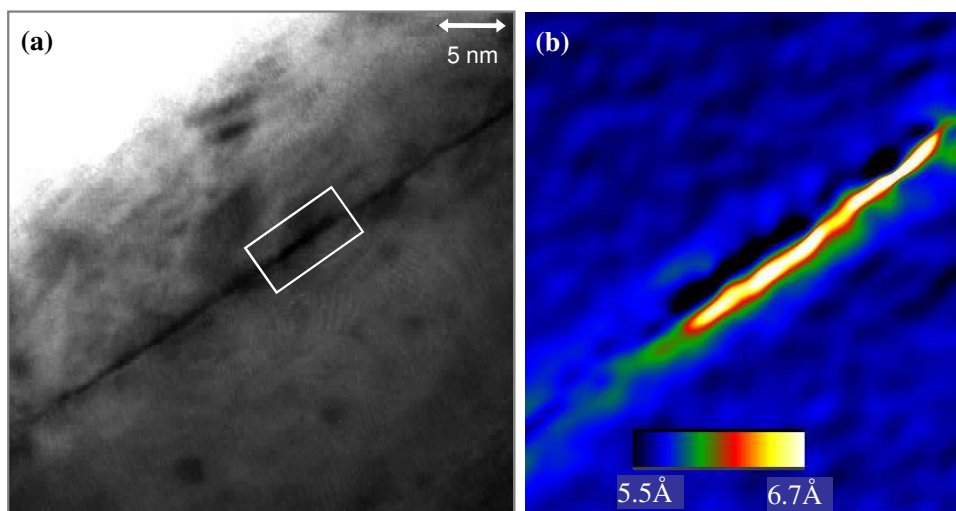


Fig. 4.8: (a) Cross sectional high resolution transmission microscope (HRTEM) image (bright field) of a 3.8 ML CdSe coverage QD sample grown by the in-situ annealing method. (b) Color coded map of the variation of the lattice constant along growth-direction across the QD layer depicted from the area marked by the white box in (a). The image was recorded under the same conditions as the picture displayed in Fig. 4.6.

Summarizing, structural and topological studies suggest the formation of well separated 3D features during the in-situ annealing step, which are stable against intermixing and Ostwald ripening. While strain certainly is a key parameter in the QD formation, this growth process is definitely not Stranksi-Krastanow like but is best described by a thermally activated surface reorganization mechanism. Upon capping the QDs appear to become, however, comparable to the QDs formed by conventional MBE, except for their areal density. The latter is by at least an order of magnitude lower than in the case of conventional MBE and is further tunable by the annealing time t_A , decreasing the areal coverage with increasing t_A [Mah07c]. As a result of the increased inter-dot spacing carrier escape due to inter-QD tunneling should be noticeably reduced in the QDs grown by this method with respect to their conventional MBE counterparts. The inhomogeneity of the Cd content over the ensemble after capping is a strong indication that the resulting QDs vary heavily in their chemical composition, which is substantiated by the PL data in the next section.

4.4 Conventional MBE versus low temperature epitaxy QD luminescence

A detailed overview of the QD ensemble photoluminescence (PL) data obtained for CdSe/ZnSe QDs grown by the methods described in Sections 4.3.1 and 4.3.2 is given in Fig. 4.9 below:

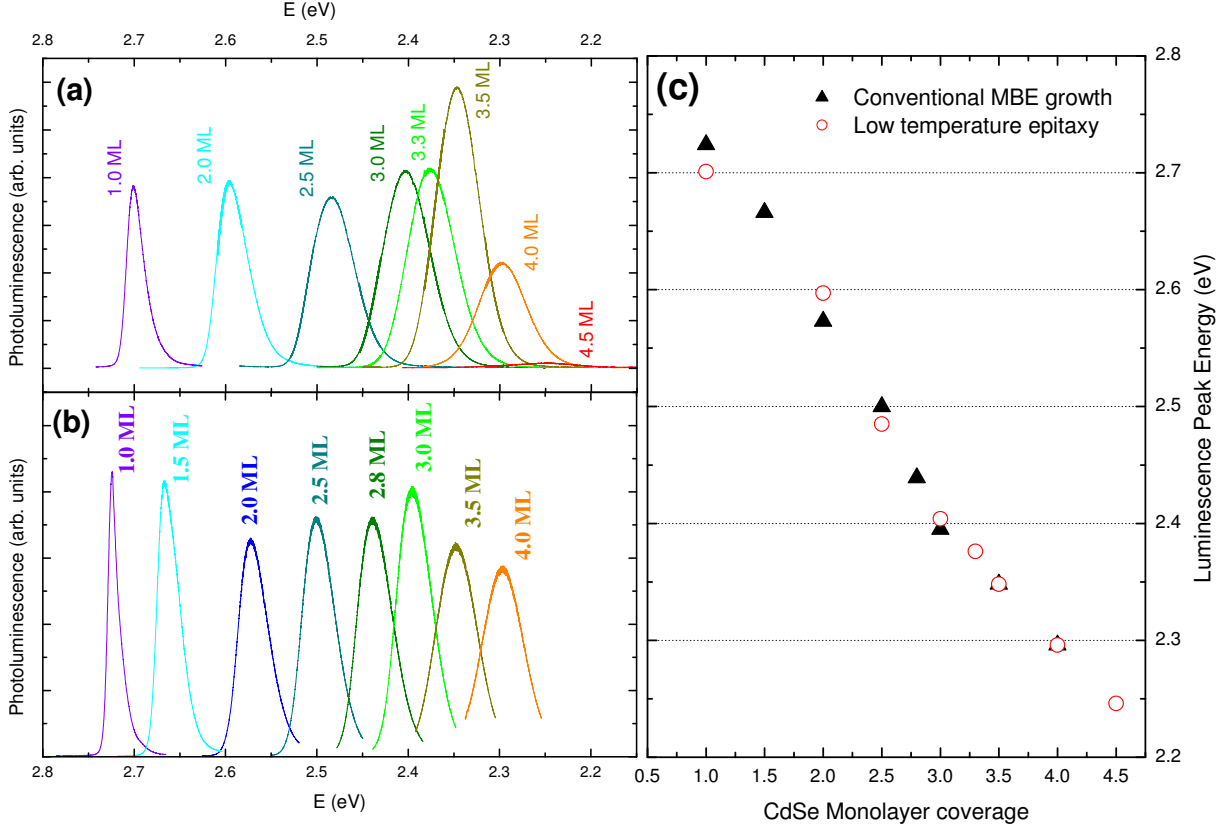


Fig. 4.9: Overview of the QD ensemble photoluminescence data at $T = 2$ K: (a) Photoluminescence spectra for QDs grown by low-temperature epitaxy and subsequent in-situ annealing depending on the nominal CdSe depositon during growth in monolayers (ML). (b) Same as (a) for conventional MBE grown QDs. (c) Ensemble luminescence peak energy position vs nominal CdSe coverage for both methods. For CdSe contents above 3 MLs the peak energies essentially coincide.

From panel (c) it is directly obtained that the evolution of the ensemble PL peak energetic position as function of CdSe deposition is strictly monotonic and no discontinuities are observed. This is consistent with the absence of a clear streaky RHEED pattern after ZnSe capping for both methods and further substantiates that the QD formation is not Stranski-Krastanow like. Moreover, the peak energetic positions resulting from the two growth variants are vastly similar, for CdSe contents above three monolayers they even appear to be identical. This strongly suggests that the final QD energetic structure is mostly determined by the capping procedure, which is in accordance with findings by

other groups (see Section 4.2).

A marked difference, however, is observed in the evolution of PL intensities for samples with CdSe coverages above 3.5 MLs when comparing both methods. While the overall optical gain from the conventional MBE grown QDs is largely constant, the intensity of in-situ annealed QDs noticeably decreases and is completely quenched for CdSe coverages above 4.5 MLs. This behavior is ascribed to the onset of plastic relaxation of the QD layer that is accompanied by the formation of stacking faults, which act as nonradiative decay channels for excitons. This conclusion is corroborated by the findings of X-ray studies, which show increasingly smeared out fringes above 3.5 MLs of CdSe (see section 4.3.2).

For a rigorous proof of the zero dimensional character of the PL emission, samples with small sized mesa structures have been lithographically prepared. By reducing the number of QDs in the laser spot, the radiative recombination of individual QD excitons becomes resolvable. Typical data for such μ -PL studies on 3 ML QDs samples prepared by both growth methods are presented in Fig. 4.10.²

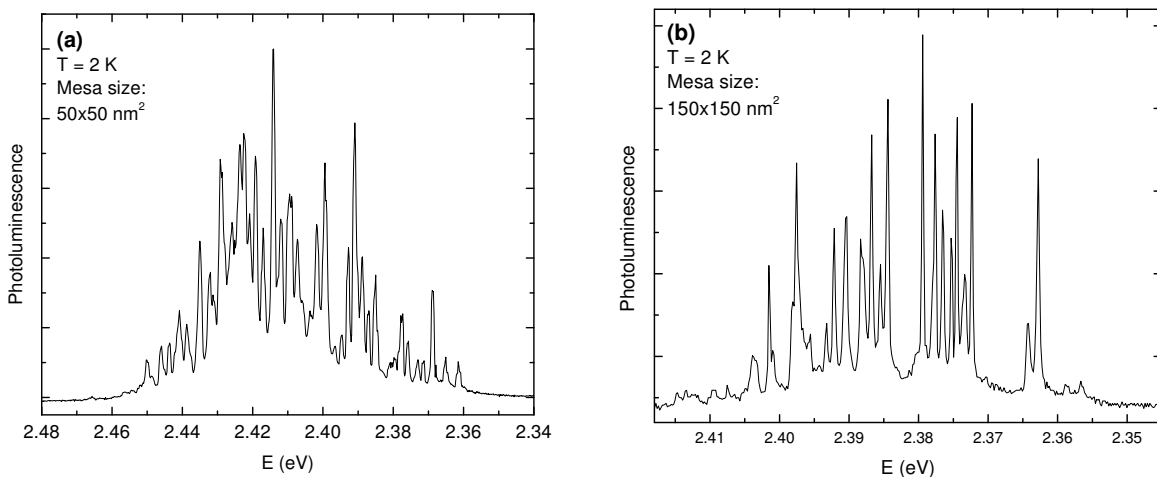


Fig. 4.10: Comparative μ -PL study of lithographically prepared mesa structures on QD samples with a CdSe coverage of three monolayers. For both methods it is clearly established that the inhomogeneously broadened ensemble luminescence deconvolutes into narrow emission lines, which are characteristic for PL from individual QDs. **(a)** For conventional MBE grown samples the QD areal coverage is extremely high, rendering the isolation of single QD emission impossible. **(b)** The number of lines observed in QD samples prepared by low temperature epitaxy is markedly reduced. Also note, while the ensemble PL for both methods energetically coincides, the PL of individual lines at low excitation conditions appears to be redshifted with respect to **(a)**.

From these data it is further possible to estimate the QD areal coverage by counting the number of lines observed. This value has to be regarded as an upper limit, as it does not account for the formation of excitonic complexes, which are simultaneously observable

²These data have been recorded by E. Margapoti, Lehrstuhl für Technische Physik, Universität Würzburg.

for a single QD in the time integrated spectra. It is nevertheless a valuable link to the topographical investigations. For the conventional MBE grown QDs it is not possible to even completely resolve individual lines for the smallest available mesa of $50 \times 50 \text{ nm}^2$. A rough estimate yields numbers in the high 10^{12} cm^{-2} range, which agrees well with results from AFM. It is therefore concluded, that the observed elongated ripples indeed act as precursors for the final QDs. Quite opposite, in the case of QDs prepared by low temperature epitaxy individual lines are already clearly resolved for mesa sizes of $200 \times 200 \text{ nm}^2$. Consequently the QD areal density is a lot lower and ranges from $1\text{-}5 \cdot 10^{10} \text{ cm}^{-2}$. This and the fact that the individual lines observed at low excitation density appear on the low energy flank of the ensemble luminescence, which implies that they are either CdSe-rich or large in size, are strong indications that the final QDs result from the CdSe islands, which form during the annealing step. At the same time these data appear to contradict the above findings by the ensemble luminescence, which calls for a more rigorous investigation of the QD PL data.

Bearing in mind the Raman data presented in Section 4.3.1 it is clear that with increasing Cd deposition the QDs emerging from conventional MBE growth increase in average Cd content. A simple estimate directly yields that the increase of the Cd content alone as deduced in Fig 4.5 can not be held responsible for the redshift observed for PL ground state energy in Fig. 4.9. In accordance with the fact that the overall Cd-content is not varying much across the ensemble for conventional MBE grown QDs, it is therefore deduced that the QDs also increase in size. Comparing the physical sizes of the surface features on the reference samples found by the topological investigations as well as the in-plane dimension of the Cd-rich zones found by HRTEM with the bulk exciton Bohr radius of CdSe of $a_B \sim 5.6 \text{ nm}$ hence determines the sample choice: Since there are no detailed topological informations available on the shape and size of the QDs after cap, it is clear from the above that excitons which are strongly confined in all three spatial directions are most likely to be found in the samples with the lowest available nominal Cd surface coverage. It is therefore, that for the remainder of this work we limit ourselves to investigations of samples with a nominal CdSe coverage of one monolayer.

Chapter 5

Electronic Properties of shallow CdSe/ZnSe Quantum Dots

This chapter deals with the experimental characterization of the electronic and resulting optical properties of strongly confining CdSe/ZnSe QDs. It is found by extensive experimental test that these are robustly reproducible from sample to sample and are further almost identical for both growth methods described above. We thus choose to show a full set of data on one representative sample grown by conventional MBE, which will be used on all forthcoming experiments presented in this Thesis. On this basis we discuss the peculiarities, be it that they are only minor, of the QD composition resulting from the two growth methods.

For a comprehensive characterization power and temperature dependent photoluminescence (PL) as well as photoluminescence excitation (PLE) spectroscopy are employed under continuous wave (cw) excitation and supplemented by time-resolved data. These methods enable a thorough establishment of the QD internal energetic structure and the composition of excitonic complexes over QD ensemble, the knowledge of which forms the backbone of the discussion on the optical anisotropy in chapter 6.

The data moreover provide access to the complex interaction of excitons confined to QDs with the lattice of their host material. The investigation of the unusual exciton-phonon interaction witnessed in our material system forms the second part of this chapter. When tuning the optical excitation into resonance with excited electronic exciton states within the QDs, we find the appearance of a broad phonon-replica with a remarkable finestructure that persists up to the fourth order and cannot be explained in terms of alloying or interface phonons. Our interpretation invokes the truly zerodimensional properties of the confined excitons, which totally relaxes the k -conservation condition and therefore enables interaction with phonons over the complete Brillouin zone.

5.1 Electronic structure and composition

The excitation-density dependent photoluminescence spectra of a conventional MBE grown one monolayer $\text{Zn}_{1-x}\text{Cd}_x\text{Se}$ fluctuations QD sample are displayed in Fig. 5.1 below.

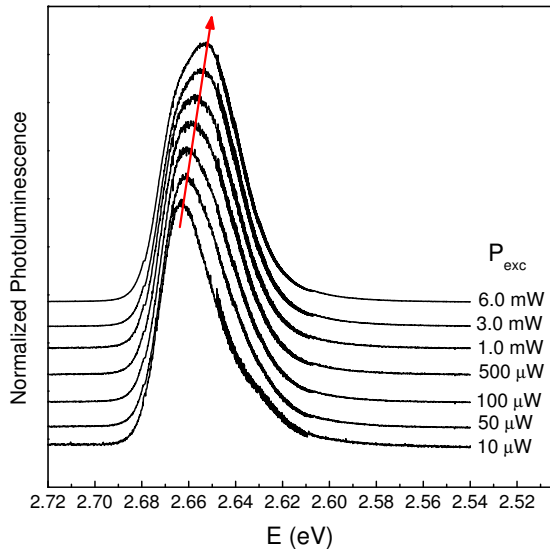


Fig. 5.1: Evolution of the photoluminescence (PL) band of an one monolayer CdSe fluctuation QD ensemble as function of excitation power P_{exc} . The PL was recorded at $T=1.6$ K with $E_{exc}=3.5$ eV. The center of gravity of the PL is clearly redshifted for increasing P_{exc} as indicated by the red arrow.

The PL band has a full width at half maximum of ~ 30 meV, is markedly asymmetric and clearly resembles the inhomogeneously broadened spectrum that arises from probing approximately 10^8 QDs of different shape, size and composition simultaneously. Since one would not expect a gaussian distribution of exciton ground state energies even for a perfect gaussian distribution of QD sizes at constant alloy composition (see Section 3.2) for very small QDs, the asymmetry is not surprising. It is further clear from the redshift of the spectral maximum of PL band with increasing excitation density P_{exc} that a significant contribution in the PL must arise from trions and/or biexcitons. Previous work established that these excitonic complexes are expected to be shifted by 15-20 meV and 20-25 meV, respectively, to lower energies with respect to the exciton ground state energy in the CdSe/ZnSe material system, depending on the exact QD parameters [Low99, Pat03]. They are further known to increase their spectral weight superlinearly with increasing P_{exc} , which stands in perfect agreement with the observation. One can finally expect phonon replicas of all of the above excitonic complexes to be present in the low energy tail of the PL band, which is best seen from the PL band recorded for low P_{exc} .

In order to identify the various contributions more rigorously and to obtain information on the internal energetic structure of the QDs photoluminescence excitation spectroscopy (PLE) was performed. To avoid artifacts from phonon replicas of the exciting laser in the PL band, we recorded the integrated intensity of the PL band as function of excitation. The result is displayed in Fig. 5.2.

For excitation energies E_{exc} below the ZnSe band edge the overall intensity of the QD PL band decreases by about one order of magnitude, which signifies efficient capture of photocarriers excited in the ZnSe matrix by the QDs. It is thus evidence of high quality

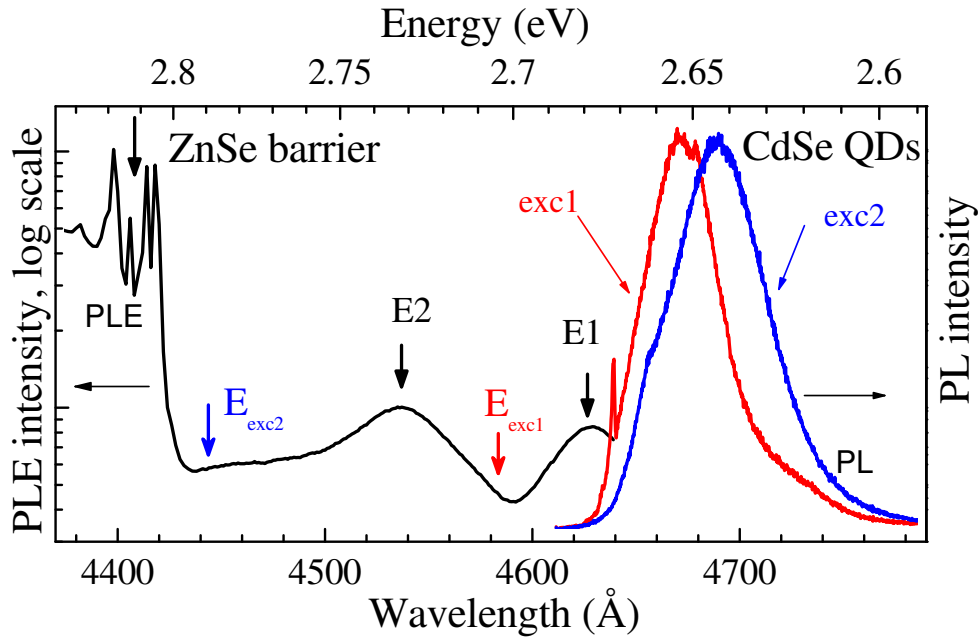


Fig. 5.2: Photoluminescence excitation spectrum of a one monolayer CdSe coverage fluctuation QD sample. Plotted is the integrated intensity of the QD ensemble luminescence band versus the excitation energy. We find two excited states labeled E1 and E2, respectively, the latter of which is identified as the mobility edge for carriers excited in the QD layer. For reference two ensemble PL bands are shown, which are excited above (blue) and below (red) E2, clearly demonstrating a marked blue-shift for excitation below E2. The sharp feature in the respective PL-band is ascribed to the ZnSe-LO(Γ) phonon replica of the exciting laser.

interfaces between the QD layer and the adjacent ZnSe layers and proves a low density of defects, which would act as killer centers by opening non-radiative decay channels. The energetic position and the overall shape of the PL band remains, however, unchanged.

We further identify the presence of two excited states ~ 30 meV and ~ 90 meV above the exciton ground state energy, labeled E1 and E2. For $E_{exc} < E2$ the PL band is blueshifted by about 15 meV with its FWHM reduced by 10 meV to 20 meV. For these excitation conditions the shape and the energetic position of the PL maximum are also independent of P_{exc} . We therefore conclude that for excitation energies below E2 only excitons are formed. In this picture we can identify the feature at ~ 2.63 eV as phonon replica (ZnSe LO(Γ)) of the exciton luminescence. The E2 states are then identified as the mobility edge [Rez02]. For $E_{exc} > E2$ carriers excited in the QD layer are free to move and hence are able to form charged exciton and multi-exciton complexes, while for $E_{exc} < E2$ the excitons are directly pumped into the QDs. This is, however, not evidence for a complete absence of charged excitons.

Even though the material is nominally undoped, II-VI semiconductors usually exhibit a defect-related residual n-type background, which arises from the low temperature growth conditions (see chapter 4). From previous studies on II-VI quantum well (QW) structures

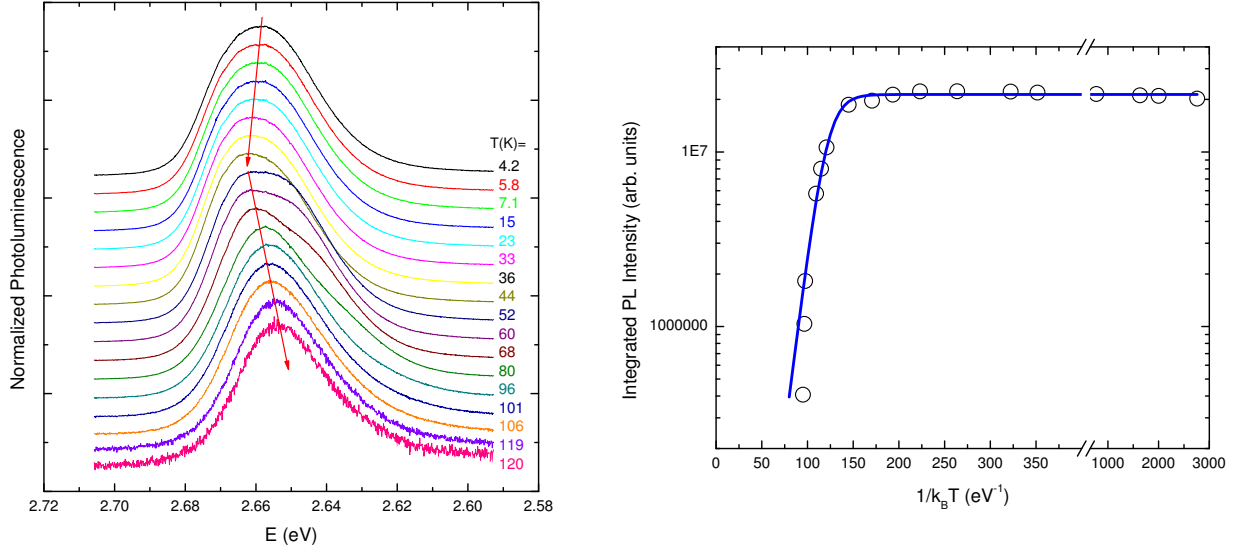


Fig. 5.3: Temperature dependence of the QD ensemble luminescence: (a) Normalized PL spectra excited above the ZnSe barrier ($E_{exc}=3.5$ eV, $P_{exc}=300$ μ W) for increasing temperature. The red arrows are guide to eye and follow the PL band peak. (b) Arrhenius plot of the integrated intensity of the lefthand PL spectra. Blue line is a fit to the data according to the thermal activation model.

it is known that the sheet electron density in such a nominally undoped structure is typically a few 10^9 cm^{-2} [Ast02]. Since essentially we are studying a rough QW, this numbers should be in the same ballpark for the QD system under investigation. Upon comparing this figure to QD areal density of several 10^{12} cm^{-2} , either extracted from the AFM studies or μ -PL, it is clear that only a small fraction of the QDs will host residual electrons. However, these electrons can form trions even if the excitons are resonantly excited into the QDs. They should predominantly appear on the low energy side of the PL band due to the reduced ground state energies of trions with respect to excitons. Likewise, their formation dynamics must be different from that of trions formed by photoexcitation.

To further elucidate the nature of the E2 states temperature dependent PL has been recorded for excitation above the ZnSe barrier. The data are displayed in Fig. 5.3. We find that up to 50 K the PL intensity is constant and the peak intensity is monotonically blueshifted by about 10 meV at 50 K compared to 4.2 K. Between 50 K and 60 K the PL intensity is marginally increased followed by a dramatic decrease in intensity above 60 K. Moreover, for temperatures above 60 K the PL peak energy is monotonically redshifted. No QD PL is observable for $T > 122$ K.

To model the evolution of the PL intensity with increasing temperature we invoke a simple rate equation model, that takes into account radiative and thermally activated nonradiative decay [Bac91]:

$$\frac{\partial c}{\partial t} = -\frac{c}{\tau_J} - \frac{ce^{-E_A/k_B T}}{\tau_{nr}} + G \quad (5.1)$$

Here c is the number of excitons, τ_J the average radiative lifetime of excitons confined to QDs and τ_{nr} the effective scattering time of confined excitons into continuum states. The effectiveness of this channel is heavily dependent on the thermal distribution of excitons $ce^{-E_A/k_B T}$, where E_A is the characteristic activation energy that is defined by the total confinement energy in the case of QDs. The generation rate G depends on the laser excitation conditions. For the steady-state conditions $\frac{\partial c}{\partial t} = 0$ and $G = \frac{c_0}{\tau_J}$ under which the experiments are performed we obtain

$$c(T) = \frac{c_0}{1 + \frac{\tau_J}{\tau_{nr}} e^{-E_A/k_B T}} \quad . \quad (5.2)$$

To first approximation we take $\frac{\tau_J}{\tau_{nr}}$ to be independent of temperature, which is certainly oversimplified but reasonable with respect to the strong temperature dependence of $e^{-E_A/k_B T}$. The integrated PL intensity as function of temperature is then fit by Eq. (5.2). Despite the rather rough approximations made, the fit agrees well with the data, except for the datapoint recorded at $T=120$ K. This is readily understood, since at elevated temperatures the scattering rates are certainly enhanced. For a typical τ_J of several hundreds of picoseconds [Pat03], the fit yields an average scattering time τ_{nr} on the order of tens of femtoseconds. This is a reasonable result when compared to scattering times obtained by time resolved experiments, which are clearly in the sub-picosecond regime [Kli99]. The impact of enhancing the scattering rates on the fit would be an increasing slope with increasing temperature, yet given our data, for such a fitting procedure our system is underdefined. As we are mainly interested in E_A , which marks the onset of the saturation and is independent of τ_J and τ_{nr} , this fact can safely be neglected. As a key result, the fit then yields a characteristic activation energy $E_A = (96 \pm 8)$ meV. This value is in superb agreement with the relative energetic position of the E2 states obtained from PLE and enables a comprehensive understanding of the energetic structure of the QD layer.

It is clear that the total confinement energy is limited by the existence of quasi-2D states represented by the E2 states. For excitation in or above those the photocarriers are mobile and can relax over the parts of the ensemble, thereby mainly forming energetically more favourable charged and multi-exciton ground states. It is further clear that these states cannot be understood in terms of a wetting layer, as no such layer is observed in the HRTEM studies on the capped samples. We therefore interpret the E2 states as energetic signature of 2D platelets of finite size, which connect sub-ensembles of individual dots in the QD layer. This interpretation agrees well with spatially resolved micro-PLE studies on comparable samples, in which it was found that different dots can share common excited states [Ngu07].

The interpretation of the evolution of the energetic position of the peak PL intensity is not straightforward. The slight increase of the PL intensity between 50 and 60 K can be ascribed to thermal repopulation of the dark exciton into the bright exciton states. Previous studies on the temperature dependence of the radiative decay times of excitons

confined to $\text{Zn}_{1-x}\text{Cd}_x\text{Se}$ alloy fluctuation QDs clearly established a contribution of the dark exciton repopulation on the decay times in this temperature regime [Pat03], which is naturally accompanied by an increase in the observed intensity and stands in good agreement with our findings. The abrupt drop in the PL intensity above 60 K then marks the onset of the thermal escape of excitons from the QDs. What is puzzling, however, is the magnitude of energetic shifts, which is clearly smaller than the thermally induced reduction of the fundamental band gap of both CdSe and ZnSe. Up to 50 K it is not even of the correct sign. It is known from comparable studies that the peak energetic position of the ensemble PL does not necessarily follow the band gap evolution as a result of thermal repopulation of excitons within the ensemble. For example, it has been found in both CdTe/ZnTe [Kar99] and InAs/GaInAs [Pop04] QDs, that the peak intensity redshift clearly exceeds the band gap induced decrease in the exciton ground state energy. These findings are well explained from the size distribution of QDs over the ensemble. As the confinement potentials increase with increasing dot size, excitons confined to small QDs will dissociate first and can then be captured by larger QDs.

However, we observe the opposite as in our case the PL peak intensity is consistently blue-shifted with respect to the band gap evolution, which to the best of our knowledge has not been previously reported. We attribute this behavior to a massive reorganization of the relative intensities of different exciton complexes with increasing temperature. As the temperature rises the formation of uncharged excitons is obviously favored over formation of trions and/or biexcitons. On balance, while the exciton ground state energy is reduced, the net energetic shift of the PL band is blueshifted initially and above 60 K redshifted at a much lower rate than expected from the temperature evolution of the fundamental band gap.

To shed additional light on the formation dynamics of the PL ensemble ground states, time-resolved photoluminescence has been recorded.¹ These data are displayed in Fig. 5.4. The evolution of the ensemble luminescence is most clearly seen from the normalized spectra. The PL initially rises, peaking at 2.655 eV. The shape and the energetic position of this PL band almost perfectly coincides with the PL band recorded under steady-state conditions for $E_{exc} < E_2$. We therefore conclude that in this regime exclusively excitons are formed and consequently label these states X. Between 550 and 700 ps the complete PL band experiences a massive redshift, with the energetic peak shifted by as much as 15 meV. This transition clearly marks the formation of charged and multiexciton complexes and is subsequently labelled T. The energetic position of this band then persists over the complete radiative lifetime of the PL band and further marks the position of cw-excited PL band for $E_{exc} > E_2$. From the data we can further directly extract the radiative decay times, which are 180 ps and 280 ps for the X and T, respectively. These number further substantiate our interpretation, since the X states have additional decay channel through the formation of exciton complexes, whereas the T exclusively decay radiatively.

¹These data have been taken by the group of M. Bayer, Lehrstuhl Experimentelle Physik IIa, Universität Dortmund

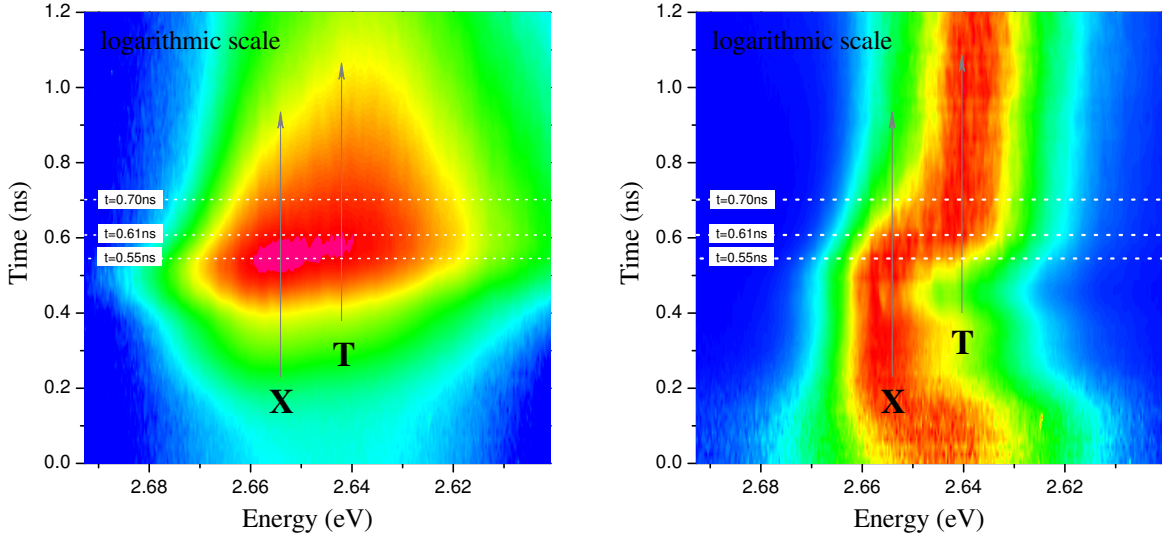


Fig. 5.4: Temporal evolution of the photoluminescence band of a one monolayer CdSe coverage conventional MBE grown QD ensemble at $T=1.6$ K. The PL was excited with a frequency doubled Ti:Sapphire laser at $E_{exc}=3.1$ eV with a pulse width of 150 fs and recorded by a streak-camera with overall time resolution of 70 ps. In the left panel the time evolution of the PL intensity can be depicted. The energetic peak position is redshifted by about 15 meV at ~ 610 ps. This is seen even more clearly from the normalized data displayed in the right panel.

Summarizing, the time resolved data corroborate the assignment of excited states and internal structure of the ensemble PL band. They moreover show, that the ensemble PL band is not simply a direct display of the size distribution of QDs, but instead is the result of a complex charging sequence that is in addition heavily temperature dependent.

Summary

The above results are totally consistent with the morphological investigations (AFM and HRTEM) and studies by resonant Raman spectroscopy presented in chapter 4 for QDs grown with a nominal CdSe coverage of one monolayer. The QDs are effectively formed by Cd-rich inclusions in a Zn-rich ternary ZnCdSe alloy and confine at least one excitonic level. The nature of the enhanced PL intensity arising from excitation ~ 30 meV above their energetic ground state is not conclusively answered by the measurements presented up to this point, yet the fact that the PL temperature evolution is well described without assuming excited states may be taken as hint that there are none and the E1 states arise from distinct features of the energy relaxation. The PL data yield an activation energy E_A of ~ 90 meV, which is clearly less than the energetic distance to the ZnSe barrier. This result in combination with the dynamic and the PLE data states that the individual QDs are embedded in quasi-2D ZnCdSe platelets with a slightly reduced Cd-content with respect to the QDs. While not forming a uniform layer in the sense of a wetting layer, these platelets enable photocarriers to move from dot to dot and

therefore mark the energetic position of the mobility edge. On balance, the resultant QDs robustly confine excitons to slightly above liquid nitrogen temperature ($T=77$ K). This temperature is ultimately defined by both the activation energy E_A and the radiative lifetime to nonradiative scattering rate ratio.

These results are robustly reproducible on a wide range of examined samples grown by both methods described in section 4.3. This means that the only recognizable difference between the growth variants is the resulting areal density of the QDs, as seen from the μ -PL in Fig. 4.10. It therefore has to be concluded that the 3D features observed under AFM are the seeds of the resulting QDs in both methods, yet their size and chemical composition appear to be totally defined by the CdSe content offered during growth. Most important, the actual QD formation is obviously entirely governed by the capping procedure.

5.2 Exciton-phonon interaction

This section details the peculiarities of the interaction of strongly confined excitons with phonons in narrow CdSe/ZnSe QDs. The relaxation of energy in semiconductor QDs is now a longstanding problem that puts the basic understanding of the carrier-phonon interaction in a fully confined system to the test. Due to the discrete nature of the energy spectrum of QDs, the interaction with phonons was a priori expected to be only efficient if the interlevel energetic spacing was either matching a small window around the LO-phonon energy (or integral multiples thereof) or smaller than a few meV in favor of LA-phonon scattering. With the spacing of the low lying levels, especially in strongly confining QDs, exceeding the typical phonon energies, the transitions between these quantized levels were thought to only occur via multiphonon processes, which is why the energy relaxation in QDs was early on predicted to be slow and inefficient [Boc90].

This so-called *phonon bottleneck* has ever since been controversially discussed in the field, which is in great part caused by seemingly contradictory experimental results. While there is indeed some experimental work that supports the existence of a phonon bottleneck (e. g. [Muk96, Hei01, Xu02]), the vast majority of the reported experiments (see e. g. [Wan94, Ohn96, Boc97, Kli99, Co07]) demonstrate fast and efficient carrier relaxation inside QDs, which is inconsistent with the above claim.

Several non-phonon mechanisms have been proposed which would be able to explain energy relaxation on ultrashort timescales. U. Bockelmann and T. Egerle suggested a model based on Auger processes of the QD confined carriers with an electron-hole plasma outside the QD, the latter of which exhibits an efficient energy exchange with the phonon bath [Boc92b]. Such a model could only be invoked, however, in the case of high excitation densities and, moreover, cannot explain fast relaxation in colloidal QDs at all [Kli99].

The experimental observation of correlations between the strength of the electron-hole coupling and the rate of electron relaxation on the other hand provided strong evidence that the energy relaxation in small QDs is dominated by an Auger-type energy transfer from the electrons to holes [Kli00]. This mechanism was originally proposed by Efros *et al.* and assumes energy transfer from the electron to the hole within excitons via Coulomb interaction and a subsequent rapid hole relaxation through its dense spectrum of states [Efr95] (recall that the hole level spacings are typically one order of magnitude smaller than those of the electrons as a result of the larger effective mass and valence band degeneracy). While this model is capable of explaining fast energy transfer from electrons to holes, the reverse process, i. e. energy transfer from holes to electrons, would not be efficient, because of the small inter-level separations of holes, which means that this process technically is *unidirectional*. However, recent experiments on colloidal QDs clearly demonstrate hole relaxation on the fs-scale [Coo07], which the authors ascribe to a vibrational coupling of the particle stabilizing surface ligands.

Beyond that, there is theoretical work which suggests that the phonon-induced relaxation in QDs may not at all be as inefficient as initially thought. Arakawa and co-workers

pointed out that on taking into account anharmonic decay of LO phonons into bulk acoustic phonons, which is a well understood effect [Val94], the energetic window around which the LO-phonon relaxation remains effective broadens up to several tens of meV [Li99]. Seebeck *et al.* demonstrated that other than widely applied time-dependent perturbation theory, a quantum kinetic description of carrier-phonon interaction predicts ps-relaxation even in weak polar coupling material at least for elevated temperatures [See05]. Their result mainly arises from the polar coupling of the localized quantum dot states, which brings up another long running open question: Is it actually appropriate to think in terms of excitons interacting with phonons or do we have to find a description in which we take into account that the carrier phonon interaction renormalizes both the electronic and vibrational states, i. e. zerodimensional excitonic polarons?

Several theoretical works have stressed the importance of polaronic effects in semiconductor QDs [Ino97, Ver02, Jas03, Vas04], yet from the experimental side there is no clear cut answer to that question as of now. More recent work regarding intraband relaxation in InAs QDs is at least consistent with a polaronic description [Zib04], which if true was ever more so important in more polar materials like CdSe/ZnSe. For the case of extremely shallow QDs, arising from deposition of only one or even a fractional monolayer (e. g. [Kre01]), one can take these considerations even further and ask whether or not the electronic confinement arising from the QD size alone characterizes the QD or if indeed one needs to think of *bound polarons* [Wog03].

Summarizing, while it is now clear that phonons are not the sole energy relaxation channel in QDs, even with almost 20 years of research on QDs at hand, a thorough understanding of the exciton-phonon interaction in QDs is far from being reached. There is not even a general agreement as to what the appropriate theoretical tools are. The highly unusual exciton-phonon interaction witnessed in our material system will therefore first be described by pure experimental fact, which henceforth is discussed in the light of the above said.

5.2.1 Experimental results

The shape of the ensemble PL band is strongly dependent on the excitation conditions, as was already detailed in section 5.1. The full evolution of the PL band as the exciting laser is tuned close to PL band is displayed in Fig. 5.5. For reference, Fig. 5.5a shows the PL band for excitation above the ZnSe band edge. When the excitation is tuned below the E2 states (the mobility edge) and close to the energetic position of the E1 states (see Fig. 5.2), a sharp peak arises and the ensemble peak luminescence is blueshifted by $\Delta E=11$ meV accompanied by a narrowing of the PL band. It is well established that the sharp peak is a phonon replica [ZnSe LO(Γ)] of the laser line, quasi-resonantly exciting photocarriers into the QDs, which then relax into the energetic ground state of the QDs and thus give rise to the reformation of the PL band. The narrowing of PL band as well as the peak blueshift result from the reduced trion formation under these excitation

conditions.

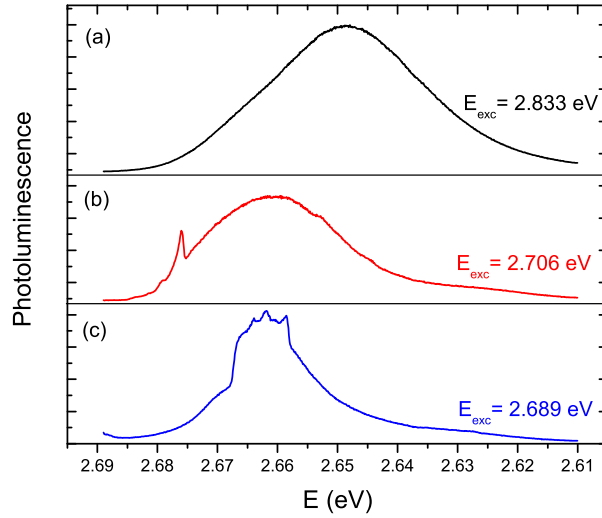


Fig. 5.5: Evolution of the PL signal as a function of excitation energy E_{exc} at $T=1.6$ K. (a) QD ensemble luminescence with excitation above the ZnSe barrier. (b) Appearance of the phonon replica with excitation below the ZnSe barrier. (c) Resonant excitation into the QD E1 excited states. The phonon replica no longer appears as a narrow peak, but rather as a broad band revealing fine structure.

The PL band exhibits a massive reconstruction as the excitation is tuned into resonance with the E1 excited states of the QDs. The full width at half maximum (FWHM) of the PL is reduced to 14 meV and the phonon replica no longer appears as a narrow line but instead manifests as a broad band that clearly yields fine structure. At least three peaks are resolved out of which only the lowest energetic one can be ascribed to the ZnSe LO(Γ) phonon.

For a more detailed description of the phonon replica fine structure, polarization-sensitive PLE was performed on the QDs. Keeping in mind the fact that the optical polarization is conserved during the fast phonon relaxation process [Sch03b], only the PL polarized parallel to the exciting polarization (in our case the linearly polarized component parallel to the [110] crystalline direction) should contain information on the phonon band. Therefore PLE was recorded with detection polarization parallel and perpendicular to the excitation polarization direction. To elucidate the dependence of phonon band fine structure on the detection energy, the PLE data taking procedure was set up the following way: For each excitation energy a CCD spectrum containing 1100 data points in the energy range from 2.61 to 2.69 eV was recorded for both polarization directions in the detection. Hence the difference of the normalized spectra was calculated in order to remove any background contribution. This data taking procedure was repeated for excitation wavelengths from 4430 to 4630 Å in steps of 0.25 Å (which corresponds to energy range from 2.798 to 2.678 eV). The procedure is visualized in the left panel of Figure 5.6. All data were taken at a temperature of $T = (1.6 \pm 0.1)$ K, the excitation power was stabilized at $P = (20.0 \pm 0.2)$ mW with a spot diameter of one mm.

It is then possible to obtain full information on the carrier-phonon interaction as function of excitation and detection energy by presenting the data in the form of a 3D spectral map as done in the right panel of Fig. 5.6. In such a graph one plots the excitation energy versus detection energy, with the backgroundcorrected PL intensity colour-coded

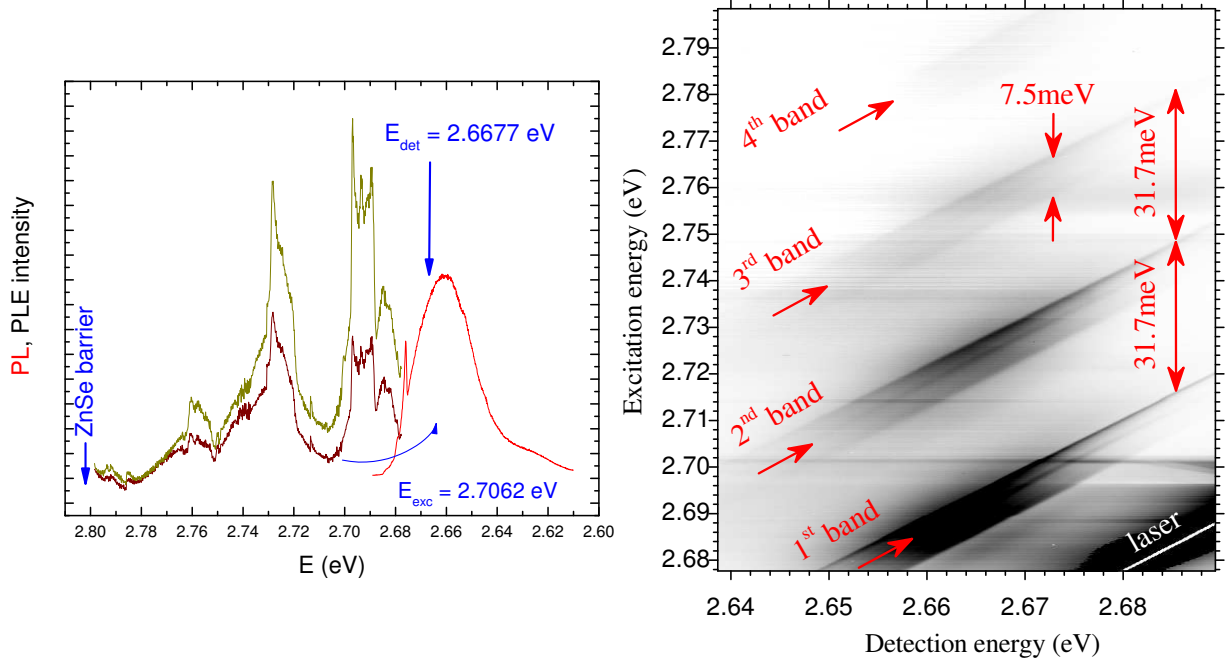


Fig. 5.6: **Left panel:** PL and PLE spectra at $T=1.6$ K. The PLE, here detected at $E_{det}=2.667$ eV, was background corrected by taking the difference in intensity of PL polarized parallel (yellow) and perpendicular to the excitation polarization (brown). Even without correction four phonon bands are visible from the raw data. **Right panel:** 3D spectral map of the background corrected PL intensity as function of the excitation energy. Plotted is the excitation energy versus detection energy, the PL intensity is colour-coded from white (no signal) to black (normalized signal 1). Four phonon bands are clearly resolved, which have a spectral width of 7.5 meV and exhibit an energetic spacing of 31.7 meV.

from white (no signal) to black (maximum signal). In this scheme horizontal slices through the map represent PL spectra for a given excitation energy, whereas vertical slices through the map depict classical PLE spectra for a given detection energy.

For improved visibility we identify major features of the spectral map on the basis of a PLE slice at a detection energy $E_{det} = 2.6677$ eV as displayed in Fig. 5.7. From the background corrected PLE four phonon bands are obtained, out of which the three lower energetic ones restore with high accuracy the fine structure that was previously observed in the PL spectra. The intensities of the phonon band are changing because of decreased signal-to-noise ratio as the energy rises, which is also the reason no fine structure is resolved in the fourth peak. This can easily be understood, as increased dephasing occurs as more phonons are involved in the relaxation process. Again, the outmost peak situated 31.7 meV above E_{det} can be ascribed to the LO(Γ)-ZnSe phonon. There are three main observations in the PLE data: First, the energetic width of 7.5 meV is conserved for all four phonon bands in the spectrum, as is their energetic spacing of 31.7 meV. Second, the energetic position of the fine structure peaks within the phonon band reproduces for all phonon bands. Finally, the intensities of the fine structure peaks relative to each

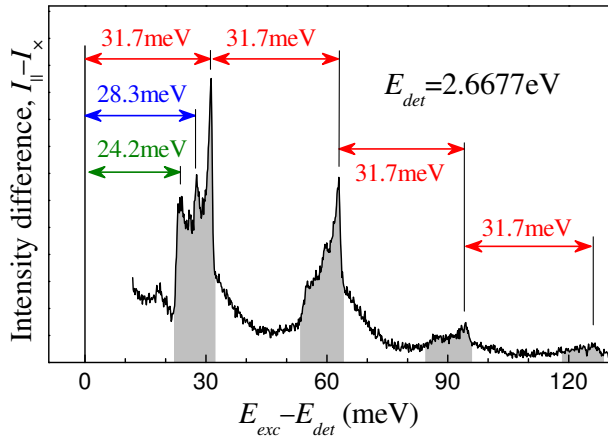


Fig. 5.7: Background corrected PLE. Phonon bands up the fourth order are resolved, which clearly resemble finestructure. In the first order the individual peaks have an energetic distance to the exciting laser of 31.7, 28.3 and 24.2 meV, respectively. The higher orders reproduce the first order phonon band every 31.7 meV without any dispersion, i. e. the energetic position of the finestructure peaks relative to the high energy side of the band remains constant.

other apparently change within the PLE spectrum, but no clear trend can be extracted throughout the development of the phonon band in the spectrum.

Further, a remarkable result is depicted from the 3D spectral map: The energetic width and the finestructure of the phonon bands both do *not* depend at all on the detection position, i. e. they remain constant as they shift through the PL band. It is exclusively the intensity of the difference signal that scales proportional with the intensity of the PL band for excitation conditions between the E2 and E1 states (as displayed in Fig. 5.5b).

A concluding remark on the 3D spectral map concerns the visible horizontal lines in the data. These are clearly artifacts that arise from intensity fluctuations with wavelength change of the dye-laser used in this experiment. From the data taking procedure it is clear that the 3D map was basically constructed line by line vertically. Even though externally stabilized by a feedback controller, the absolute intensities of the exciting laser were only constant to within a few percent and thus translate into fluctuations of up to five percent in the difference signal.

5.2.2 Analysis and discussion

Lowisch *et al.* have observed a very similar phonon band in the PL band as well as in PLE, albeit only in first order, and ascribed these peaks to $\text{Zn}_x\text{Cd}_{1-x}\text{Se}$ ternary alloy modes that arose from material interdiffusion [Low99]. This interpretation cannot explain our data. If the phonon band was to arise from additional phonon modes present due to alloy disorder, the higher order phonon bands would necessarily have to show a broadening. Yet, they do not, in fact ruling out the presence of *any* additional phonon modes, be them ternary alloy or interface phonon modes, the latter of which is a commonly used interpretation upon observation of more exotic phonon modes in QD systems [Rho00, Ngu04]. This statement is further substantiated by Raman studies, which also do not show any phonon modes except for the $\text{ZnSe-LO}(\Gamma)$ at 31.7 meV [Kör08].

The energetic spacing of 31.7 meV of the individual phonon bands strongly suggests a correlation with the $\text{ZnSe LO}(\Gamma)$ -phonon. It has to be stated that 31.7 meV is slightly redshifted with respect to the 31.95 meV that would be expected for a pure $\text{ZnSe LO}(\Gamma)$ -

mode in ZnSe that is pseudomorphically strained to match the GaAs(100) lattice constant. However, as was detailed in section 4.3, even for only one monolayer of CdSe deposited, there is always a small fraction of Cd in the ZnSe layer, which explains this redshift well and renders the designation of the mode unambiguous.

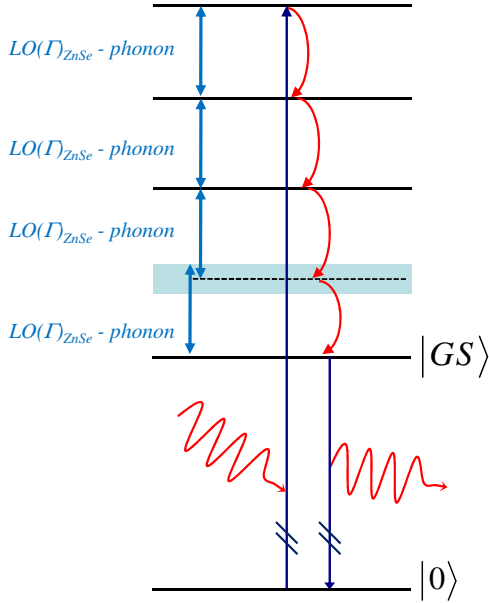


Fig. 5.8: Scattering cascade of excitons excited in the QD embedding material. Incoming photons generate excitons in the ZnSe matrix, which subsequently relax by interaction with LO-phonons. For the final scattering into the QDs k -conservation is lifted due to a finite overlap of the confined exciton wavefunction in the QD and exciton wavefunction in the barrier. As a result a continuum of phonon modes becomes accessible that may participate in the relaxation to the QD ground state. From here the confined excitons radiatively recombine.

Our results are, however, well understood if we assume k -conservation to be relaxed. It is well known from optical investigations on Si and $\text{Si}_x\text{Ge}_{1-x}$ nanocrystals that k -conservation may completely break down in QDs [Kov98, Fuj00]. Due to the indirect bandgap nature of these materials optical transitions in bulk material can only occur by the coupling with phonons and are therefore very inefficient. It is well established that for nanocrystals from these materials the optical gain massively enhances and no-phonon lines appear, which is direct evidence of a lifting of k -conservation.

Under this assumption the appearance of the phonon-band can be understood as presented in Fig. 5.8. Incoming photons create excitons in the ZnSe matrix that relax their excess energy by scattering with the LO-phonon of ZnSe until they are energetically relaxed to above one LO-phonon energy over the QD exciton ground state or slightly below. At this point the phonon interaction can capture the exciton into the QD, where it becomes confined. If for the final relaxation into the QD k -conservation is now lifted, this relaxation is no longer energetically sharp but can occur over a continuum of phonon-states. The fact that the scattering states do not at all depend on the detection energy in the PL band further constitutes that the scattering phonons must belong to the embedding material, as it is hard to conceive that the resulting QDs can be totally uniform over the ensemble. This can certainly be understood from the fact that we are probing extremely small QDs. Recall that even for deposition of three monolayers of CdSe, the resulting QDs are sub 10 nm in lateral and about 1 nm in vertical dimension (see section 4.3.1). For our one monolayer QDs one therefore would also expect a sizeable leakage of the QD

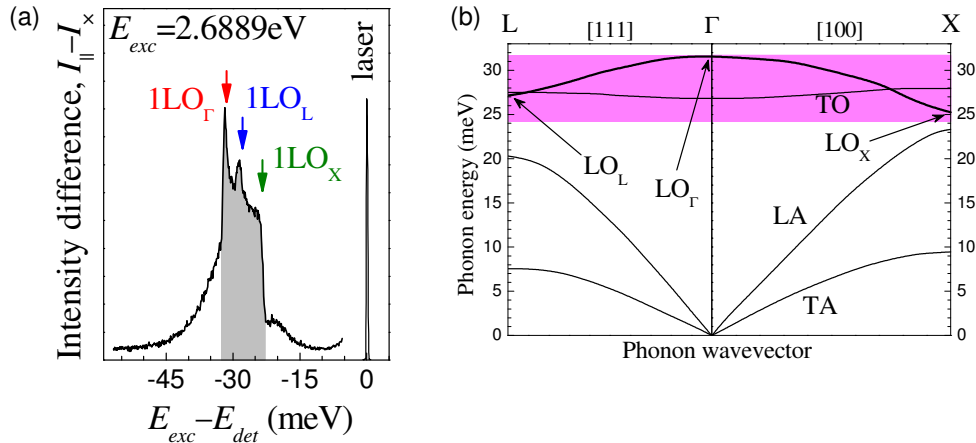


Fig. 5.9: (a): PL-phonon band energy relative to the exciting laser. (b): Phonon Dispersion relation of ZnSe as measured by Hennion *et al.* [Hen71]. The energetic width of the QD phonon band remarkably reproduces the energetic width of ZnSe LO-phonons dispersion. The PL-phonon finestructure peaks almost perfectly coincide with the energetic position of phonons at high symmetry points.

confined exciton wave function into the barrier.

In order to estimate the degree of k -conservation violation in our sample we compare the width of PL-phonon band with phonon dispersion of ZnSe (see Fig. 5.9). We find that the measured spectral width of the PL-phonon band remarkably well reproduces the energetic width of the LO-phonon dispersion as determined by Hennion *et al.* in neutron scattering experiments [Hen71]. The resonance fine structure further appears to relate to specific high symmetry points of the optical-branch. The lowest energetic peak within the PL-phonon band corresponds nicely to the LO-phonon at the X -point of the Brillouin zone with an energy of $E=24.2$ meV, as does the $E=27.2$ meV peak with the L LO-phonon. On balance, in this picture we are able to reconstruct the full LO-phonon dispersion within the Brillouin zone from our experimental data, which would mean that k -conservation is entirely lifted.

Such a complete breakdown of k -conservation could only be explained in two ways. The first would be total disorder in the QD-forming alloy, which is a common explanation in Si and SiGe alloys (see [Fuj00] and the references therein). For such QDs the optical selection rules likewise had to break down due to the absence of any remaining symmetry. This is not the case here as shall be detailed in chapter 6, which is why disorder cannot be a valid explanation. The only possibility then left is that the QD are only of the size of about one monolayer on at least one of the confining axes. With respect to the AFM-data on 3 ML samples this assumption is justified.

In the above picture it is thus possible to understand the physical meaning of the E1 states scanned in the PLE on the integrated PL-intensity as presented in Fig. 5.2. Upon relaxing k -conservation one effectively increases the energetic window in which excitons

may be resonantly excited into the QDs. The E1 states then arise from enhanced photon absorption and do not represent electronic states. This is further substantiated by the observed temperature dependence of the PL, which is best explained without assuming intermediate states that would participate in the thermal activation. It is therefore concluded that for the extremely shallow CdSe QDs in our samples only one exciton level is confined, which consequently is the energy ground state.

The fact that k is no longer conserved in the phonon relaxation also has obvious implication on the energy relaxation in QDs. The vast majority of the theoretical models on phonon energy relaxation in QDs is based on Fermi's golden rule, which incorporates a strict delta function, or neglects the phonon dispersion for other reasons ([Sta00] and references therein). These models are consequently fundamentally flawed and should not be expected to correctly predict energy relaxation rates and times in QDs.

Summary

The data on the exciton-phonon interaction suggest a complete breakdown of k -conservation in shallow CdSe/ZnSe QDs. With a continuum of accessible states for the phonon-interaction of hot excitons excited above the ZnSe barrier and their scattering into the QDs, one can therefore expect fast and efficient exciton capture by the QDs. This is further totally consistent with the absence of a phonon bottleneck as confirmed by the time-resolved PL. It does not rule out the simultaneous relaxation via Auger-like processes by Coulomb scattering [Efr95] but opens an additional effective channel and further adds to the argument of efficient energy relaxation in systems with closely spaced hole levels.

For the QD system under investigation this further implies that the confining potential has to be on the length-scale of a single monolayer at least for one of the confining axes. In combination with the data on the electronic properties as presented in section 5.1 the above finally leads to the conclusion that these QDs only incorporate one exciton confined state, which consequently is the ground state, but may exhibit finestructure as a result of the electron-hole exchange interaction.

Chapter 6

Optical anisotropy of CdSe/ZnSe quantum dots

This chapter is ascribed to the experimental investigation of the sensitive interplay of the QD symmetry and the optical polarization properties with and without external magnetic fields. As was detailed in chapter 3, the reduced symmetry of epitaxially fabricated QDs gives rise to a distinct splitting of the otherwise degenerate bright exciton states, with the final states inheriting an intrinsic degree of linear optical polarization as a result of the enhanced electron-hole exchange interaction and light-heavy hole mixing of the QD valence band ground state. The orientation of the built-in dipole moment of a particular exciton state is determined by the exact shape of the resulting confinement potential.

The experimentally observable anisotropy of the optical polarization of QDs thus provides ample information on the intrinsic QD characteristics that determine highly relevant properties like excitonic spin coherence times and their relaxation channels. With the orientation of the confining potentials varying from dot to dot, the integrated signal over a whole ensemble usually is strongly reduced with respect to a single QD. However, as was demonstrated in chapter 4, the alignment of the individual QDs also may follow a systematic scheme as a consequence of the material properties and the growth details. Upon studying QD ensembles not only the intrinsic properties of the individual QDs but also the global distribution of the QDs resulting from a given growth method can be accessed.

The chapter is divided into two closely related sections. First, the QD intrinsic anisotropy is investigated without external fields applied. It is demonstrated how the electron-hole exchange interaction that is mostly reputed to be unwanted in fact leads to a sizeable effect of polarization conversion, which due to the absence of external fields may be technologically exploitable. From the orientation resolved optical alignment it is further shown how the ensemble arrangement can be restored. In the second section the optical anisotropy of QDs subject to in-plane magnetic fields is studied. The resulting complex polarization behaviour is quantitatively modeled on the basis of a $\mathbf{k}\cdot\mathbf{p}$ -Hamiltonian from which QD key parameters are extracted. The results are discussed with respect to their implications for QD use in non-classical optical device architectures.

6.1 Optical anisotropy in the absence of magnetic fields

This section covers the comprehensive description of the optical anisotropies of strongly confined excitons in CdSe/ZnSe QDs and the interconnection of the latter to the QD confinement potential symmetry. We establish the interplay of the QD symmetry and the optical anisotropy using angle dependent polarization resolved photoluminescence spectroscopy. In this context we demonstrate for the first time efficient optical polarization conversion from circular-to-linear and linear-to-circular polarization by asymmetric QDs upon quasi-resonant excitation under steady state conditions. The effect is observed in the absence of any external fields and arises from the exchange split excitonic finestructure of such QDs. We successfully model the experimental findings by an analytical pseudospin model, which enables the extraction of the experimental key parameters.

Finally, we demonstrate how the full symmetry of the QD ensemble is retained from optical investigations by analyzing the angle dependent optical alignment of the excitons. These findings provide valuable information towards a full theoretical description of the epitaxial QDs.

6.1.1 Optical polarization anisotropy and polarization conversion

In order to study the polarization properties and thus the optical anisotropy of the QDs, the total polarization of the PL is described by a vector $[\rho_v, \rho_l, \rho_c]$ inside the Poincaré sphere. These Stokes coordinates are defined as

$$\rho_v = \frac{I_{[110]} - I_{[1\bar{1}0]}}{I_{[110]} + I_{[1\bar{1}0]}} \quad \rho_l = \frac{I_{[100]} - I_{[010]}}{I_{[100]} + I_{[010]}} \quad \rho_c = \frac{I_{left} - I_{right}}{I_{left} + I_{right}} \quad (6.1)$$

in the sample frame, where $I_{[100]}$, $I_{[010]}$, $I_{[110]}$, $I_{[1\bar{1}0]}$ are the intensities of the linear polarization components along the corresponding crystal axes and I_{left} and I_{right} are the intensities of the left- and rightcircular polarization components, respectively. For these Stokes coordinates the relation $\sqrt{\rho_v^2 + \rho_l^2 + \rho_c^2} \leq 1$ obviously holds. The measurements are then performed with fixed analyzers, while the sample is rotated inside the cryostat with respect to the laboratory frame, as displayed in Fig. 6.1. The angle between these frames is denoted as α . The circular and linear polarization components ρ_{circ}^{lab} and ρ_{lin}^{lab} detected in the laboratory frame relate to the sample frame polarization components as

$$\rho_{circ}^{lab} = \rho_c \quad \rho_{lin}^{lab} = \rho_v \cos 2\alpha - \rho_l \sin 2\alpha. \quad (6.2)$$

For the forthcoming experiments we distinguish between two fundamentally different regimes. For *non-resonant* excitation the laser is tuned above the ZnSe energy barrier. In this regime the photocarriers bear no information about the excitation polarization

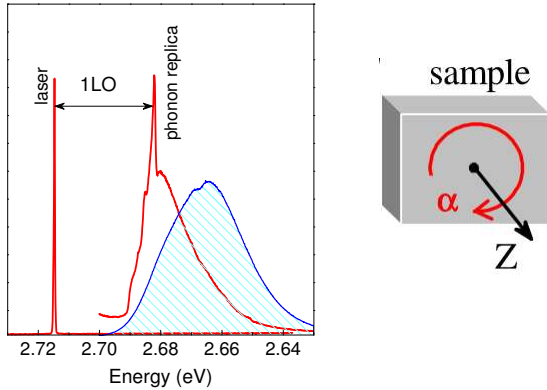


Fig. 6.1: In order to tune the angle α between the incident optical polarization and the crystal axes, the sample is mounted on a rotating holder, enabling rotation around the z -axis (which is the propagation direction of the laser) to an accuracy of 1° . Quasi-resonant excitation is achieved by exciting one ZnSe-LO(Γ)-phonon above the detection energy (i. e. detection is performed on the phonon replica of the laser).

as the relaxation to the ground state includes many scattering events that completely destroy the initial polarization. Under these conditions one therefore probes the intrinsic properties of the respective ground state.

For investigations concerning the QD polarization dynamics it is on the other hand necessary to initialize well defined exciton polarization states. In principal this is achievable by strict resonant excitation into the QD ground state. It is, however, experimentally not straightforward, as under such conditions straylight from the laser energetically coincides with photoluminescence signal and is therefore very difficult to suppress. For these measurements we therefore prepare *quasi-resonant* excitation, which means that the excitation is tuned one ZnSe-LO(Γ)-phonon above the intended detection energy, which is accordingly tuned into the phonon replica of the laser (see Fig 6.1). Due to the fast (sub ps) relaxation via phonons these conditions are well suited for the preparation of coherent exciton states [Sch03a]. For further experimental details refer to Appendix A.

6.1.1.1 Experimental results

Non resonant excitation of the CdSe QDs is obtained for $E_{exc} = 2.83$ eV with the detection set to the spectral maximum of the PL band. The result can be depicted from Fig. 6.2. A residual linear polarization is detected along the $[110]$ crystalline direction. The polarization is best fit with $\rho_0 \cos 2\alpha$ similar to that of a linear polarizer, which indicates an uncompensated net asymmetry of the QD ensemble along this crystal axis. This result stands in perfect agreement with the topological findings obtained by AFM (see Fig. 4.5). Further, the result is independent of the excitation polarization, since for the optical excitation above the ZnSe energetic barrier essentially all spin information is randomized by the time the radiative recombination occurs. Under such conditions one directly probes the structural asymmetry of the QD ensemble. Variation of the detection energy through the PL band only yields minor changes in the magnitude of the fitting parameter ρ_0 , with the overall findings unchanged.

The fact that ρ_0 is constant in the temperature range from 1.6 to 20 K is further conclusive evidence that the uncompensated linear polarization detected for non resonant excitation arises from a partial mixing of light and heavy hole states. A thermal population

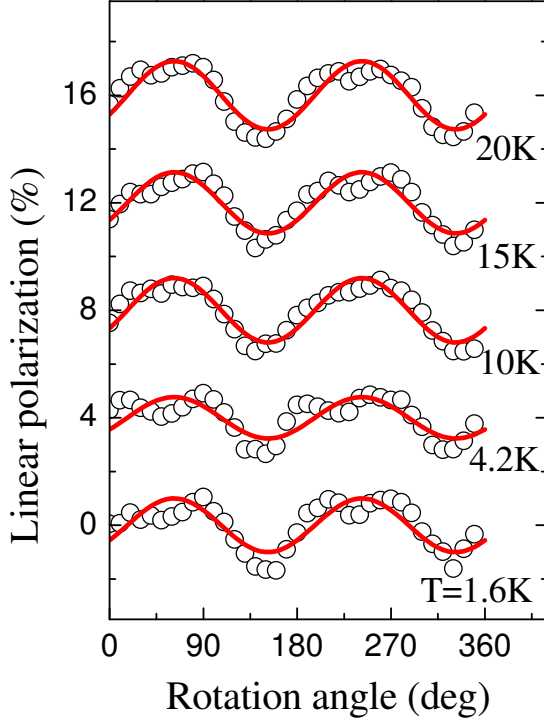


Fig. 6.2: Intrinsic linear polarization observed in the PL band as function of sample orientation for nonresonant excitation ($E_{exc}=2.83$ eV). The degree of linear polarization ρ is well described by $\rho = \rho_0 \cos 2\alpha$ with $\rho_0 \approx 0.02$, which does not vary noticeably over PL band and is further constant for in the temperature range from 1.6 to 20 K. The zero offset for the individual curves is set to integral multiples of 4 %.

of the exchange split exciton ground state cannot explain the observed behavior. For typical values of the fine-structure splitting (FSS) $\delta_1 = \hbar\Omega$ in the range of 0 to 0.5 meV, ρ_0 should rapidly decrease to zero in the above temperature range. It should further exhibit a strong spectral dependence, since for the trions, which are the dominating contribution on the low energy side of the PL band, the FSS vanishes.

An estimate on the degree of the valence band mixing is nevertheless not meaningful from these data, because the absolute value of ρ_0 is statistically averaged over all directions and therefore no good measure for the intrinsic linear polarization of the individual dots. For a reasonable analysis of this valence-band mixing one needs to apply in-plane magnetic fields, which is the subject of section 6.2.

Repeating the above experiment for quasi-resonant excitation alters the picture dramatically as is depicted from Fig. 6.3. Under the condition of fast phonon relaxation, excitons are pumped directly into the QDs. In this case the net linear polarization detected is no longer fixed to the [110] crystal axis but instead depends on the handedness of the exciting circular polarization and varies with $\rho_0 \cos(2\alpha \pm 2\varphi_0)$ where $\varphi = 34^\circ$. This observation implies an effective conversion of circular to linear polarization. To exclude artifacts from the setup, the optical orientation, i.e. the degree of circular polarization in the luminescence upon circular excitation, is also measured. The result (not displayed) shows a net circular polarization of $\ll 1\%$ independent of the sample orientation.

As efficient conversion, we define

$$\rho_l > \rho_v \quad \text{and} \quad \rho_l > \rho_c \quad (6.3)$$

From Fig. 6.3b we can extract the amplitude of the linear polarization, which is

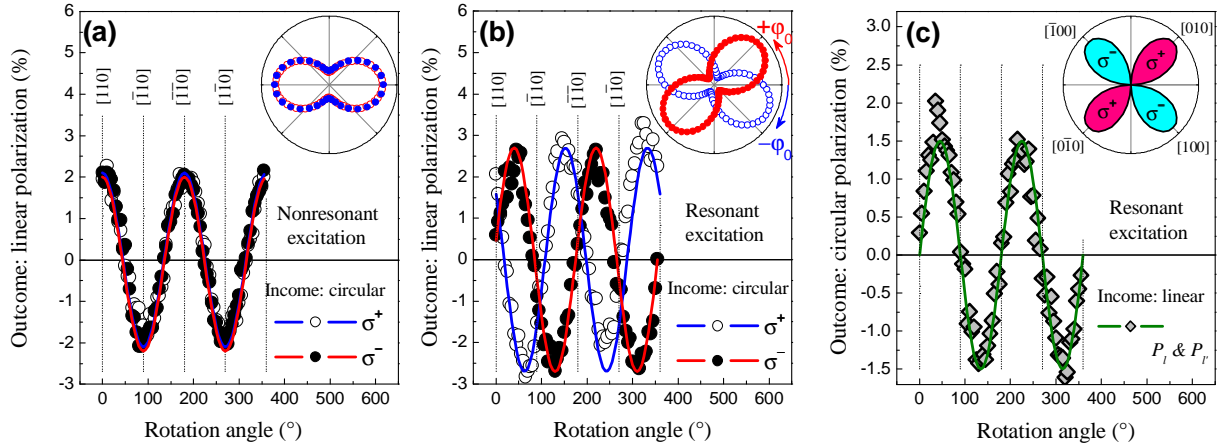


Fig. 6.3: Polarization scans in absence of magnetic fields. **(a)** Degree of linear polarization as function of sample orientation for $E_{exc} = 2.83$ eV above the ZnSe energetic barrier with σ^+ (open symbols)/ σ^- (closed symbols) polarization. Solid lines represent fit with $\rho_0 \cos 2\alpha$. Inset: Same data but in polar coordinates. **(b)** Same as (a) but detected resonantly at the phonon replica with $E_{exc} = 2.714$ eV. The solid curves are fits with $\rho_0 \cos 2(\alpha \pm \varphi_0)$ depending on the handedness of the excitation polarization. **(c)** Degree of circular polarization as function of sample orientation detected under the same resonant conditions as in (b), but with linear excitation polarization. Zero rotation corresponds to polarization set parallel to the [110] crystal axis. The fit is obtained with $\rho_0 \sin 2\alpha$. Inset shows the same data with $|\rho_0 \sin 2\alpha|$, directly displaying effective linear-to-circular polarization conversion.

$\rho_0 = \sqrt{\rho_v^2 + \rho_l^2} = 2.7\%$. This value yields in combination with the characteristic splitting angle $2\varphi_0$ for $\rho_l = \rho_0 \sin 2\varphi_0 = 2.5\%$ and $\rho_v = \rho_0 \cos 2\varphi_0 = 1.0\%$. For our experimental values Eq. 6.3 is obviously fulfilled.

As there are no magnetic fields applied, time reversal symmetry must be preserved. Therefore, the opposite effect, namely linear-to-circular polarization conversion, must also be observable. Keeping the energetic positions of excitation and detection constant at quasi-resonance, the excitation is hence set linearly polarized and the degree of circular polarization is detected. The result displayed in Fig. 6.3c unambiguously proves the existence of linear-to-circular polarization conversion. In a final check experiment, the excitation is tuned back above the ZnSe barrier, with the polarization excitation again linear and detection scheme unchanged. Under these conditions no circular polarization component is detectable. It is therefore concluded that indeed optical polarization conversion is observed.

In a final experiment we monitor the evolution of the characteristic splitting angle $2\varphi_0$ as function of the excitation position. For this measurement we therefore tune the position of the phonon replica of the laser line over the PL band and repeat the circular-to-linear polarization conversion experiment. The result is displayed in Fig. 6.4. For excitation from 2.70 to 2.71 eV $2\varphi_0$ slightly increases from 67° to 74° and is hence constant on that level to ~ 2.73 eV. Above this value $2\varphi_0$ rapidly decays to zero. Detecting on the

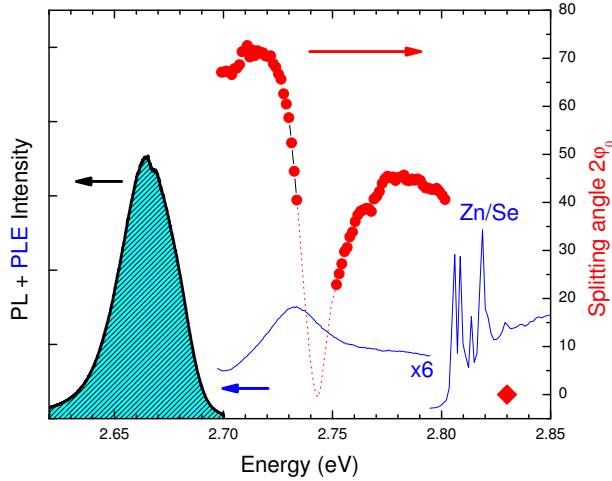


Fig. 6.4: Spectral dependence of the circular-to-linear optical polarization conversion efficiency on the excitation conditions. Plotted is the characteristic splitting angle 2φ in degree versus excitation energy. For reference the position of the PL band and the integrated PLE signals are included. Clearly, for excitation in the vicinity of QD excited states the conversion is suppressed.

second order phonon replica, a splitting angle of 22° is detectable for $E_{exc} > 2.755$ eV that monotonically increases to 40° for $E_{exc} = 2.776$ eV. This trend continues for detection on the third order phonon replica above 2.776 eV until $2\varphi_0$ saturates at a value of 46° at ~ 2.78 eV. In the vicinity of the ZnSe barrier the splitting angle is then slightly decreasing and is strictly zero for excitation above.

The breakdown of polarization conversion in the range from 2.73 to 2.75 eV is clearly associated with the presence of the E1 QD excited states, which is readily seen by comparing the above data with the PLE data. It appears that the relaxation with non- Γ -point phonons weakens or completely suppresses the coherent excitation of the exciton polarization state. This may be understood primarily as a dephasing effect, where individual QDs still have a well defined exciton initial state, yet the ensemble coherence is lost as a result of the slightly varying QD intrinsic properties that will give rise to interaction with different phonons. Due to the altered relaxation dynamics the conversion mechanism is apparently suppressed.

6.1.1.2 Analysis and discussion

One key observation is that the conversion only occurs under phonon-assisted quasi-resonant excitation. With circular excitation one excites a coherent superposition of the two linearly polarized eigenstates of FSS exciton that is conserved due to the rapid relaxation on the 1-ps timescale [Fli01]. Observations of quantum beats in the time domain [Tar04] directly showed the precession of the circularly polarized PL with a frequency $\Omega = \frac{\delta E}{\hbar}$. Thus, the presence of a preferential direction for excitonic states, as induced by the e-h exchange interaction in low symmetry QDs, gives rise to quantum interferences. For such a system optical polarization conversion has been theoretically predicted by Ivchenko *et al.* [Ivc91]. Obviously, a magnetic field aligned in the sample plane can give rise to a preferential direction. This kind of magnetic field-induced optical polarization conversion was previously observed experimentally on GaAs/AlAs superlattices [Dzh97]. In contrast, we report for the first time on optical polarization conversion in the complete

absence of external fields.

The experimental results are well described using a pseudospin approach and utilizing the correspondence of the Poincaré and Bloch sphere concepts. We recall that any two level system can be described in terms of a spin formalism. Here, the bright exciton states split by $\delta_1 = \hbar\Omega$ form such a system. In zero magnetic field, the pseudospin Hamiltonian then takes the form [Kus05]

$$\mathcal{H} = \frac{\hbar}{2}\Omega\sigma_x \quad (6.4)$$

with σ_x being the Pauli matrix. The eigenstates of the system in terms of optical polarization states are given by

$$|+\rangle = \frac{1}{\sqrt{2}}(|1\rangle + |-1\rangle); \quad |-\rangle = \frac{1}{\sqrt{2}}(|1\rangle - |-1\rangle); \quad (6.5)$$

where $|1\rangle, |-1\rangle$ correspond to pure σ^+, σ^- polarization (see also section 3.2). We now define a pseudospin $\mathbf{S} = [S_1, S_2, S_3]$, identifying the spin components as the polarization components of our Stokes vectors by

$$\rho_v = S_1; \quad \rho_l = S_2; \quad \rho_c = S_3; \quad (6.6)$$

The time evolution of the polarization of the PL-signal represented by this pseudospin \mathbf{S} is then described by the well-known kinetic equation [Mei84]:

$$\frac{\partial \mathbf{S}}{\partial t} = \boldsymbol{\Omega} \times \mathbf{S} - \frac{\mathbf{S} - \mathbf{P}_{\text{eq}}}{\tau_s} - \frac{\mathbf{S} - \mathbf{P}_{\text{ex}}}{\tau_0}. \quad (6.7)$$

Here τ_0 is the radiative lifetime of the exciton, τ_s the spin dephasing time, \mathbf{P}_{ex} the polarization vector of the excitation and \mathbf{P}_{eq} the equilibrium polarization vector. In our case $\mathbf{P}_{\text{eq}} = [\Gamma_{lin}, 0, 0]$, with Γ_{lin} being the observed net linear polarization along the [110] axis under nonresonant excitation, arising from the linear dichroism and thermal population of the FSS exciton states. As no magnetic fields are present, $\boldsymbol{\Omega} = [\Omega, 0, 0]$ consistent with the Hamiltonian in eq. (6.4). For the steady-state condition of our experiment $\frac{\partial \mathbf{S}}{\partial t} = 0$, hence for arbitrarily polarized excitation $\mathbf{P}_{\text{ex}} = [P_v, P_l, P_c]$ eq. (6.7) yields

$$\rho_v = \frac{T}{\tau_0}P_v + \frac{T}{\tau_s}\Gamma_{lin} \quad (6.8)$$

$$\rho_l = \frac{T}{\tau_0} \left[-\frac{\Omega T}{1 + (\Omega T)^2}P_c + \frac{1}{1 + (\Omega T)^2}P_l \right] \quad (6.9)$$

$$\rho_c = \frac{T}{\tau_0} \left[+\frac{1}{1 + (\Omega T)^2}P_c + \frac{\Omega T}{1 + (\Omega T)^2}P_l \right] \quad (6.10)$$

with $T^{-1} = \tau_s^{-1} + \tau_0^{-1}$. From Eq. (6.9) and Eq. (6.10) one can readily depict how the linear and circular optical polarization components of the excitation and PL intermix. These equations are certainly an approximation, as they do not take into account dark exciton states or valence band mixing, but succeed in describing the experimental findings.

For efficient conversion it is necessary that $\tau_0 \leq \tau_s$, which is in agreement with the observed long dephasing times in the QD ground state [Sch03b, Mac04] that generally exceed the radiative lifetime of excitons by far. As an example, the spin relaxation time of a single hole was found to be on the order of 10 ns [Fli03], which is about two orders of magnitude larger than the typical τ_0 for bright excitons. Consistently, no conversion is observed for exciton injection above the ZnSe barrier or into the E1 QD excited states. Under such conditions $\tau_0 \geq \tau_s$ and all but the intrinsic linear polarization Γ_{lin} decay to zero.

The conversion further goes to zero for $\Omega = 0$ and $\Omega \rightarrow \infty$, which means that only a fraction of the QDs with proper FSS contribute to effective conversion. Comparison to our data yields $\sqrt{\langle \Omega^2 \rangle} T \approx 10$. With τ_0 on the order of several hundred ps, this corresponds to an FSS of some ten μeV . It is directly derived from the above equations, that a maximum conversion of $\rho_l = \rho_c = 50\%$ is obtained for $\Omega T = 1$. However, for such effective polarization conversion, the FSS must be on the order of only a few μeV .

The fact that the characteristic splitting angle $2\varphi_0$ is near constant in the excitation range from 2.70 to 2.73 eV is evidence that the net asymmetry of the QDs is not varying much over the ensemble, i.e. $\sqrt{\langle \Omega^2 \rangle} T \approx 10$ holds over the complete PL band. This stands in perfect agreement to the fact that the amplitude of the built-in linear polarization observed for non-resonant excitation is almost constant over the ensemble, as any net asymmetry affects both exciton fine structure and the valence band mixing.

Finally, the evolution of $2\varphi_0$ above 2.775 eV is ascribed to a change in the relative efficiency of the exciton capture by the E1 QD excited states and the subsequent relaxation into the QD ground state.

6.1.2 Optical polarization alignment and ensemble symmetry

Figure 6.5 shows the optical alignment, i.e. the degree of linear polarization of the emission ρ_{lin}^{lab} excited by linearly polarized light along the same direction P_{lin} . The optical alignment is much larger than the circular-to-linear conversion and varies in a range of $\rho_{lin}^{lab} = 25\text{--}28\%$ in the case of resonant excitation ($E_{exc} = 2.714$ eV). Surprisingly, the optical alignment shows only a weak dependence on whether the linear polarization of the excitation is set along $\langle 110 \rangle$ or $\langle 100 \rangle$ directions.

For qualitative explanation we consider an inhomogeneous distribution of QDs in the sense that their confining potentials are asymmetric along different directions. For simplicity they are considered to have the same absolute value of anisotropic exchange splitting $\hbar\Omega$. This assumption is reasonable with respect to analysis in section 6.1.1, where it was established that the net asymmetry is not varying much over the QD ensemble. The relative number of these dots is denoted by $N_{[110]} + N_{[1\bar{1}0]} + N_{[100]} + N_{[010]} = 1$. By analyzing the inbuilt linear polarization shown in Fig. 6.3a we establish the following interrelations

$$N_{[110]} > N_{[1\bar{1}0]} \quad N_{[100]} = N_{[010]}. \quad (6.11)$$

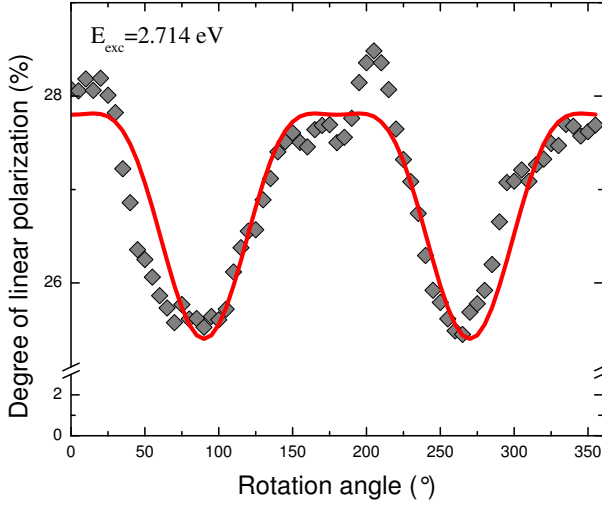


Fig. 6.5: Angle scan of optical alignment detected under quasi-resonant excitation. Solid curve is a simulation assuming an inhomogeneous distribution of the asymmetric QDs (see text for details).

From Eq. 6.2 we further directly obtain

$$P_V = P_{lin} \cos 2\alpha \quad \text{and} \quad P_L = -P_{lin} \sin 2\alpha \quad . \quad (6.12)$$

According to Eqs. (6.8) and (6.9) the contribution to the optical alignment coming from $\langle 110 \rangle$ dots is therefore

$$\rho_V = (N_{[110]} + N_{[1\bar{1}0]}) \frac{T}{\tau_0} P_{lin} \cos 2\alpha + (N_{[110]} - N_{[1\bar{1}0]}) \frac{T}{\tau_s} \Upsilon_{lin} \quad (6.13)$$

and

$$\rho_L = -(N_{[110]} + N_{[1\bar{1}0]}) \frac{T}{\tau_0} \frac{1}{1 + (\Omega T)^2} P_{lin} \sin 2\alpha \quad . \quad (6.14)$$

Following Eqs. (6.8) to (6.10) the efficient conversion that we observe in Fig. 6.3, means $\Omega T \gg 1$. Because of the factor $\frac{1}{1 + (\Omega T)^2} < 1$ in Eq. (6.14) this means $\rho_V > \rho_L$ and thus the contribution of the $\langle 110 \rangle$ dots to ρ_L can safely be neglected. In analogy, we obtain for the QDs elongated along $\langle 100 \rangle$

$$\rho_L = -(N_{[100]} + N_{[010]}) \frac{T}{\tau_0} P_{lin} \sin 2\alpha \quad . \quad (6.15)$$

After substituting Eqs. (6.13) and (6.15) in Eq. (6.2) we obtain

$$\rho_{lin}^{lab} = (\Sigma_{\langle 110 \rangle} \cos^2 2\alpha + \Sigma_{\langle 100 \rangle} \sin^2 2\alpha) \frac{T}{\tau_0} P_{lin} + \Delta_{\langle 110 \rangle} \cos 2\alpha \frac{T}{\tau_s} \Upsilon_{lin} \quad . \quad (6.16)$$

Here, $\Sigma_{\langle 110 \rangle} = N_{[110]} + N_{[1\bar{1}0]}$, $\Sigma_{\langle 100 \rangle} = N_{[100]} + N_{[010]}$ and $\Delta_{\langle 110 \rangle} = N_{[110]} - N_{[1\bar{1}0]}$. Using Eq. (6.16) the best fit with experimental data has been achieved with $\Sigma_{\langle 110 \rangle} \frac{T}{\tau_0} P_{lin} = 26.6\%$, $\Sigma_{\langle 100 \rangle} \frac{T}{\tau_0} P_{lin} = 27.3\%$ and $\Delta_{\langle 110 \rangle} \frac{T}{\tau_s} \Upsilon_{lin} = 1.2\%$ as shown by a solid line in Fig. 6.5. The deviation of the fit from the data clearly arises from the spatial inhomogeneity of the QD distribution and is therefore an artifact from the measurement. As we rotate the sample,

the position at which the PL is excited can be shifted by several hundred microns. This movement is extremely hard to avoid, because it requires optical adjustment perfectly along the rotation axis. Apart from this detail, the overall agreement with the data is good. We further obtain $\Sigma_{\langle 110 \rangle} \approx \Sigma_{\langle 100 \rangle}$, which is in agreement with other studies [Kus05].

For the derivation of Eqs. (6.8) to (6.10) it was explicitly assumed that only QDs asymmetric along $\langle 110 \rangle$ contribute to the conversion and accordingly we set $\mathbf{\Omega} = [\Omega, 0, 0]$ in Eq. (6.7). Given our above results we are now in a position to extend our model such that it accounts for FSS-split bright excitons confined to dots with asymmetric potentials along $\langle 110 \rangle$ and $\langle 100 \rangle$. Without external magnetic field we hence obtain $\mathbf{\Omega} = [\Omega_{\langle 110 \rangle}, \Omega_{\langle 100 \rangle}, 0]$, where $\hbar\Omega_{\langle 110 \rangle}$ and $\hbar\Omega_{\langle 100 \rangle}$ are the average anisotropic exchange splittings for $\langle 110 \rangle$ and $\langle 100 \rangle$ dots, which we approximated to be equal (see above). For resonant circularly polarized excitation Equations (6.9) and (6.10) are then modified following the inhomogeneous distribution of QDs to

$$\rho_l = -\Delta_{\langle 110 \rangle} \frac{T}{\tau_0} \frac{\Omega T}{1 + (\Omega T)^2} P_c \quad \rho_c = (\Sigma_{\langle 110 \rangle} + \Sigma_{\langle 100 \rangle}) \frac{T}{\tau_0} \frac{1}{1 + (\Omega T)^2} P_c. \quad (6.17)$$

With these equations and a full set of data covering all possible polarization interrelations we are able to restore the complete inhomogeneous distribution of the QD ensemble. In the limit of long spin relaxation ($T/\tau_0 \sim 1$) we obtained $\rho_l = 2.5\%$, $\rho_c = 1\%$ and $\Omega T \approx 10$. Based on Eqs. (6.16) and (6.17) we deduce from Fig. 6.3 the values $N_{[110]} = 0.37$, $N_{[\bar{1}\bar{1}0]} = 0.11$, $N_{[100]} = N_{[010]} = 0.26$. Such a distribution is schematically presented in Fig. 6.6.

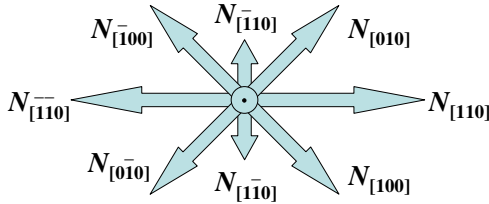


Fig. 6.6: Schematics of the anisotropy in a CdSe/ZnSe QD ensemble. Lengths of arrows indicate the partial number of QDs elongated along corresponding crystalline directions (see text for details). The following numbers are found based on the analysis of angle scans for the optical conversion and alignment (orientation): $N_{[110]} \equiv N_{[\bar{1}\bar{1}0]} = 0.37$, $N_{[1\bar{1}0]} \equiv N_{[\bar{1}10]} = 0.11$, and $N_{[100]} \equiv N_{[\bar{1}00]} = N_{[010]} \equiv N_{[0\bar{1}0]} = 0.26$.

Summarizing, we have shown how a complete characterization of the optical anisotropy of a QD ensemble can restore the net asymmetry of an inhomogeneous distribution of QDs. This method is an invaluable tool for the characterization of QDs *after* capping as it provides direct access to the resulting potential distribution. Moreover, when applied to single QDs, the above formalism can be used to completely characterize the QD potential geometry. Finally, the above equations also yield the possibility to estimate the spin-dephasing times τ_s when combined with time resolved measurements. While τ_s is known to by far exceed the radiative lifetime of excitons bound to QDs, there are still barely any absolute values available from the literature. Comprehensive time-resolved and steady-state experiments are a promising option to overcome this shortcoming.

6.2 Optical anisotropy induced by in-plane magnetic fields

This section is devoted to the in-depth investigation of the optical polarization properties of excitons confined to low symmetry QDs subject to in-plane magnetic fields, i. e. magnetic fields applied perpendicular to the growth direction. The interplay of the anisotropic exchange interaction and isotropic and anisotropic Zeeman terms leads to a complex polarization behavior that can only be accounted for by considering higher order terms in the Zeeman Hamiltonian.

We begin with the presentation of the experiment and results. It is demonstrated that the observed highly non trivial polarization behavior can be separated into two main contributions that correspond to linear polarizations whose polarization axes either rotate in opposite direction to that of an applied magnetic field or remain fixed to a given crystalline direction. In a qualitative analysis based on the exciton pseudospin Hamiltonian it is then unambiguously evidenced that these polarization components are induced by isotropic and anisotropic contributions of the heavy-hole Zeeman term, respectively. At low temperatures, the latter is shown to be capable of compensating the built-in uniaxial anisotropy present in the absence of external fields, therefore resulting in an optical response for highly symmetric QDs.

In the final step a comprehensive quantitative analysis of the above results is provided that accounts for the exchange induced excitonic fine structure, the magnetic field induced Zeeman shifts and the low-symmetry induced contribution of the light-hole states to heavy-hole exciton. With the unique set of parameters provided by the analysis one is able to follow the temperature evolution of the optical polarization behavior and establish fundamental trends, which are of high relevance for possible device schemes that employ QDs as sources of nonclassical light.

6.2.1 Experimental results

For the studies on the magneto-optical polarization anisotropy external magnetic fields up to $B = 4$ T were applied in Voigt geometry. The detection axis was set to an angle of either $\gamma = 45^\circ$ or $\gamma = 0^\circ$ with respect to the magnetic field axis. Both are kept fixed during the measurements. The degree of linear polarization ρ_γ^l in the PL is defined as

$$\rho_\gamma^l(\alpha) = \frac{I_\gamma - I_{\gamma+90^\circ}}{I_\gamma + I_{\gamma+90^\circ}} \quad (6.18)$$

where I_γ and $I_{\gamma+90^\circ}$ label the intensity of the linearly polarized PL component along the respective direction as displayed in Fig. 6.7. Hence, ρ_γ^l is detected as function of sample orientation, where α now denotes the angle between the $[1\bar{1}0]$ crystal direction and the magnetic field direction, which were set parallel at the beginning of each sweep. For a comprehensive analysis, the experiments presented below were performed on the exact

same sample discussed in section 5.1. The results, however, have been confirmed on a vast number of samples to ensure the general nature of our experimental findings.

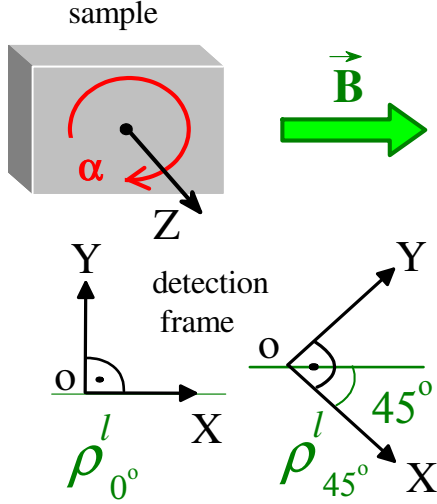


Fig. 6.7: Detection scheme of the angle resolved experiments with applied in-plane magnetic fields where α denotes the rotation angle of the sample with $\alpha = 0$ meaning \mathbf{B} is pointing along the $[1\bar{1}0]$ crystalline direction. The detection frame ρ_γ is rotated by an angle γ with respect to the magnetic field \mathbf{B} where γ is set either to 45° or 0° .

The excitation energy was set to $E_{exc} = 2.76$ eV, i. e. below the ZnSe band edge but above the exciton mobility edge (refer to Fig. 5.2). To completely rule out memory effects on the photo-generated excitons that would spoil the analysis, the exciting beam was passed through a wedge depolarizer before being directed onto the sample. The detection energy was subsequently chosen at the high energy side of the PL ($E_{det} = 2.68$ eV) to ensure mainly charge neutral excitons are probed. This is in contrast to previous work that dealt with the magneto-optical anisotropy of negatively charged trions [Kou04].

The result of angle scans of $\rho_{45^\circ}^l$ for varying magnetic fields at $T = 1.6$ K is shown in Fig. 6.8. For zero applied field only a second spherical harmonic resulting from the shape asymmetry is observed (Note that the detection axis is tilted by 45° with respect to the data presented in Chapter 5, which gives rise to the phase shift of the below data compared to the data in section 5.1). As the magnetic field is ramped up, the amplitude of this second spherical harmonic is decreased. Moreover, an additional fourth spherical harmonic arises. At a critical field $B_c \approx 0.4$ T the second spherical harmonic vanishes and a pure fourth spherical harmonic is observed. As the magnetic field is further increased, a second spherical harmonic appears again, yet with inverted sign. Finally, above 1 T the response saturates with both second and fourth harmonics present. Summarizing, the data follows a relation

$$\rho_{45^\circ}^l(\alpha) = a_2 \sin 2\alpha + a_4 \sin 4\alpha \quad (6.19)$$

where the amplitude of the fourth spherical harmonic amplitude a_4 steadily increases until it saturates at higher fields and the second spherical harmonic amplitude a_2 steadily decreases, starting from positive and going to negative values, until it also saturates at higher fields. The zero crossing point of a_2 marks the critical field B_c .

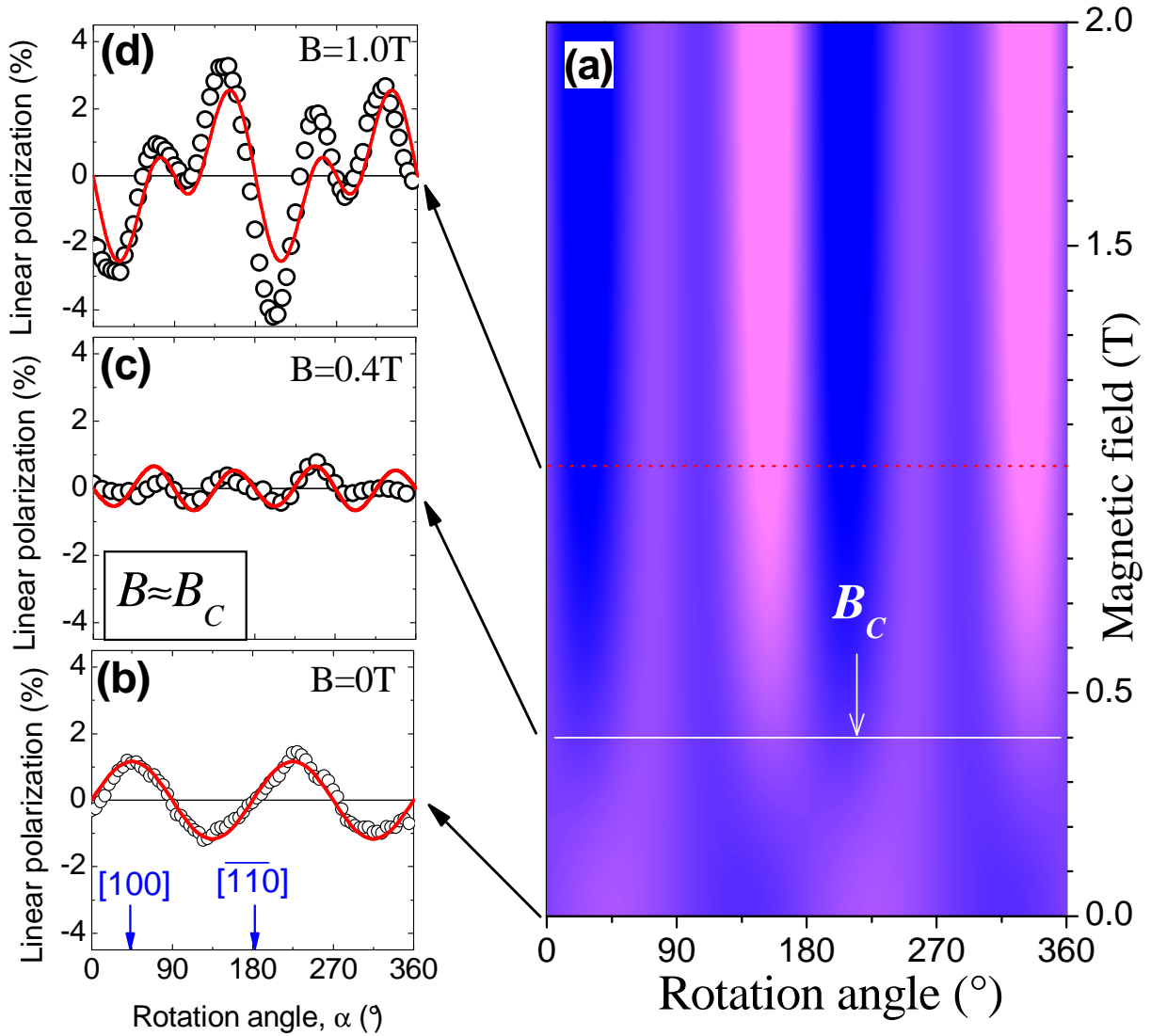


Fig. 6.8: (a) 3D plot of the linear polarization $\rho_{45^\circ}^l$ as function of rotation angle α and magnetic field B . Blue (dark) and magenta (light) areas correspond to negative and positive values of the linear polarization $\rho_{45^\circ}^l$. The subfigures (b)-(d) represent slices through the 3D map for distinct magnetic fields with open symbols representing raw data and red lines being best fits according to Eq. 6.19. (b) For zero applied magnetic field only the second spherical harmonic arising from the QD shape anisotropy is present. (c) For a critical field $B_c \approx 0.4$ T a pure fourth spherical harmonic is observed. (d) Both, second and fourth spherical harmonics are observed for higher fields. Note that the amplitude of the second spherical harmonic changes sign with respect to the zero field amplitude after passing through B_c .

As in the above geometry no zeroth spherical harmonic component can be observed, the experiment was repeated for $\gamma=0^\circ$. For this geometry the data follows the relation

$$\rho_{0^\circ}^l(\alpha) = a_0 + a_2 \cos 2\alpha + a_4 \cos 4\alpha \quad (6.20)$$

where a_2 and a_4 are identical to the coefficient extracted from Eq. 6.19. Remarkably, even

in this geometry the a_0 is vanishingly small. A summary of the B-field evolution of a_0 , a_2 and a_4 is shown in Fig. 6.11. To within our experimental error of $\pm 0.2\%$ we find $a_0 \approx 0$.

The temperature evolution of the magneto-optical response in the high field saturation regime is summarized in Fig. 6.9.

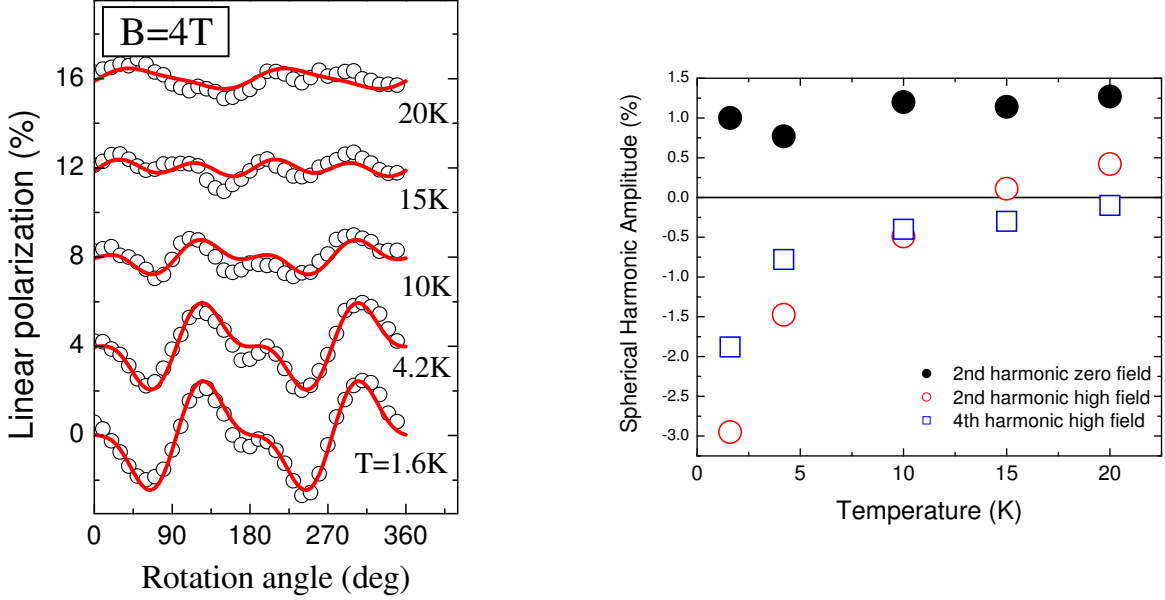


Fig. 6.9: Left panel: Temperature evolution of the linear polarization $\rho_{45^\circ}^l(\alpha)$ in the saturation regime at $B = 4$ T. Note that the magnetic field was applied along the $[110]$ -direction in this measurement, so there is a phase shift of 90° with respect to the data shown in Fig. 6.8. Right panel: Spherical harmonic contributions as function of temperature extracted from linear polarization in the saturation regime to the left and at zero field (see Fig. 6.2). Solid lines are guide to the eye.

In contrast to the zero field measurements, in which the built-in polarization is almost constant in the above temperature range, the amplitudes of the second and fourth spherical harmonics invoked by the in-plane magnetic fields exhibit a pronounced temperature dependence. The absolute value of the coefficient a_4 monotonically decreases and at 20 K is already reduced to about 10 % of its value at 1.6 K. For a_2 the situation is more complex in the saturation regime. Up to 15 K the absolute value of a_2 steadily reduces, yet the sign of a_2 remains inverted with respect to the zero field linear polarization. At 15 K and above no sign reversal of a_2 is observed anymore and the saturation value of a_2 approaches the zero field value of a_2 . Summarizing, both the magnitude of a_4 and the field induced change in a_2 rapidly approach zero as the temperature rises.

For the interpretation of these data it is helpful to discuss how the different harmonic signals relate to the rotation of the axis of linear polarization and to the rotation of the magnetic field. This is best done considering the situation inside the sample frame, as this simplifies the forthcoming analysis in a significant manner. The different contributions recognized in the experiment are displayed in Fig. 6.10.

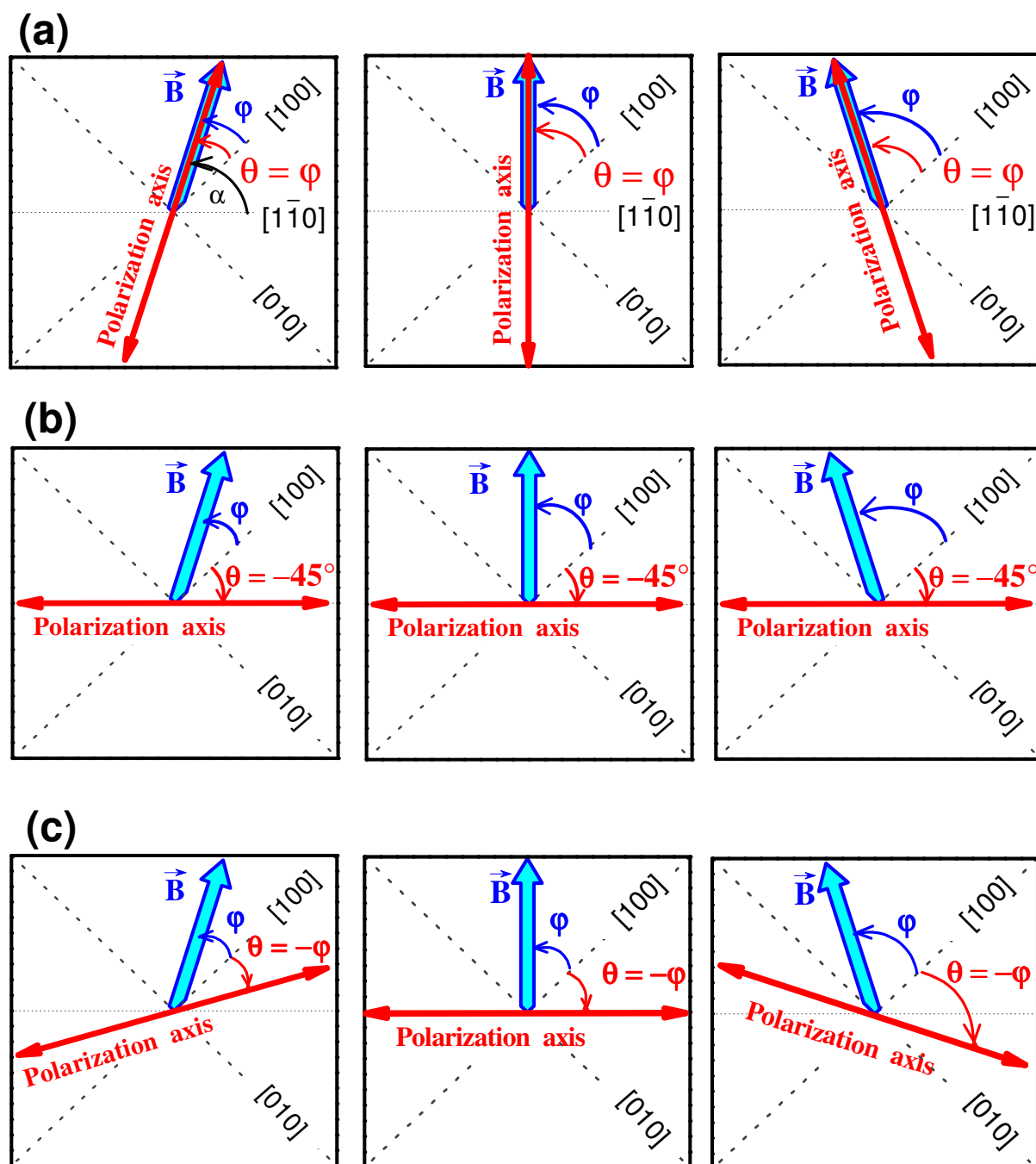


Fig. 6.10: Different scenarios for the relative rotation of the linear optical polarization axis in the photoluminescence signal and the magnetic field vector in the sample frame, sketched for increasing rotation angle of the magnetic field vector φ from left to right. (a) Both rotate in the same direction linked to each other, which is the situation encountered in a classical Voigt experiment. (b) The optical polarization axis is linked to one of the crystal axis and does not rotate at all, irrespective of the orientation of the magnetic field. (c) The magnetic field vector and the polarization axis rotate in opposite direction with $\theta = -\varphi$.

In the sample frame the position of the crystal axes remains fixed and the magnetic field is rotated (in opposite direction to the rotation of the sample in the laboratory frame). It is therefore useful to define additional angles, so let θ denote the rotation-angle of the magnetic field vector and φ denote the rotation angle of the linear polarization axis, both with respect to the [100] crystal axis.

Fig. 6.10(a) shows the situation in which the magnetic field vector and polarization axis align parallel for all angles $\theta = \varphi$. As the detection axis is fixed relative to the magnetic field vector, such a behavior would give rise to a constant signal for all rotation angles. i. e. a zeroth spherical harmonic contribution. This scenario corresponds to what would be expected from a classical Voigt experiment. Obviously, this is not at all observed in our data, as the a_0 contribution is zero within the experimental uncertainty.

For observation of a second spherical harmonic it is evident from the above that the axis of the polarization vector must be fixed to a distinct crystal axis independent of the orientation of the magnetic field vector. This situation is displayed in Fig. 6.10(b). Here, the polarization axis is linked to the [110] axis in accordance to the results without magnetic fields. In this case $\varphi = 45^\circ$ for all θ . With a moments thought, it is hence clear that a fourth spherical harmonic is recorded when magnetic field vector and polarization axis rotate in opposite direction, yielding $\theta = -\varphi$ (see Fig. 6.10(c)). Obviously, the latter two contributions are simultaneously present in our data. On balance, the in-plane magnetic field vector gives rise to a highly non-trivial rotation behavior of the linear polarization axis inside the sample plane.

6.2.2 Qualitative discussion

A similar polarization behavior was previously observed by Kusrayev *et al.* in narrow magnetic CdTe/(Cd,Mn)Te Quantum Wells (QWs) subject to in-plane magnetic fields [Kus99]. Specifically, they observed both second and fourth spherical harmonic contributions in addition to the dominating zeroth spherical harmonic expected for QWs. Using a pseudo-spin approach they were able to explain the appearance of a second harmonic signal assuming an extreme in-plane anisotropy of the heavy-hole g -factor $g_{hh}^{xx} = -g_{hh}^{yy}$ that could be caused by a low-symmetry perturbation of the QW. The manifestation of a fourth harmonic contribution remained unexplained, but it was speculated that magnetic polaron formation might give rise to such a signal. The latter hypothesis can obviously not apply in our QD system, which is not containing any magnetic moments.

In subsequent theoretical work based on a microscopic approach it was demonstrated that the observed polarization anisotropy was caused by the interplay of two sources [Sem03]. Specifically, these are correlations between the electron and HH phases of the wavefunctions resulting from the interaction with the in-plane magnetic field and a small admixture of the LH states to the HHs, both of which are caused by low symmetry perturbations in the QW. No excitonic effects have been considered in this work, in particular the electron-hole exchange interaction was ignored. In light of the importance

of the latter for our QD system this approximation, which may only be minor in QWs, is too rough in our case.

For a principle understanding of the physical mechanisms that give rise to the complex polarization behavior observed in our QD system, we consider a pseudospin formalism to be a good starting point [Kus99]. Therefore we define by $|+S_n\rangle$ and $|-S_n\rangle$ the wave functions of an electron ($n = \text{el}$) or hole ($n = \text{hh/lh}$) with pseudo-spin projection $\pm S$ along the z -direction, which is the direction normal to the sample plane (i. e. [001]). The Hamiltonian describing the system then takes the form

$$\mathcal{H}_n = \frac{\delta_n}{2}(\sigma_x \cos \theta_n + \sigma_y \sin \theta_n), \quad (6.21)$$

where δ_n denotes the magnetic-field induced energy splitting in the conduction ($n = \text{el}$) or the valence ($n = \text{hh/lh}$) band, and θ_n denotes the angle of the magnetic field with respect to the [100] crystal axis in accordance with the above definition. σ_x and σ_y denote the Pauli matrixes. This Hamiltonian has the eigenfunctions

$$\Psi_n^{+1} = \frac{1}{\sqrt{2}}e^{-i\frac{\theta_n}{2}}(|+S_n\rangle + e^{-i\theta_n}|-S_n\rangle) \quad \Psi_n^{-1} = \frac{1}{\sqrt{2}}e^{-i\frac{\theta_n}{2}}(|+S_n\rangle - e^{-i\theta_n}|-S_n\rangle) \quad (6.22)$$

To consider the optical transitions one has to take into account the dipole momentum operator \hat{P} . We define by the unit vectors $\hat{u}_x||$ [100] and $\hat{u}_y||$ [010] the unit vector for right- and left-circular handedness as $\hat{u}_\pm = (\hat{u}_x \pm i\hat{u}_y)/\sqrt{2}$. Following from the optical selection rules for electrons and holes at $\mathbf{k} = 0$ established in section 3.1.2, the matrix elements of \hat{P} for heavy hole transitions then take the form $\langle \pm \frac{1}{2}\text{el} | \hat{P} | \pm \frac{3}{2}\text{hh} \rangle = \mp \hat{u}_\pm$. With the eigenfunctions of the system defined in Eq. (6.22) we therefore obtain the following optical transitions

$$\langle \Psi_{el}^\eta | \hat{P} | \Psi_{hh}^\mu \rangle \propto -\hat{u}_+ + \eta\mu e^{i(\theta_{hh} - \theta_{el})}\hat{u}_-. \quad (6.23)$$

with $\eta, \mu = \pm 1$. From that one can readily see that the optical transitions are linearly polarized forming an angle of $\theta = \frac{1}{2}(\theta_{hh} - \theta_{el})$ for $\eta = -\mu$, or $\theta = \frac{1}{2}(\theta_{hh} - \theta_{el}) + 90^\circ$ for $\eta = \mu$ with respect to the [100] axis. In order to establish the optical spectra as function of relative orientation of the crystal axes and the magnetic field, one now has to follow closely the evolution of the splitting of the individual bands. For an electron subject to an external magnetic field B the Zeeman Hamiltonian defined in Eq. (3.30) takes the form

$$\mathcal{H}_{el} = \frac{1}{2}g_{el}^\perp \mu_B (\sigma_x B \cos \varphi + \sigma_y B \sin \varphi), \quad (6.24)$$

where g_{el}^\perp is the electron g -factor of the studied material system and μ_B is the Bohr magneton. Thus, by comparison with Eq. 6.21 one directly finds $\theta_{el} = \varphi$.

For the valence band the situation is more complicated. In D_{2d} symmetry, the interaction of holes with an in-plane magnetic field can be described by the following Hamiltonian (see section 3.2.1)

$$\mathcal{H}_{D_{2d}} = q_0 g_0 \mu_B (J_x^3 B \cos \varphi + J_y^3 B \sin \varphi), \quad (6.25)$$

where g_0 is the free electron g -factor and q_0 the Luttinger coefficient defining the hole g -factor for bulk material. For the description of the optical transition of heavy holes, one can simplify Eq. 6.26 as the matrix components of J_x^3 and J_y^3 related to the angular momentum of heavy holes behave as $\frac{3}{4}\sigma_x$ and $-\frac{3}{4}\sigma_y$, respectively (see appendix B) and Eq. 6.25 becomes:

$$\mathcal{H}_{hh} = \frac{3}{4}q_0 g_0 \mu_B (\sigma_x B \cos \varphi - \sigma_y B \sin \varphi) , \quad (6.26)$$

By comparing Eq. 6.26 with Eq. 6.21 one obtains $\theta_{hh} = -\varphi$, which in combination with the response of the electron then gives an overall rotation angle for the axis of the linear polarization of $\theta = -\varphi (+90^\circ)$. Checking with Fig. 6.10 shows this corresponds to a fourth spherical harmonic contribution in the optical response.

However, as is known from the previous results, the true symmetry of the QD system is $C_{2\nu}$. For those systems one has to add the following contribution to the Hamiltonian of Eq. 6.26

$$\mathcal{H}_{C_{2\nu}} = q_1 g_0 \mu_B (J_x^3 B \sin \varphi + J_y^3 B \cos \varphi) , \quad (6.27)$$

The factor q_1 depends on the deformation of the QDs and is $C_{2\nu}$ invariant. For HHs Eq. 6.27 reduces to

$$\mathcal{H}'_{hh} = \frac{3}{4}q_1 g_0 \mu_B (\sigma_x B \sin \varphi - \sigma_y B \cos \varphi) , \quad (6.28)$$

Keeping in mind the above it is directly conceived that this contribution yields $\theta_{hh} = \varphi - 90^\circ$ resulting in an overall rotation of the polarization axis of $\varphi = \pm 45^\circ$. Thus, the reduced symmetry gives rise to a second spherical harmonic contribution. Moreover, its axis coincides with the axis of linear polarization arising from the shape asymmetry of the QDs in zero magnetic field.

As is established from the magneto-optical anisotropy in the absence of magnetic field, there also is a small admixture of the light holes to the excitons present, so we also discuss what the impact of the light hole states to the magneto-optical anisotropy would be. From the dipole momentum operator \hat{P} the light hole transitions take the form $\langle \pm \frac{1}{2}el | \hat{P} | \mp \frac{1}{2}hh \rangle = \pm \hat{u}_\pm$. The eigenfunctions established in Eq. 6.22 therefore yield for LHs the transitions

$$\langle \Psi_{el}^\eta | \hat{P} | \Psi_{lh}^\mu \rangle \propto -\mu \hat{u}_+ + \eta e^{i(\theta_{lh} + \theta_{el})} \hat{u}_- . \quad (6.29)$$

Like in the case of HH the LH transitions are therefore linearly polarized, but their angle of rotation comes out to be $\theta = \frac{1}{2}(\theta_{hh} + \theta_{el})$ for $\eta = \mu$ and $\theta = \frac{1}{2}(\theta_{hh} + \theta_{el}) + 90^\circ$ for $\eta = -\mu$ with respect to the [100] axis. The matrix components of J_x^3 and J_y^3 related to the angular momentum of light holes are described by $\frac{5}{2}\sigma_x$ and $\frac{5}{2}\sigma_y$, respectively. The high symmetry part of the Hamiltonian for the valence band (Eq. 6.25) takes the form

$$\mathcal{H}_{lh} = \frac{5}{2}q_0 g_0 \mu_B (\sigma_x B \cos \varphi + \sigma_y B \sin \varphi) , \quad (6.30)$$

In complete analogy to the considerations on the HHs one obtains $\theta_{lh} = \varphi$, which combined with the result for the electrons would yield a rotation for LH transitions of $\theta = \varphi$. This means that the axis of the linear polarization for the isotropic part of the LH transition aligns always parallel to the magnetic field direction, which has been shown in section 6.2 to be equivalent to a zeroth spherical harmonic contribution in the data. Within the experimental uncertainty of our experiment, no such signal is observed. This is a striking fact, as the above considerations do not depend on the direction in which the low symmetry QDs align. In other words, while the contribution on the zero field optical anisotropy of the LH is averaged over the different resulting directions of the individual QDs in the ensemble, the full LH component is observed in the magneto-optical anisotropy data. It is therefore possible to estimate an upper boundary for the admixture of LHs to the HH states. With a maximum zeroth spherical harmonic signal of 0.2 % even in the high magnetic field limit, the contribution of the LHs to the optical polarization signal must be at least one order of magnitude smaller than the HH contribution. LH are therefore ignored for the remainder of the analysis.

For sake of completeness we shall briefly note what the anisotropic contribution of the LHs would be. From the above, Eq. 6.27 transforms to

$$\mathcal{H}'_{lh} = \frac{5}{2}q_1 g_0\mu_B (\sigma_x B \sin \varphi + \sigma_y B \cos \varphi) , \quad (6.31)$$

and this contribution yields $\theta_{lh} = \varphi - 90^\circ$ resulting in an overall rotation of the polarization axis of $\varphi = \pm 45^\circ$. In light of the facts that $q_1 \ll q_0$ and the overall admixture of the LH is already vanishing the anisotropic LH contribution to the magneto-optical polarization anisotropy is negligible.

In **summary** the above discussion on the basis of the exciton pseudospin Hamiltonian unambiguously demonstrates that the fourth and second harmonic contributions in the data are induced by the isotropic and anisotropic contributions of the heavy-hole Zeeman term. In detail, the magneto-optical polarization signal observed for the QDs is caused by the fact that the high and low symmetry components of the heavy-hole Zeeman term impose specific phase correlations of the HH and the electron. This means that the appearance of a pure fourth spherical harmonic as observed in a magnetic field of $B_C=0.4$ T corresponds to signal expected for a QD of perfect D_{2d} symmetry. Explicitly, the application of an in-plane magnetic field can result in a compensation of the otherwise present uni-axial anisotropy induced by the shape of the confining potential and, moreover, enables a sensitive tuning of the potential asymmetry. This result is of high potential relevance in the light of possible QD device schemes, which calls for a more rigorous, quantitative analysis.

6.2.3 Quantitative analysis

For a quantitative analysis a more detailed approach is required which is provided below. The essential experimental data are summarized in Fig. 6.11, in which the amplitudes of the spherical harmonics are plotted, i.e. the coefficients a_0 , a_2 and a_4 , extracted from the fits of the experimental data on $\rho_\gamma^l(\alpha)$ using Eq. 6.20 vs magnetic field.

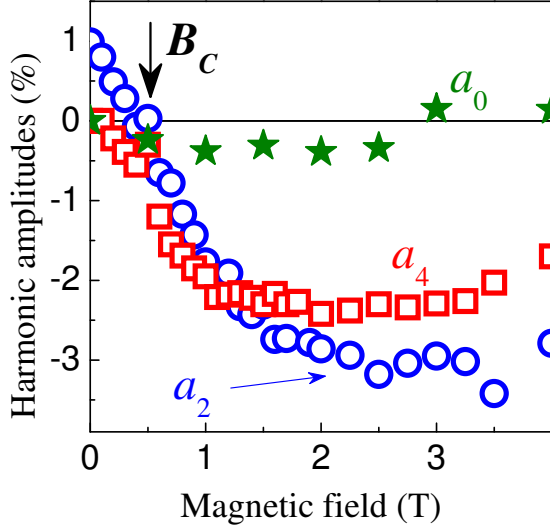


Fig. 6.11: Evolution of the harmonic amplitudes as function of applied magnetic field at $T = 1.6$ K. Plotted are the values of the harmonic amplitudes extracted from raw data using Eq. 6.20. B_C designates the critical magnetic field for which the second harmonic signal vanishes.

We deduce from the qualitative discussion on the basis of a pseudospin model that the contribution of the light holes admixed to excitons confined to our QDs is very small. The following analysis shall therefore be limited to heavy-hole excitons. As discussed in section 3.2, the electron-hole exchange interaction is significant in QDs and therefore a corresponding term \mathcal{H}_{ex} must be included in the forthcoming analysis. Consistent with the results obtained in section 6.1 and the formalism described in section 3.2 we denote by δ_0 the splitting between the $|\pm 1\rangle$ (bright) and $|\pm 2\rangle$ (dark) heavy-hole exciton states. For the corresponding C_{2v} symmetry of our QDs \mathcal{H}_{ex} further leads to a splitting $\delta_2 < \delta_0$ of the dark exciton states and a splitting δ_1 of the radiative doublet observed for the bright exciton states.

In the basis of the heavy-hole exciton states $\Phi_{1,2} = |\pm 1\rangle$ and $\Phi_{3,4} = |\pm 2\rangle$, the final spin Hamiltonian $\mathcal{H} = \mathcal{H}_{el} + \mathcal{H}_{hh} + \mathcal{H}'_{hh} + \mathcal{H}_{ex} + \mathcal{H}'_{ex}$ then takes the following matrix form (compare to Eqs. 3.27 and 3.31)

$$\mathcal{H} = \frac{1}{2} \begin{pmatrix} \delta_0 & -i\delta_1 & \delta_{el} & \delta_{hh} \\ i\delta_1 & \delta_0 & \delta_{hh}^* & \delta_{el}^* \\ \delta_{el}^* & \delta_{hh} & -\delta_0 & \delta_2 \\ \delta_{hh}^* & \delta_{el} & \delta_2 & -\delta_0 \end{pmatrix}. \quad (6.32)$$

Here, $\delta_{el} = \mu_B g_{el}^\perp B_+$ and $\delta_{hh} = \mu_B (g_{hh}^i B_+ + i g_{hh}^a B_-)$ are in-plane Zeeman terms for electrons and holes, respectively, where $g_{hh}^i = \frac{3}{2}g_0q_1$ and $g_{hh}^a = \frac{3}{2}g_0q_2$ denote the isotropic and anisotropic contributions to the heavy-hole g-factor. $B_\pm = B e^{\pm i\varphi}$ are the effective magnetic fields.

In the high magnetic field limit ($|\delta_{hh}|, |\delta_{el}| \gg |\delta_0|, |\delta_1|, |\delta_2|$) this Hamiltonian can be solved analytically. The corresponding normalized eigenfunctions $\Psi_j = \Sigma V_{nj} \Phi_n$ and the energy eigenvalues E_j of Hamiltonian (6.32) are then found by

$$V = \frac{1}{2} \begin{pmatrix} 1 & 1 & 1 & 1 \\ e^{2i\theta} & -e^{2i\theta} & -e^{2i\theta} & e^{2i\theta} \\ -e^{-i\theta_{el}} & e^{-i\theta_{el}} & -e^{-i\theta_{el}} & e^{-i\theta_{el}} \\ -e^{i\theta_{hh}} & -e^{i\theta_{hh}} & e^{i\theta_{hh}} & e^{i\theta_{hh}} \end{pmatrix}, \quad (6.33)$$

$$E_{1,4} = \mp |\delta_{el}| \mp |\delta_{hh}|; \quad E_{2,3} = \pm |\delta_{el}| \mp |\delta_{hh}|.$$

Here $e^{i\theta_{el}} = \delta_{el}/|\delta_{el}|$, $e^{i\theta_{hh}} = \delta_{hh}^*/|\delta_{hh}|$ and $e^{2i\theta} = e^{i(\theta_{hh}-\theta_{el})}$ have the same meaning as in Eq. (6.23). Eqs. (6.33) perfectly reproduce the results of the qualitative discussion presented in section 6.2.2 above.

For a given finite magnetic field the eigenenergies E_j and eigenfunctions Ψ_j of Hamiltonian 6.32 can be calculated numerically. From the Ψ_j s it is possible to extract the intensity and polarization of the observed luminescence. Since only the $\Phi_{1,2} = |\pm 1\rangle$ excitons are optically active, the optical matrix element in an arbitrary direction \mathbf{e} for the eigenfunction Ψ_j is determined by $M_j(\mathbf{e}) = -V_{1j}e_+ + V_{2j}e_-$ [Pik93]. It is then possible to calculate the intensity of the linearly polarized component of the luminescence along an axis rotated by an angle ξ with respect to the [100] crystalline axis by $I_{j,(\xi)} = |M_j(\mathbf{e}||\xi)|^2$.

The polarization of the PL from an ensemble of QDs must be averaged over the thermal population of exciton states, and can be expressed in the sample frame by

$$\rho'_{(\xi)} = K \frac{\sum_j P_j (I_{j,(\xi)} - I_{j,(\xi+90^\circ)})}{\sum_j P_j (I_{j,(\xi)} + I_{j,(\xi+90^\circ)}), \quad (6.34)$$

where $P_j = e^{-E_j/k_B T}$ is the Boltzmann factor. K is a phenomenologic scaling factor which accounts for spin relaxation in the ensemble and basically determines the saturation level of the polarization at high magnetic fields. The physical reasoning of this factor is understood from the following considerations. The four optical active states of the pure HH exciton all have the same oscillator strength. The axis of the optical polarization of transitions from the energies E_1 and E_4 (also referred to as the *outer states*) is further perpendicular to the axis of the optical polarization contained in the transitions from the energies E_2 and E_3 (consequently labeled as the *inner states*). That is, the total polarization observed in the PL over the complete HH excitons recombination as defined by Eq. 6.18 is zero if all four states are equally populated.

With the optical pump conditions under which the discussed experiments were performed, the excitation probability is to good approximation equivalent for all four HH states as the excitonic interlevel spacing is negligible against the energetic distance between the exciton ground states and the mobility edge levels. The absolute degree of the optical polarization observable in ensemble PL is therefore determined by the ability of the excitons to thermalize. It is well established that the spin relaxation time τ_s is large

against the radiative lifetime of excitons τ_0 in QDs (e. g. [Sch03b, Mac04]) from which it is directly conceived that K should be small. Microscopically K will be defined by the scattering of the excitons on acoustic phonons and fluctuations in the confining potentials of the individual QDs.

Using Eq. (6.34) the linear polarizations $\rho'_{(100)}$ and $\rho'_{(1\bar{1}0)}$ in the sample frame were calculated. From this, the polarizations in the laboratory frame are ultimately found by

$$\rho_{0^\circ}^l(\alpha) = \rho'_{(1\bar{1}0)} \cos 2\alpha + \rho'_{(100)} \sin 2\alpha \quad (6.35)$$

$$\rho_{45^\circ}^l(\alpha) = \rho'_{(1\bar{1}0)} \sin 2\alpha - \rho'_{(100)} \cos 2\alpha. \quad (6.36)$$

The corresponding spherical harmonic amplitudes extracted from the optical polarization rotation obtained by equation by Eq. (6.35) can then be directly compared to the experimental values shown in Fig. 6.11, which is done for the best fit parameters in Fig. 6.12.

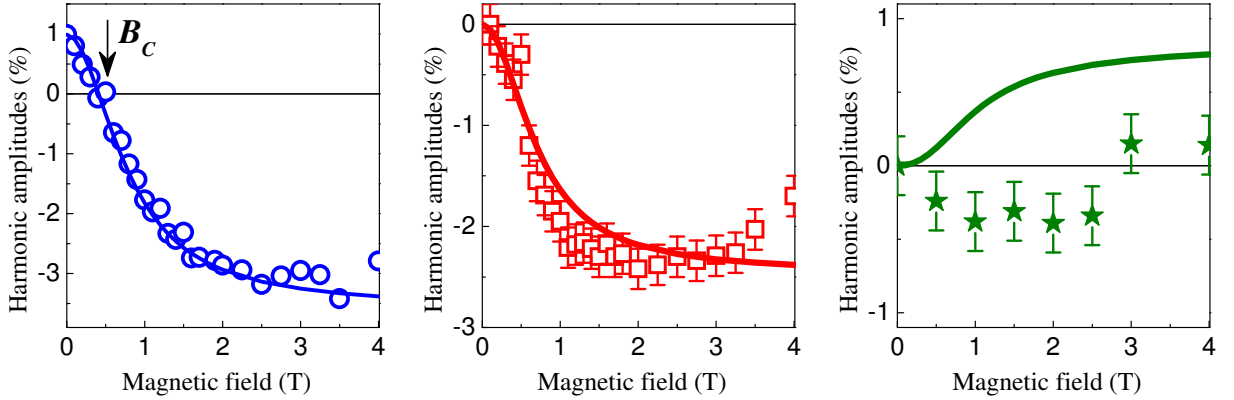


Fig. 6.12: Direct comparison of the data (symbols) and the best fit model calculation (solid lines) on the magnetic field dependence of the spherical harmonic amplitudes for $T=1.6$ K. From left to right the panels show a_2 (blue), a_4 (red) and a_0 (olive).

The fitting procedure was done iteratively along the following considerations. The value of δ_1 unambiguously sets the value of a_2 for $B=0$, while g_{hh}^i and g_{hh}^a define the saturation value of a_4 and a_2 , respectively, at high magnetic fields for a given g_e^\perp . The fact that all saturation values are scaled by the same K sets a hard condition for the choice of g_e^\perp , because the difference in the saturation values of a_2 and a_4 is hence solely determined by g_e^\perp . By definition $\delta_0 > \delta_2$ and it is therefore clear that δ_0 defines the zero crossing of a_2 for a given temperature, as it basically sets the relative population between the (in the notation of zero-magnetic field) dark and bright exciton states. Once K , δ_1 , g_e^\perp , g_{hh}^i and g_{hh}^a are determined by the saturation values of a_2 and a_4 for zero and high magnetic field, δ_0 exclusively defines the value of B_C . Finally, δ_2 determines the curvature the B-field dependence of a_2 and a_4 and therefore defines how quickly the saturation values of a_2 and a_4 are acquired with increasing magnetic field.

With the above procedure we were able to reproduce the magnetic field dependence of a_2 , a_4 and a_0 at $T=1.6$ K using a unique set of parameters. The result is displayed in Fig. 6.12. The best fit was acquired for taking the coefficient $K = 0.05$, substituting for the exchange energies $\delta_0 = 2.8$ meV, $\delta_2 = 0.20$ meV, $\delta_1 = 0.12$ meV and setting the g-factors to $g_e^\perp = 1.0$, $g_{hh}^i = 0.55$ and $g_{hh}^a = 0.60$. The agreement between model and data is remarkably good for a_2 and a_4 . The appearance of a non-zero a_0 in the model calculation is not intuitively obvious and arises from the interplay of the Zeeman and the e-h exchange terms. Generally speaking, the value of a_0 increases the more the ratio of δ_1 to δ_2 deviates from one. This can be understood by close inspection of the resulting eigenfunctions. In the high field limit (see Eq. 6.33) as well as in the Pseudospin considerations *only* the Zeeman terms are considered, which give rise to an overall of four states, out of which two pick up a relative phase shift of strictly π with respect to the other two. The addition of the exchange contribution will further result in a phase pickup that is different for all four states and will manifest in the optical signal as an out phase linear optical polarization component, i. e. a small degree of ellipticity. This ellipticity in return will be picked up by the linear polarization detection assembly as a constant signal or zeroth spherical harmonic contribution.

As no such signal can be identified in the experimental data within noise, the boundary condition a_0 sets on the model calculation is a_0 to be minimal, while a_2 and a_4 are still well met. The above fitting procedure result is robust within ± 5 % on the individual values found for the best fit parameters and stands moreover in good agreement with the value of the bright exciton splitting extracted from the polarization conversion data in section 6.1.1.

It is further possible to compare the optical polarization as function of sample orientation as calculated by the model directly to the experimental raw data. Exemplary results of the calculations for different magnetic fields and detector configurations are displayed and compared to experimental data in Fig. 6.13. The small deviation between model and experiment for non zero magnetic fields that is recognized in the plot is attributed to a slight spatial inhomogeneity of the sample. Note that the data themselves are somewhat asymmetric upon rotation by 180° . For signals that contain only second and fourth harmonic contributions this should not at all be the case. It is however readily understood from the data taking procedure. As described in section 6.2 the detection scheme remains fixed while the sample is rotated. It is essentially impossible to align the optical axis such that it perfectly coincides with the axis around which the rotation occurs. As such, the position of the laser spot on the sample moves by a tiny amount as the sample is rotated and as a consequence the ensemble that is optically probed slightly changes, at which point any spatial inhomogeneity of the QD sample will be relevant. In a simple check experiment it was therefore verified that the principal picture is conserved upon moving the detection on the sample surface to different places but consistently found that the absolute values of the various optical polarization coefficient exhibit a scatter of ± 0.5 %, as they do in Fig. 6.13.

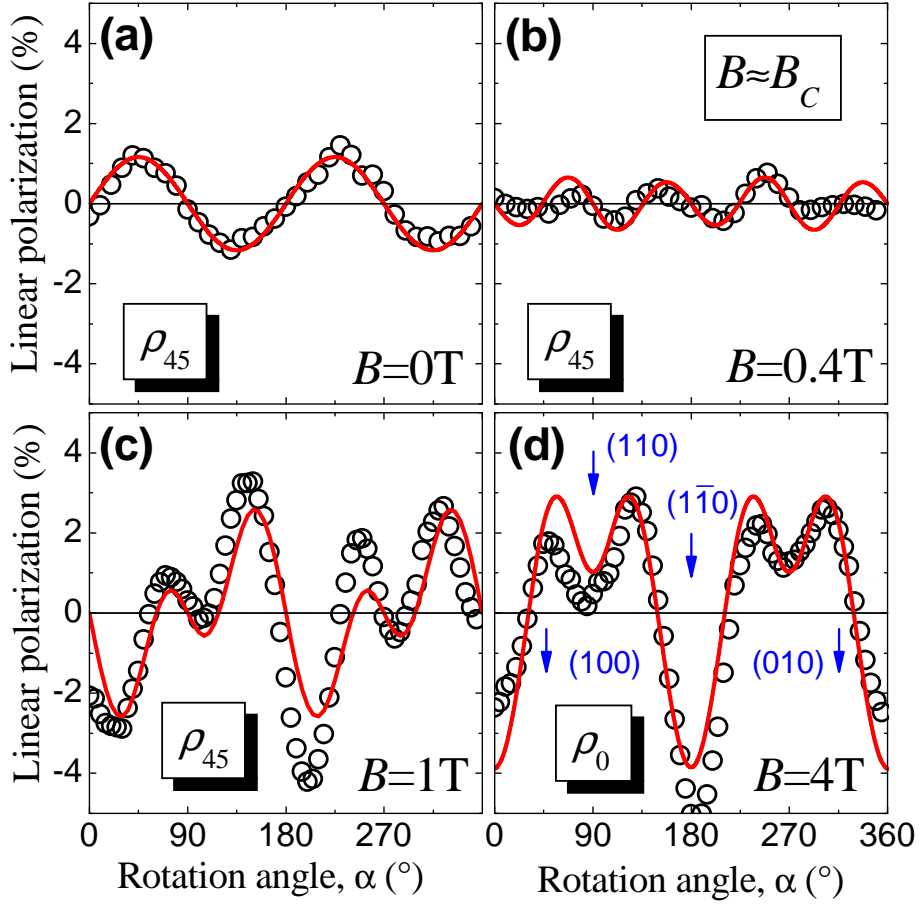


Fig. 6.13: Quantitative simulation based on the heavy-hole exciton Hamiltonian compared to raw data. Open symbols represent raw data recorded at different magnetic fields and for different analyzer configurations as indicated in the individual panels. The solid lines are the result of the respective numeric simulation procedure described by Eqs. 6.32 through 6.36.

The full evolution of the magneto-optical anisotropy of excitons at $T = 1.6$ K calculated for the analyzer configuration ρ_{45° is displayed in Fig. 6.14a. By comparing to the data displayed in Fig. 6.8 it is conceived that the model succeeds in quantitatively describing the experimental data as function of magnetic field strength *and* sample orientation. In perfect agreement with the data the model finds a compensating field B_C for a_2 of 0.42 T, which coincides with the experimental value.

Using the best fit parameter set the model is further used to describe the temperature dependence of the optical polarization. For these calculations the values of the exchange splittings and g-factors are left unchanged with respect to the best fit values extracted at $T=1.6$ K, but the temperature is varied to match the according data points displayed in Fig. 6.9. For direct comparison the values of the spherical harmonic amplitudes at $B=4$ T, which is deep in the saturation regime at $T=1.6$ K, were calculated as function of temperature and are displayed in Fig. 6.15.

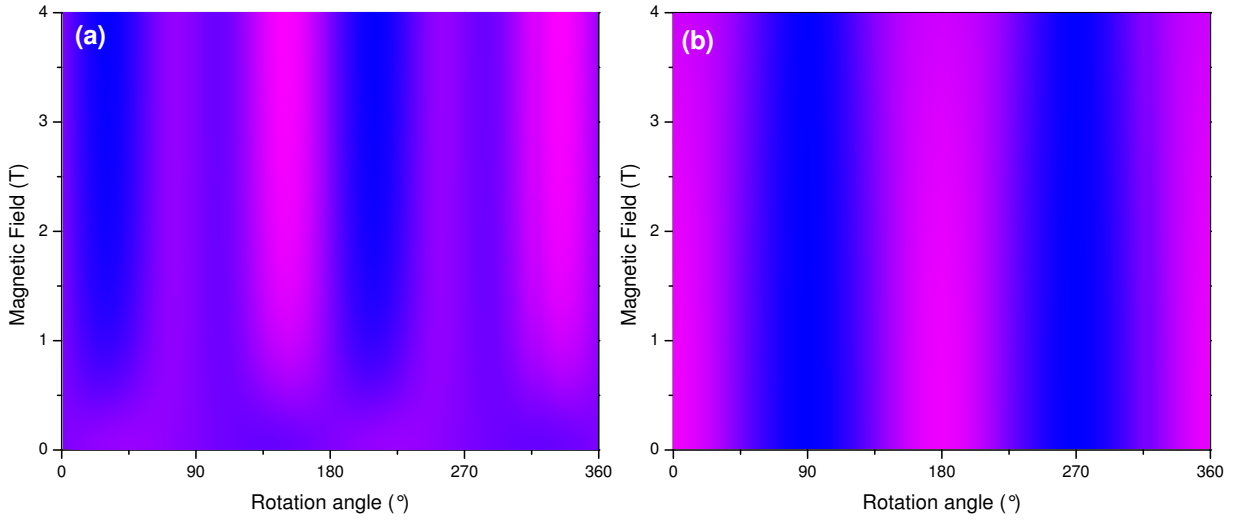


Fig. 6.14: 3D plot of the linear polarization ρ_{45}^l as function of rotation angle α and magnetic field B as derived from the model calculations. **(a)** For a sample temperature of $T = 1.6$ K the model is in superb agreement with the experimental data (compare to Fig. 6.8.) **(b)** At $T = 10$ K the signal remains almost unchanged up to $B = 3.5$ T. At $B = 4.0$ T the second harmonic is reduced but not inverted, with only a very weak fourth harmonic appearing.

It can first generally be stated that the model covers all trends observed in the data well, in particular a_4 approaches zero as the temperature is increased and the sign reversal for a_2 as function of magnetic field no longer occurs. It is therefore concluded that the model covers all the relevant physics necessary to describe the temperature evolution of the optical polarization in transverse magnetic fields. Quantitatively a_4 is, however, predicted to more rapidly approach zero than observed in the experiment. The disappearance of the a_2 crossover is further shifted to about $T \approx 4$ K, which is clearly less than the observed value of just below 15 K (see Fig. 6.9).

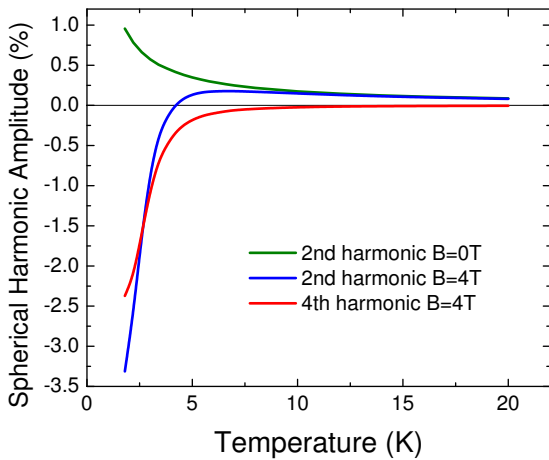


Fig. 6.15: Evolution of the second and fourth spherical harmonic amplitudes a_2 and a_4 in the saturation regime for $B = 4$ T as function of temperature as extracted from the model. Note that a_2 changes sign at $T \approx 4$ K, whereas a_4 monotonically approaches zero for increasing T .

Neither the exchange splittings nor the g-factors are to first order temperature dependent. Therefore only two reasons can be considered to understand the deviation between

our data and the model calculations. First, the empirical factor K that accounts for the spin relaxation could exhibit a temperature dependence. Given its microscopic origin, fluctuations in the QD confining potentials and phonon scattering, K should increase as the number of phonons in the system increases with rising temperature. This would result in an increase of the values of the spherical harmonic amplitudes and could compensate the rapid decrease to some degree. It can, however, neither explain the shift in the zero-crossover of a_2 nor the experimentally observed total lack of change in a_0 with increasing temperature.

Second, there could be an influence of the experimentally established (small) LH-admixture to the QD excitons, which the model does not account for. As stated in section 6.1.1 the HH-LH mixing will give rise to fixed phase relations for the right-circular and left-circular polarization components of the resulting excitons and therefore result in a net linear polarization component even in the case of equal thermal population of the exchange and magnetic field split exciton states. It is easily conceived that such an intrinsic degree of linear polarization changes the evolution of the optical polarization as function of temperature and will further be the dominant observed mechanism at high temperatures. As this reconciles with the data in zero magnetic fields, it is concluded that the deviations between data and model indeed arise from the neglect of the LH contribution.

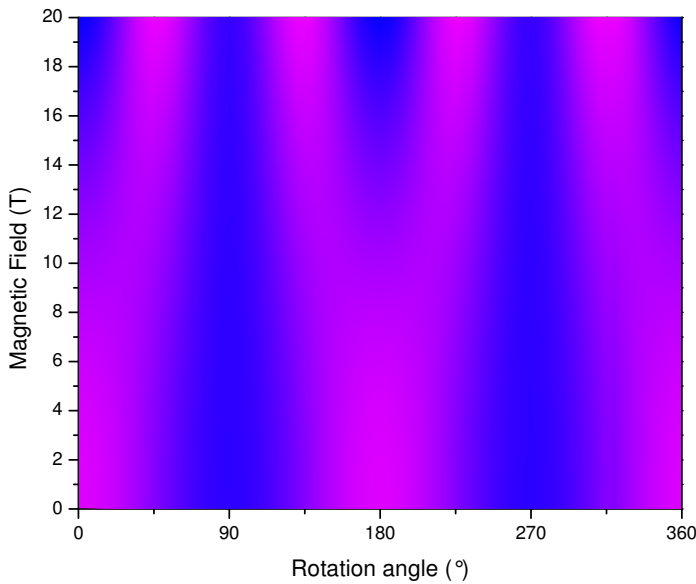


Fig. 6.16: 3D plot of the linear polarization ρ_0^l as function of rotation angle α and magnetic field B for $T = 20$ K determined from the model. The overall evolution of the optical response is equivalent to the low temperature regime, but the critical field B_C for the sign inversion of the second harmonic amplitude a_2 and the saturation field are shifted to noticeably higher magnetic fields.

While this is a quantitative shortcoming, it does not at all spoil a further remarkable observation. Not only does the sign reversal of the second harmonic spherical amplitude disappear at higher temperatures, when carefully looking into the magnetic field dependence of a_2 for different temperatures it also becomes clear that the critical field B_C at which the crossover occurs is increasing with temperature. When then closely examining the model calculations for $T = 10$ K displayed in Fig. 6.14b it appears that the crossover of a_2 is just shifted above 4 T.

At first thought this is highly counter-intuitive as detailed by the following considerations. The above analysis clearly demonstrated that the disappearance of the second spherical harmonic signal corresponds to the optical polarization signal expected for highly symmetric (i. e. $\geq D_{2d}$) QDs. In such QDs the exchange induced finestructure splitting vanishes, which as a consequence restores the fully entangled biexciton-exciton cascade. In parallel work Stevenson *et al.* reported the direct observation of such a transverse magnetic field induced detuning of the finestructure by μ -PL in InAs/GaAs QDs [Ste06c]. Moreover, recall neither the exchange splittings nor the g-factors, which are the ingredients of the Hamiltonian in Eq. 6.32, exhibit a temperature dependence to first order. Thus, whatever critical field B_C one observes at low temperatures, in this picture it should persist to high temperatures (until eventually the thermal activation of QD excitons comes into effect).

This is in stark contrast to experimental fact. Beyond that the temperature dependence of the symmetrization of the optical polarization is in agreement with our model calculations. This is most clearly demonstrated by modeling the optical polarization signal at $T = 20$ K, which is the highest temperature with available data, as function of magnetic field up to 20 T. The result can be depicted from Fig. 6.16. The principle evolution of the signal is absolutely equivalent to the low temperature case, i. e. the transverse magnetic field introduces a fourth spherical harmonic contribution and the second harmonic signal experiences a sign change at a critical field B_C . The only noticeable changes are in absolute values of the amplitudes a_2 and a_4 , which rapidly decrease with increasing temperature, and in a steady increase of B_C with increasing T . For $T = 20$ K our model finds $B_C \approx 10$ T.

From the combined observations it can only be concluded that it is the thermal occupation of the exciton states alone that governs the optical polarization behavior. Under the common assumption that the excitonic finestructure is only weakly affected by in-plane magnetic fields (e. g. [Dor03]) this is, however, hard to conceive, because if it was correct, the optical polarization signal observed had to be constant as function of temperature and not depend noticeable on magnetic field.

Yet, previous work on QDs subject to in-plane magnetic fields ignored the low symmetry and its resulting influence on the magnetic field dependent energetic evolution of the exciton states. For a direct inspection of the latter the eigenvalues of our Hamiltonian as function of magnetic field were numerically determined (again, note these are temperature-*independent*). The result is plotted in Fig. 6.17.

In hindsight, it is clear that the assumption of negligible influence of an in-plane magnetic field to the finestructure of excitons confined to QDs of low symmetry is unjustified and has to be revised. Moreover, the picture is now entirely conclusive. The different degrees of polarization observed for different temperatures are solely given by the thermal occupation of the four optical active exciton states. The intrinsic optical polarization degrees of the individual levels themselves depend on fixed phase relations of the electron and the hole confined to the QD that are induced by the symmetry of the confining poten-

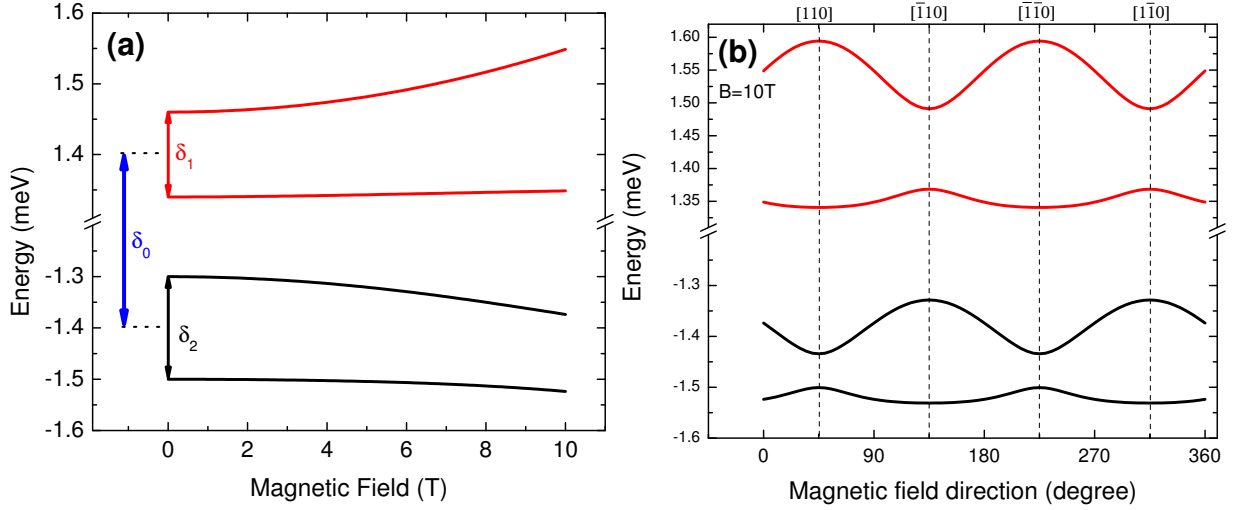


Fig. 6.17: (a) Eigenergies of the four HH-exciton states as calculated by our model Hamiltonian (Eq. 6.32) versus magnetic field substituting the best fit parameters to our data, with magnetic field aligned along the [100] crystal axis. For $B=0$ energetically positive transitions (red lines) correspond to the bright exciton states whereas the negative transitions (black lines) label the dark exciton states (see Fig. 3.6). Indicated are the e-h induced exchange splittings between the bright and dark exciton states (blue), the bright-bright (red) and dark-dark (black) splitting in the absence of magnetic fields. The energy shift is given with respect to the non exchange-split exciton ground state energy. (b) Respective eigenenergies as calculated in (a) for a fixed magnetic field $B=10\text{T}$ as function of magnetic field direction relative to crystal axes orientation. Note that at not point in (a) and (b) any two exciton levels undergo a crossing.

tial, whereby the *inner* and the *outer* states always maintain a relative phase difference of almost exactly 90° . For the total degree of linear polarization in the luminescence signal this means that the fourth spherical harmonic contributions of all four states always add up, but for the second spherical harmonic component the contributions of the inner and outer states always have opposite sign and therefore only the difference between those is measured.

As the magnetic field is now ramped up the occupation is changed in favor of the energetically lower former dark states until at some critical field B_C the population of the inner and the outer states is equal, at which point a_2 necessarily becomes zero and consequently experiences a sign change as the field is further increased. Ultimately, at high fields virtually only the two lowest energetic former dark states will be occupied. For the fields in which the experiments were conducted the change in δ_2 is much smaller than the change in the energetic spacing of the former dark and bright states, which explains the appearance of a saturation regime. At no point in this process do the bright states undergo a crossing. This result is of very high relevance, as it basically states that one can observe a symmetrization of the optical polarization signal of asymmetric QDs **without** restoring the degeneracy of the exciton-biexciton cascade. We shall therefore conclude by setting the above results into context with recent work on the matter and discussing flaws

and possible improvements of the model used throughout this chapter.

6.2.4 Conclusions

We conclude by first discussing the possible contributions arising from the mixing of heavy (HH) and light (LH) holes. First, it modifies the coefficients q_1 and q_2 [Pik94], which are dealt with in Eqs. (6.26), (6.28) and (6.32). Second, it directly affects the polarization of the optical transitions as the hole wavefunction is now written in the form $|\pm\frac{3}{2}hh\rangle + \beta|\mp\frac{1}{2}lh\rangle$. It was shown on the basis of a pseudospin formalism that the light-holes give rise to a zeroth harmonic component instead of a fourth one. In the samples studied in our work the zeroth harmonic appeared to be weak, and therefore the contribution of the light-hole band to the exciton eigenfunctions was neglected. This may explain some discrepancy of the calculated a_0 with the data in Fig. 6.11. We also note that the heavy-light hole mixing gives rise to a linear dichroism of the QDs, $\tilde{\rho}$, which is independent on temperature (see Section 3.2). For $\tilde{\rho} \ll 1$ this contribution is additive to Eq. (6.34) and thus can be considered phenomenologically. However, based on the present experimental data we cannot distinguish between the contributions of the built-in linear polarization arising from the anisotropic exchange splitting δ_1 and the linear dichroism. In general, we are able to fit them with a reasonable value of $\tilde{\rho}$, but for sake of simplicity the presented calculations are obtained with $\tilde{\rho} = 0$. Further work may however built on the fact that different microscopic mechanisms will lead to a distinguishable magnetic field response for the HH-LH mixing. In particular, effects induced by alloy disorder could be separated from the influence of the symmetry reduction as introduced by the heterointerfaces [Pik94] or inhomogeneous strain [Lég07]. Such an experiment would provide valuable input for a comprehensive theoretical description of QDs. It may further be an important step towards a conclusive understanding of the importance of the HH-LH mixing in different material systems, as there is no apparent trend visible in the literature as of now.

Summarizing, we have observed an anomalous behavior of the in-plane magneto-optic anisotropy in CdSe/ZnSe QDs, in that the second and fourth spherical harmonics of the response dominate over the classical zeroth order response. We demonstrated the existence of a compensating magnetic field, leading to a symmetry enhancement of QD optical response. This symmetry enhancement does however not stem from a restoration of the full symmetry of the bright exciton states as expected for QDs of D_{2d} symmetry in the absence of external fields, but instead arises from the thermal population of the resulting four optically active heavily mixed bright-dark exciton states.

This is highly relevant, as in the most general case the four transitions are not at all entangled if invoked in the decay path of biexcitons. Even if two of the optically active states were to cross at some given magnetic field, which may be the case for different values of the coefficients q_1 and q_2 in Eqs. (6.26), this would not automatically result in a non-classical decay path. For a true symmetrization of the biexciton cascade essentially all contributions to an asymmetric response have to cancel out, including a possible

admixture of LH states. Obviously, as demonstrated by the temperature dependence of magneto-optical anisotropy, this is not the case.

As a closing remark we highlight that the physics responsible for our findings are not limited to QDs, but can be applied to other heterostructures of the same symmetry where the heavy-hole exciton is the ground state.

Chapter 7

Conclusions and Outlook

This *Thesis* investigated the interplay of the symmetry and the optical anisotropy in small, strongly confining self-assembled epitaxial CdSe/ZnSe QDs that form by deposition of a single monolayer of CdSe. Extensive PL and PLE measurements in combination with morphological studies demonstrate that these QDs are effectively formed by Cd-rich inclusions in a Zn-rich ternary ZnCdSe alloy and confine exactly one excitonic state, which may however exhibit finestructure as a result of the electron-hole exchange interaction. These excitons have an average activation energy E_A of ~ 90 meV, which is limited by the existence of quasi-2D ZnCdSe platelets of reduced Cd-content with respect to the QDs, that moreover energetically interconnect sub-ensembles of QDs in the QD forming layer. In total, this type of QDs is confining excitons robustly to above liquid nitrogen temperature ($T=77$ K), with this value being determined by both the activation energy E_A and the radiative lifetime to non radiative scattering rate ratio.

The data on the exciton-phonon interaction suggest a complete breakdown of k - conservation in shallow CdSe/ZnSe QDs. The leakage of the exciton wavefunction into the ZnSe barrier then leads to the interaction with a continuum of accessible states for the hot excitons excited above the ZnSe, which explains fast and efficient exciton capture by the QDs. This result is of high relevance for the understanding of energy relaxation in epitaxial QDs, as it presents an alternative fast channel other than Auger-like processes mediated by Coulomb scattering, which are incapable of explaining efficient relaxation of holes in QDs. It is therefore understood, why there is no phonon-bottleneck in the QDs under investigation, which is consistent with but was not generally understood in previous work on QDs of this material system.

Angle-resolved polarization-sensitive photoluminescence spectroscopy is demonstrated to be a versatile tool for the analysis of the interplay of QD symmetry and the resultant optical anisotropy. The method is capable of restoring the otherwise hidden symmetry of the individual QD alignment within an inhomogeneously distributed QD ensemble *after* capping, which may add substantially to the understanding of the actual growth/capping mechanisms. Given the experimental challenges of alignment may be overcome this method will further be capable of fully characterizing the QD potential geometry of a

single QD. In this manifestation it will be able to provide the necessary input for a robust theoretical description of QD electronic and optical properties.

The method was applied to demonstrate efficient circular-to-linear and linear-to-circular optical polarization conversion in QDs in the absence of external fields. Using a pseudospin model it was evidenced that the conversion arises from the electron-hole exchange induced finestructure splitting of the excitonic ground state and essentially represents the steady-state equivalent of quantum beats between these states in the time domain. For QDs with an exchange splitting $\hbar\Omega$ on the order of some μeV the conversion efficiency can take a maximum value of 50 %. This result may be interesting for technological application in several ways. It could be conceived to use QDs as polarization converters in nanoscaled planar waveguides, adding additional functionality to highly integrated all-optical device schemes. This is ever more so interesting as it is possible to change the conversion properties by charging additional carriers into the QDs. With e. g. an extra electron the total spin state of the electrons adds up to zero and consequently the e-h exchange interaction vanishes, which results in cancellation of the optical polarization conversion by the QD. Using an electrical gate to intentionally charge or deplete individual QDs, it may therefore be possible to control the *optical* properties of a nanoscaled QD-based device *electrically*.

In the last part of the *Thesis* angle-resolved polarization-sensitive photoluminescence spectroscopy was applied to QDs subject to an in-plane magnetic field. The observed complex optical polarization behavior was shown to be separable into two contributions whose main optical axis either rotate in opposite direction to that of the magnetic field or remain fixed to [110] crystalline direction. In a qualitative analysis based on the exciton pseudospin hamiltonian it was proven that this behavior was caused by fixed phase relations between the four optical active states, which are introduced by the isotropic and anisotropic contributions of the heavy-hole Zeeman term. Integrating over the ensemble the data suggested that these contributions might be capable of compensating the intrinsic uniaxial anisotropy of shape asymmetric QDs and thereby symmetrize the exciton-biexciton cascade. For a comprehensive quantitative analysis the optical properties of asymmetric QDs subject to an in-plane magnetic field were calculated numerically on the basis of the full heavy-hole exciton \mathbf{k},\mathbf{p} -Hamiltonian. This model succeeds in describing all low temperature data quantitatively with a single set of parameters. From this model it is clearly seen that a optical response characteristic for high symmetry QDs may be obtained from an ensemble of asymmetric QDs *without* a crossing of the zero-field bright exciton states. This observation arises solely from thermal population and exciton relaxation along all four optically active states. As such it does not restore the exciton-biexciton cascade. It is moreover clear, that any logic scheme based on the exciton decay in QDs subject to in-plane magnetic fields has to consider four as opposed to only two optically active transitions in the absence of fields. This significantly alters the properties of the exciton-biexciton cascade in magnetic fields which is at the heart of entanglement based studies on QDs. Models that do not take the above result into account can therefore

not be a priori expected to provide reliable results on excitonic Bell states, which explains major disagreement on recent entanglement studies [Ste06b, Lin06, Gil07].

The model used to describe the magneto-optical anisotropy is moreover not limited to QDs, but can be applied to other heterostructures of the same symmetry in which the heavy-hole exciton is the ground state, as it solely builds on symmetry considerations. A logical expansion of the model would further be the incorporation of the heavy and light hole mixing. This is particularly interesting towards a comprehensive theoretical description of the optical properties of QDs, as it can provide access to different microscopic symmetry reducing mechanism such as alloy disorder, inhomogeneous strain and heterointerfaces, all of which have a distinct behaviour in magnetic fields. Quantitative knowledge of these contributions would provide valuable information on the peculiarities of different QD forming material systems, which show distinctly different influence of the valence band mixing on their optical properties. It must finally be considered a prerequisite for the application of QDs as the fundamental building block in non-classical light sources.

Appendix A

Setup and experimental methods

A.1 Experimental setup

The setup used for all experiments in this work is displayed in Fig. A.1.

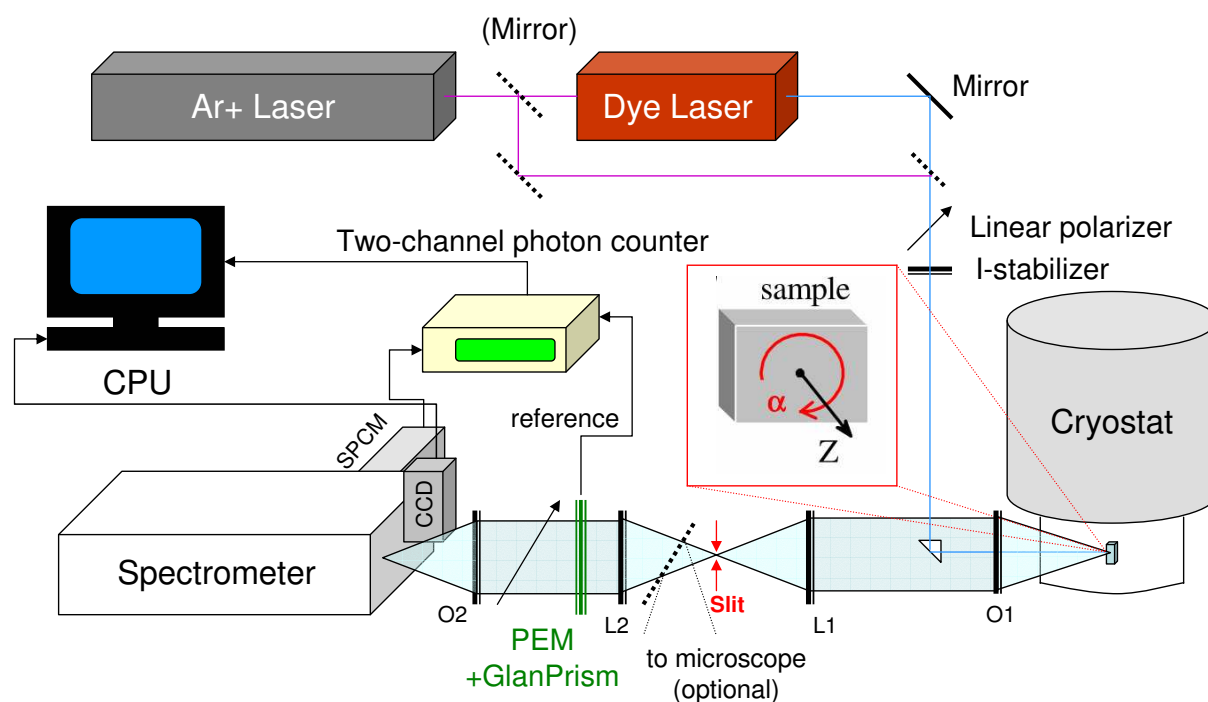


Fig. A.1: Scheme of the polarization resolved photoluminescence and photoluminescence excitation setup.

The optical excitation is provided by an Ar-Ion laser (Coherent Innova 400), which can be operated either in ultra-violet multiple line (UVML) or visible multiple line (MLVIS) mode, thus delivering laser light in the 350-355 nm or 488-516 nm spectral region, respectively. Where required the Ar-Ion laser is used as pump laser for dye lasers (Coherent CR599), which can be configured with a variety of dyes, that in principle allow for continuous tuning of the laser light through the complete visible spectrum (420-750nm). The

high decay rate of the Coumarin dyes, however, which operate in the 480-550 nm spectral region, inflicts serious limitations on long term measurements requiring green excitation.

The exiting light is then passed through a high quality Glan-Thompson linear polarizer and subsequently through an intensity stabilizer unit (ThorLabs CR200A) to ensure highly pure and stable excitation. Where required quarter wave-plates or a Soleil-Babinet compensator were used to prepare circularly polarized excitation after deflecting the beam on a right angle prism into the cryostat. The laser is then focussed by 75 mm diameter plano-convex lens with 250 mm focal length (labelled O1 in Fig. A.1) onto the sample inside of the cryostat, focussing the laser to a spot size of about $\sim 100 \mu\text{m}$. The latter is limited by the distance of 230 mm from the outer cryostat windows to the sample.

The sample itself is mounted on a rotating holder inside a glass pin in the center of the cryostat, enabling measurements from 1.6 K (sample immersed in superfluid helium) up to room temperature. The rotating holder is set up such that it allows for rotations around the axis of the incident light (defined z-axis), i. e. the plane of rotation is perpendicular to the axis of incidence. The holder is externally controlled by a stepping motor (Nanotec ST5709S1208-A) that enables positioning of the sample with an accuracy of 0.1° . The helium bath cryostat (Thor Research Instruments) is equipped with superconducting NbTi split-coil magnet, which is capable of ramping magnetic fields up to $B = 7 \text{ T}$ and can be set up in both Faraday and Voigt geometry.

The isotropically emitted photoluminescence signal (PL) is then again picked up from the sample by lens O1 and further passed on to lens L1, where it is focussed again onto an adjustable x-y mechanical slit. The purpose of this mechanical slit is twofold. For one it enables spatial selection of the area on the sample from which the PL signal is detected. The exact position on the sample can be monitored by an microscope upon inserting an optional mirror into the beampath. The slit further serves as an effective filter of scattered light coming from the various optical elements. After the mechanical slit the PL signal is picked up again by lens L2. Lenses L1 and L2 are of identical design with the appropriate anti-reflection coating of the corresponding wavelength (i. e. of the PL signal) to minimize signal loss on the optical elements.

The PL signal is then passed through the photo-elastic modulator (Hinds Instruments I/FS50) / Glan Prism assembly, which is the key ingredient of the high optical polarization sensitivity of the setup (see section A.2) and finally picked up by the objective O2, from which the signal is focussed onto the spectrometer entrance slit. The single spectrometer (Jobin-Yvon HR1000), which has a focal length of one meter and was operated with a blazed holographic 1200 mm^{-1} grating in all experiments presented in this work, disperses the signal either on multi-channel liquid nitrogen cooled CCD camera (Princeton Instruments CCD-1100-PF/UV) or on a single channel avalanche photo-diode single photon counting module (Perkin Elmer SPCM-AQR-17). The latter is connected to a two channel photcounter referenced by the modulation frequency of the PEM, which is either 50 or 100 kHz (see below). Finally, the signal is recorded by the central computer.

The setup is fully automatized and can be completely controlled hands-off from the

computer once the optics are properly aligned. This is highly beneficial in long term measurements, where high system stability is required, and thus enables a high data volume feedthrough. Moreover, this allows on-the-fly analysis of the recorded data by passing on the raw data to a second computer, where they are further processed.

A.2 Optical polarization modulation spectroscopy

The high polarization sensitivity of the setup is provided by the application of a photo-elastic modulator (PEM) / Glan Prism assembly as optical polarization analyzer. The optically active element of the PEM is a fused-silica element, that is periodically compressed and stretched by an ac-driven piezoelectric quartz transducer at a frequency of $f = 50$ kHz. Exploiting the photo-elastic effect, the oscillating strain is accompanied by an oscillating induced birefringence, which gives rise to a time-dependent phase shift in the linear optical polarization component parallel to the fast axis of the modulator. For technical reasons the modulation occurs in the form of a sine-function. Whereas the modulation frequency is fixed by design, the phase shift is adjustable and referred to as retardation. Depending on the magnitude of the set retardation, different polarization components are probed by a linear polarizer at 45° with respect to the fast axis of the PEM, as depicted by Fig. A.2.

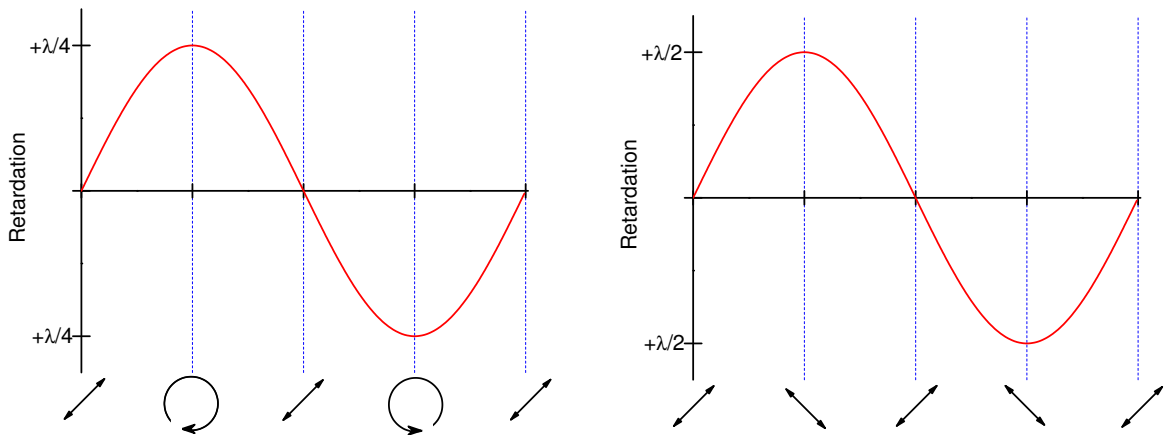


Fig. A.2: Operation principle of the photo-elastic modulator (PEM): While the linear optical polarization component parallel to the PEM slow axis passes unaffected through the device, the component parallel to the PEM fast axis experiences a time-dependent phase shift. Different scenarios are realized for linearly polarized light incident under 45° to the PEM fast axis depending on the set retardation. For quarter wave retardation (left panel) the polarization is modulated between right and left circular polarization at the modulator frequency f . For half wave retardation (right panel) the light beam is modulated between two perpendicular, linearly polarized states at the modulator second harmonic $2f$.

The PEM assembly is further mount on a rotation stage, which allows a precise measurement of the Stokes vector components introduced in Chapter 3.1.3. Using the

two-channel photon counter in combination with the highly sensitive SPCM module as detector, the optical polarization state of the PL signal is detected the following way:

At half wave retardation one simultaneously records two mutually perpendicular linear polarization components I_x and I_y upon referencing to the modulator second harmonic $2f$. By analyzing

$$\rho_l = \frac{I_x - I_y}{I_x + I_y} \quad (\text{A.1})$$

hence rotating the PEM assembly by 45° around the optical axis, repeating the measurement for the mutually perpendicular linear polarization intensities I_{x+45° and I_{y+45° and analyzing

$$\rho_{l'} = \frac{I_{x+45^\circ} - I_{y+45^\circ}}{I_{x+45^\circ} + I_{y+45^\circ}} \quad (\text{A.2})$$

one obtains the linear polarization state of the observed optical signal. By additionally recording the circular polarization components I_r and I_l , which are measured by setting the PEM to quarter wave retardation and referencing the two channel photon counter to the modulator frequency f , one obtains

$$\rho_c = \frac{I_r - I_l}{I_r + I_l} \quad (\text{A.3})$$

which together with the above gives the exact optical polarization state of the PL signal in terms of Poincaré sphere coordinates.

The main advantage of modulation detection is the high sensitivity to even very small signals in combination with reasonably short measurement times. In practice, the polarization resolution is limited by the events on the detector n , as

$$\Delta\rho \propto \frac{\sqrt{n}}{n}. \quad (\text{A.4})$$

The overall sensitivity of the setup is further limited by the leakage rate of the polarizers, yielding a minimum value of $\Delta\rho \sim 0.001$.

Appendix B

Angular Momentum Operators

In this appendix we shall give the Angular Momentum Operator explicitly. For the representation $D_{3/2}$ in the basis $Y_m^{3/2}; m = 3/2, 1/2, -1/2, -3/2$ (canonical basis) we find the matrices $J_i (i = x, y, z)$

$$J_x = \begin{pmatrix} 0 & \sqrt{3}/2 & 0 & 0 \\ \sqrt{3}/2 & 0 & 1 & 0 \\ 0 & 1 & 0 & \sqrt{3}/2 \\ 0 & 0 & \sqrt{3}/2 & 0 \end{pmatrix} \quad (\text{B.1})$$

$$J_y = \begin{pmatrix} 0 & -i\sqrt{3}/2 & 0 & 0 \\ i\sqrt{3}/2 & 0 & -i & 0 \\ 0 & i & 0 & -i\sqrt{3}/2 \\ 0 & 0 & i\sqrt{3}/2 & 0 \end{pmatrix} \quad (\text{B.2})$$

$$J_z = \begin{pmatrix} 3/2 & 0 & 0 & 0 \\ 0 & 1/2 & 0 & 0 \\ 0 & 0 & -1/2 & 0 \\ 0 & 0 & 0 & -3/2 \end{pmatrix} \quad (\text{B.3})$$

Accordingly, we find their products to the second power

$$J_x^2 = \begin{pmatrix} 3/4 & 0 & \sqrt{3}/2 & 0 \\ 0 & 7/4 & 0 & \sqrt{3}/2 \\ \sqrt{3}/2 & 0 & 7/4 & 0 \\ 0 & \sqrt{3}/2 & 0 & 3/4 \end{pmatrix} \quad (\text{B.4})$$

$$J_y^2 = \begin{pmatrix} 3/4 & 0 & -\sqrt{3}/2 & 0 \\ 0 & 7/4 & 0 & -\sqrt{3}/2 \\ -\sqrt{3}/2 & 0 & 7/4 & 0 \\ 0 & -\sqrt{3}/2 & 0 & 3/4 \end{pmatrix} \quad (\text{B.5})$$

$$J_z^2 = \begin{pmatrix} 9/4 & 0 & 0 & 0 \\ 0 & 1/4 & 0 & 0 \\ 0 & 0 & 1/4 & 0 \\ 0 & 0 & 0 & 9/4 \end{pmatrix} \quad (\text{B.6})$$

And the products to the third power

$$J_x^3 = \begin{pmatrix} 0 & 7\sqrt{3}/8 & 0 & 3/4 \\ 7\sqrt{3}/8 & 0 & 5/2 & 0 \\ 0 & 5/2 & 0 & 7\sqrt{3}/8 \\ 3/4 & 0 & 7\sqrt{3}/2 & 0 \end{pmatrix} \quad (\text{B.7})$$

$$J_y^3 = \begin{pmatrix} 0 & -i7\sqrt{3}/8 & 0 & i3/4 \\ i7\sqrt{3}/8 & 0 & -i5/2 & 0 \\ 0 & i5/2 & 0 & -i7\sqrt{3}/8 \\ -i3/4 & 0 & i7\sqrt{3}/2 & 0 \end{pmatrix} \quad (\text{B.8})$$

$$J_z^3 = \begin{pmatrix} 27/8 & 0 & 0 & 0 \\ 0 & 1/8 & 0 & 0 \\ 0 & 0 & -1/8 & 0 \\ 0 & 0 & 0 & -27/8 \end{pmatrix} \quad (\text{B.9})$$

Appendix C

List of Abbreviations

- AFM - Atomic Force Microscope
- CB - Conduction Band
- CMM - Continuum Mechanical Model
- CW - Continuous Wave (excitation)
- EBOM - Empirical Bond Orbital Model
- EMA - Effective Mass Approximation
- ETB - Empirical Tight Binding (method)
- FCC - Face Centered Cubic
- FSS - Fine Structure Splitting
- FWHM - Full Width at Half Maximum
- HH - Heavy Hole (band)
- HRTEM - High Resolution Transmission Electron Microscope
- LDA - Local Density Approximation
- LA - Longitudinal Acoustic (phonon)
- LH - Light Hole (band)
- LO - Longitudinal Optical (phonon)
- MBE - Molecular Beam Epitaxy
- ML - MonoLayer
- MLVIS - Multiple Line VISible
- MOCVD - Metal Organic Chemical Vapor Deposition
- NC - NanoCrystal

PEM - Photo-Elastic Modulator

PL - PhotoLuminescence

PLE - PhotoLuminescence Excitation

QCL - Quantum Cascade Laser

QDs - Quantum Dots

QW - Quantum Well

QWr - Quantum Wire

RHEED - Reflection High Energy Electron Diffraction

SO - Splitt-Off (band)

SPCM - Single Photon Counting Module

UHV - Ultra High Vacuum

UVML - Ultra-Violett Multiple Line

VB - Valence Band

VFF - Valence Force Field (model)

Bibliography

- [Aki05] I. A. Akimov, K. V. Kavokin, A. Hundt and F. Henneberger. Phys. Rev. B **71**, 075326 (2005).
- [Ako06] N. Akopian, N. H. Lindner, E. Poem, Y. Berlatzky, J. Avron, D. Gershoni, B. D. Gerardot and P. M. Petroff. Phys. Rev. Lett. **96**, 130501 (2006).
- [Ara82] Y. Arakawa and H. Sakaki. Appl. Phys. Lett. **40**, 939 (1982).
- [Asa86] M. Asada, Y. Mayamoto and Y. Suematsu. IEEE J. Quantum Electron. **QE-22**, 1915 (1986).
- [Ash76] N. W. Ashcroft and N. D. Mermin. *Solid State Physics* (Thomson Learning, Inc., 1976).
- [Asp81] A. Aspect, P. Grangier and G. Roger. Phys. Rev. Lett. **47**, 460 (1981).
- [Ast02] G. V. Astakhov, V. P. Kochereshko, D. R. Yakovlev, W. Ossau, J. Nürnberger, W. Faschinger, G. Landwehr, T. Wojtowicz, G. Karczewski, and J. Kossut. Phys. Rev. B **65**, 115310 (2002).
- [Azz87] R. M. A. Azzam and N. M. Bashra. *Ellipsometry and Polarized Light* (North Holland Physics Publishing, Amsterdam, 1987).
- [Bac91] G. Bacher, H. Schweizer, J. Kovac, A. Forchel, H. Nickel, W. Schlapp and R. Lösch. Phys. Rev. B **43**, 9312 (1991).
- [Bas88] G. Bastard. *Wave mechanics applied to semiconductor heterostructures* (Les Editions de Physique, Les Ulis, 1988).
- [Bay02] M. Bayer, G. Ortner, O. Stern, A. Kuther, A. A. Gorbunov, A. Forchel, P. Hawrylak, S. Fafard, K. Hinzer, T. L. Reinecke, S. N. Walck, J. P. Reithmaier, F. Klopff and F. Schäfer. Phys. Rev. B **65**, 195315 (2002).
- [Ben00] O. Benson, C. Santori, M. Pelton and Y. Yamamoto. Phys. Rev. Lett. **84**, 2513 (2000).
- [Bes03] G. Bester, S. Nair and A. Zunger. Phys. Rev. B **67**, R161306 (2003).
- [Bes06] G. Bester, X. Wu, D. Vanderbilt and A. Zunger. Phys. Rev. Lett. **96**, 187602 (2006).

- [Bes07] G. Bester, D. Reuter, L. He, A. Zunger, P. Kailuweit, A. D. Wieck, U. Zeitler, J. C. Maan, O. Wibbelhoff and A. Lorke. *Phys. Rev. B* **76**, 075338 (2007).
- [Bim99] D. Bimberg, M. Grundmann and N. N. Ledentsov. *Quantum Dot Heterostructures* (John Wiley & Sons, Chichester, 1999).
- [Bir74] G. L. Bir and G. E. Pikus. *Symmetry and strain-induced effects in semiconductors* (John Wiley & Sons, New York, 1974).
- [Bla94] E. Blackwood, M. J. Snelling, R. T. Harley, S. R. Andrews and C. T. B. Foxon. *Phys. Rev. B* **50**, 14246 (1994).
- [Blo28] F. Bloch. *Z. Physik* **52**, 555 (1928).
- [Boc90] U. Bockelmann and G. Bastard. *Phys. Rev. B* **42**, 8947 (1990).
- [Boc92a] U. Bockelmann and G. Bastard. *Phys. Rev. B* **45**, 1688 (1992).
- [Boc92b] U. Bockelmann and T. Egeler. *Phys. Rev. B* **46**, 15574 (1992).
- [Boc97] U. Bockelmann, W. Heller, A. Filoramo and P. Roussignol. *Phys. Rev. B* **55**, 4456 (1997).
- [Bri97] W. F. Brinkman, D. E. Haggan and W. W. Troutman. *IEEE J. Solid-State Circuits* **32**, 1858 (1997).
- [Bru91] L. Brus. *Appl. Phys. A* **53**, 465 (1991).
- [Bry88] G. W. Bryant. *Phys. Rev. B* **37**, 8763 (1988).
- [Bry01] G. W. Bryant and W. Jaskólski. *Physica E* **11**, 72 (2001).
- [Cha88] Y.-C. Chang. *Phys. Rev. B* **37**, 8215 (1988).
- [Cha99] S. A. Chaparro, J. Drucker, Y. Zhang, D. Chandrasekhar, M. R. McCartney and D. J. Smith. *Phys. Rev. Lett.* **83**, 1199 (1999).
- [Coo07] R. R. Cooney, S. L. Sewall, K. E. H. Anderson, E. A. Dias and P. Kambhampati. *Phys. Rev. Lett.* **98**, 177403 (2007).
- [Dor03] P. S. Dorozhkin, A. V. Chernenko, V. D. Kulakovskii, A. S. Brichkin, A. A. Maksimov, H. Schoemig, G. Bacher, A. Forchel, S. Lee, M. Dobrowolska and J. K. Furdyna. *Phys. Rev. B* **68**, 195313 (2003).
- [Dre55] G. Dresselhaus. *Phys. Rev.* **100**, 580 (1955).
- [Dzh97] R. I. Dzhioev, H. M. Gibbs, E. L. Ivchenko, G. Khitrova, V. L. Korenev, M. N. Tkachuk and B. P. Zakharchenya. *Phys. Rev. B* **56**, 13405 (1997).
- [Edi07] M. Ediger, G. Bester, A. Badolato, P. M. Petroff, K. Karrai, A. Zunger and R. J. Warburton. *Nature Physics* **3**, 773 (2007).

-
- [Efr95] A. L. Efros, V. A. Kharchenko and M. Rosen. *Solid State Commun.* **93**, 281 (1995).
- [Eki85] A. I. Ekimov and A. A. Onushchenko. *JETP Lett.* **40**, 1136 (1985).
- [Fai94] J. Faist, F. Capasso, D. Sivco, C. Sirtori, A. Hutchinson and A. Cho. *Science* **264**, 553 (1994).
- [Fie04] R. Fiederling. *Elektrische Spininjektion in GaAs LEDs*. Dissertation, University of Würzburg (2004).
- [Fin02] J. J. Finley, D. J. Mowbray, M. S. Skolnick, A. D. Ashmore, C. Baker, A. F. G. Monte and M. Hopkinson. *Phys. Rev. B* **66**, 153316 (2002).
- [Fli01] T. Flissikowski, A. Hundt, M. Lowisch, M. Rabe and F. Henneberger. *Phys. Rev. Lett.* **86**, 3172 (2001).
- [Fli03] T. Flissikowski, I. A. Akimov, A. Hundt and F. Henneberger. *Phys. Rev. B* **68**, 161309(R) (2003).
- [Fox06] M. Fox. *Quantum Optics: an introduction* (Oxford University Press, Oxford, 2006).
- [Fra97] A. Franceschetti and A. Zunger. *Phys. Rev. Lett.* **78**, 915 (1997).
- [Fu97] H. Fu, L. Wang and A. Zunger. *Appl. Phys. Lett.* **71**, 3433 (1997).
- [Fu99] H. Fu, L. Wang and A. Zunger. *Phys. Rev. B* **59**, 5568 (1999).
- [Fuj00] M. Fujii, D. Kovalev, J. Diener, F. Koch, S. Takeoka and S. Hayashi. *J. Appl. Phys.* **88**, 5772 (2000).
- [Fuk91] T. Fukui, S. Ando and Y. Tokura. *Appl. Phys. Lett.* **58**, 2018 (1991).
- [Fur06] M. Furis, H. Htoon, M. A. Petruska, V. I. Klimov, T. Barrick and S. A. Crooker. *Phys. Rev. B* **73**, 241313R (2006).
- [Gam96] D. Gammon, E. S. Snow, B. V. Shanabrook and D. Park. *Phys. Rev. Lett.* **76**, 3005 (1996).
- [Ger07] B. D. Gerardot, S. Seidl, P. A. Dalgarno, R. J. Warburton, D. Granados, J. M. Garcia, K. Kowalik, O. Krebs, K. Karrai, A. Badolato and P. M. Petroff. *Appl. Phys. Lett.* **90**, 041101 (2007).
- [Gil07] A. Gilchrist, K. J. Resch and A. G. White. *Nature* **445**, E4 (2007).
- [Gou06] S. V. Goupalov. *Phys. Rev. B* **74**, 113305 (2006).
- [Gru02] M. Grundmann(Ed.). *Nano-Optoelectronics* (Springer-Verlag Berlin Heidelberg, 2002).

- [Guo97] S. P. Guo, H. Ohno, A. Shen, F. Matsukura and Y. Ohno. Appl. Phys. Lett. **70**, 2738 (1997).
- [Hýt98] M. J. Hýtch, E. Snoeck and R. Kilaas (1998).
- [Hög04] A. Högele, S. Seidl, M. Kroner, K. Karrai, R. J. Warburton, B. D. Gerardot and P. M. Petroff. Phys. Rev. Lett. **93**, 217401 (2004).
- [HB56] R. Hanbury-Brown and R. Q. Twiss. Nature **177**, 27 (1956).
- [He05] L. He, G. Bester and A. Zunger. Phys. Rev. Lett. **95**, 246804 (2005).
- [He06] L. He and A. Zunger. Phys. Rev. B **73**, 115324 (2006).
- [Hei01] R. Heitz, H. Born, F. Guffarth, O. Stier, A. Schliwa, A. Hoffmann and D. Bimberg. Phys. Rev. B **64**, 241305(R) (2001).
- [Hen71] B. Hennion, F. Moussa, G. Pepy and K. Kunc. Phys. Lett. **36A**, 376 (1971).
- [Her99] M. A. Hermann and H. Sitter. *Molecular Beam Epitaxy* (Springer Verlag Berlin Heidelberg, 1999).
- [Hto08] H. Htoon, M. Furis, S. A. Crooker, S. Jeong and V. I. Klimov. Phys. Rev. B **77**, 035328 (2008).
- [Ino97] T. Inoshita and H. Sakaki. Phys. Rev. B **56**, R4355 (1997).
- [Iva98] S. Ivanov, S. Sorokin, I. Krestnikov, N. Fleev, B. Ber, I. Sedova, Y. Kudryavtsev and P. Kop'ev. J. Cryst. Growth **184/185**, 70 (1998).
- [Ivc91] E. L. Ivchenko, V. P. Kochereshko, A. Y. Naumov, I. N. Uraltsev and P. Lavalard. Superlattices Microstruct. **10**, 497 (1991).
- [Ivc95] E. L. Ivchenko and G. E. Pikus. *Superlattices and Other Heterostructures* (Springer-Verlag Berlin Heidelberg, 1995).
- [Jac98] L. Jacak, P. Hawrylak and A. Wójs. *Quantum Dots* (Springer Verlag Berlin Heidelberg, 1998).
- [Jas03] L. Jasak, P. Machnikowski, J. Krasnyi and R. Zöller. Eur. Phys. J. D **22**, 319 (2003).
- [Joh08] R. Johne, N. A. Gippius, G. Pavlovic, D. D. Slohnyshkov, I. A. Shelykh and G. Malpuech. Phys. Rev. Lett. **100**, 240404 (2008).
- [Joy98] P. B. Joyce, T. J. Krzyzewski, G. R. Bell, B. A. Joyce and T. S. Jones. Phys. Rev. B **52**, R15981 (1998).
- [Kör08] M. Kördel. *Raman-spektroskopische Untersuchungen an II-VI Mischkristallen und -Quantenpunkten*. Diplomarbeit, University of Würzburg (2008).

-
- [Kan57] E. O. Kane. *J. Phys. Chem. Solids* **1**, 249 (1957).
- [Kan66] E. O. Kane. *Semiconductors and Semimetals*, Band 1 (Academic Press, New York, 1966). Edited by R. K. Willardson and A. C. Beer.
- [Kar99] G. Karczewski, S. Mackowski, M. Kutrowski, T. Wojtowicz and J. Kossut. *Appl. Phys. Lett.* **74**, 3011 (1999).
- [Kav03] K. V. Kavokin. *phys. stat. sol. (a)* **195**, 592 (2003).
- [Kaz71] R. Kazarinov and R. Suris. *Sov. Phys. Semicond.* **5**, 707 (1971).
- [Kea66] P. N. Keating. *Phys. Rev.* **145**, 637 (1966).
- [Kel62] L. V. Keldysh. *Sov. Phys. Solid State* **4**, 1658 (1962).
- [Kim94] Y. D. Kim, M. V. Klein, S. F. Ren, Y. C. Chang, H. Luo, N. Samarth and J. K. Furdyna. *Phys. Rev. B* **49**, 7262 (1994).
- [Kli99] V. I. Klimov, D. W. McBranch, C. A. Leatherdale and M. G. Bawendi. *Phys. Rev. B* **60**, 13740 (1999).
- [Kli00] V. I. Klimov, A. A. Mikhailovsky, D. W. McBranch, C. A. Leatherdale and M. G. Bawendi. *Phys. Rev. B* **61**, R13349 (2000).
- [Kli05] C. Klingshirn. *Semiconductor Optics* (Springer-Verlag Berlin Heidelberg, 2005).
- [Koc67] C. A. Kocher and E. D. Commins. *Phys. Rev. Lett.* **18**, 575 (1967).
- [Koh65] W. Kohn and L. J. Sham. *Phys. Rev.* **140**, A1133 (1965).
- [Kou04] A. V. Koudinov, I. A. Akimov, Y. G. Kusrayev and F. Henneberger. *Phys. Rev. B* **70**, 241305(R) (2004).
- [Kov98] D. Kovalev, H. Heckler, M. Ben-Chorin, G. Polisski, M. Schwartzkopff and F. Koch. *Phys. Rev. Lett.* **81**, 2803 (1998).
- [Kre01] I. L. Krestnikov, N. N. Lendentsov and A. H. D. Bimberg. *phys. stat. sol. (a)* **183**, 207 (2001).
- [Kru07] C. Kruse, M. Gartner, A. Gust and D. Hommel. *Appl. Phys. Lett.* **90**, 221102 (2007).
- [Kus99] Y. G. Kusrayev, A. V. Koudinov, I. G. Aksyanov, B. P. Z. abd T. Wojtowicz, G. Karczewski and J. Kossut. *Phys. Rev. Lett.* **82**, 3176 (1999).
- [Kus05] Y. G. Kusrayev, A. V. Koudinov, B. P. Zakharchenya, S. Lee, J. K. Furdyna and M. Dobrowolska. *Phys. Rev. B* **72**, 155301 (2005).
- [Lég07] Y. Léger, L. Besombes, L. Maingault and H. Mariette. *Phys. Rev. B* **76**, 045331 (2007).

- [Lan04] W. Langbein, P. Borri, U. Woggon, V. Stavarache, D. Reuter and A. D. Wieck. Phys. Rev. B **69**, 161301R (2004).
- [Lee01] S. Lee, L. Jönsson, W. Wilkins, G. W. Bryant and G. Klimeck. Phys. Rev. B **63**, 195318 (2001).
- [Leo97] K. Leonardi, H. Heinke, K. Ohkawa, D. Hommel, H. Selke, F. Gindele and U. Woggon. Appl. Phys. Lett. **71**, 1510 (1997).
- [Li99] X.-Q. Li, H. Nakayama and Y. Arakawa. Phys. Rev. B **59**, 5069 (1999).
- [Li03] X. Li, Y. Wu, D. Steel, D. Gammon, T. H. Stievater, D. S. Katzer, D. Park, C. Piermarocchi and L. J. Sham. Science **301**, 809 (2003).
- [Lin06] N. H. Lindner, J. Avron, N. Akopian and D. Gershoni. quant-ph/0601200 <http://arxiv.org/abs/quant-ph/0601200> (2006).
- [Lom88] G. Lommer, F. Malcher and U. Rössler. Phys. Rev. Lett. **60**, 728 (1988).
- [Los98] D. Loss and D. P. DiVincenzo. Phys. Rev. A **57**, 120 (1998).
- [Low99] M. Lowisch, M. Rabe, F. Kreller and F. Henneberger. Appl. Phys. Lett. **74**, 2489 (1999).
- [Lut56] J. M. Luttinger. Phys. Rev. **102**, 1030 (1956).
- [Mac04] S. Mackowski, T. A. Nguyen, T. Gurung, K. Hewaparakrama, H. E. Jackson, L. M. S. Wrobel, K. Fronc, J. Kossut and G. Karczewski. Phys. Rev. B **70**, 245312 (2004).
- [Mah07a] S. Mahapatra. *Formation and properties of CdSe/ZnSe Quantum Dots*. Dissertation, University of Würzburg (2007).
- [Mah07b] S. Mahapatra, T. Kiessling, E. Margapoti, G. Astakhov, W. Ossau, L. Worschech, A. Forchel and K. Brunner. J. Crystal Growth **301-302**, 310 (2007).
- [Mah07c] S. Mahapatra, T. Kiessling, E. Margapoti, G. V. Astakhov, J. Renner, U. Bass, C. Bougerol, T. Schmidt, A. Bendounan, F. Schmitt, C. Schumacher, L. Worschech, W. Ossau, J. Geurts, L. W. Molenkamp, F. Reinert, A. Forchel and K. Brunner. phys. stat. sol. (c) **4**, 3129 (2007).
- [Mar07] E. Margapoti, L. Worschech, A. Forchel, A. Tribu, T. Aichele, R. André and K. Kheng. Appl. Phys. Lett. **90**, 181927 (2007).
- [Mas02] Y. Masumoto and T. Takagahara(Eds.). *Semiconductor Quantum Dots* (Springer-Verlag Berlin Heidelberg, 2002).
- [Med05] I. L. Medintz, H. T. Uyeda, E. R. Goldman and H. Mattoussi. Nature Mat. **4**, 435 (2005).

-
- [Mei84] F. Meier and B. P. Zakharchenya(Eds.). *Optical Orientation* (North Holland, Amsterdam, 1984).
- [Mic03] P. Michler(Ed.). *Single Quantum Dots* (Springer-Verlag Berlin Heidelberg, 2003).
- [Muk96] K. Mukai, N. Ohtsuka, H. Shoji and M. Sugawara. *Phys. Rev. B* **54**, R5243 (1996).
- [Mur58] M. A. Murray. *Phys. Rev. Lett.* **1**, 450 (1958).
- [Mur93] C. B. Murray, D. J. Norris and M. G. Bawendi. *J. Am. Chem. Soc.* **115**, 8706 (1993).
- [Nas89] A. S. Nasibov, Y. V. Korostelin, P. V. Shapkin, L. G. Suslina, D. L. Fedorov and L. S. Markov. *Solid State Commun.* **71**, 867 (1989).
- [Ngu04] T. A. Nguyen, S. Mackowski, H. E. Jackson, L. M. Smith, J. Wrobel, K. Fronc, G. Karczewski, J. Kossut, M. Dobrowolska, J. K. Furdyna and W. Heiss. *Phys. Rev. B* **70**, 125306 (2004).
- [Ngu07] T. A. Nguyen, S. Mackowski, T. B. Hoang, H. E. Jackson, L. M. Smith and G. Karczewski. *Phys. Rev. B* **76**, 245320 (2007).
- [Nie00] M. A. Nielsen and I. L. Chuang. *Quantum Computation and Quantum Information* (Cambridge University Press, 2000).
- [Nir94] M. Nirmal, C. B. Murray and M. G. Bawendi. *Phys. Rev. B* **50**, 2293 (1994).
- [Ohn96] B. Ohnesorge, M. Albrecht, J. Oshinowo, A. Forchel and Y. Arakawa. *Phys. Rev. B* **54**, 11532 (1996).
- [Pas01] T. Passow, H. Heinke, T. Schmidt, J. Falta, A. Stockmann, H. Selke, P. L. Ryder, K. Leonardi and D. Hommel. *Phys. Rev. B* **64**, 193311 (2001).
- [Pat03] B. Patton, W. Langbein and U. Woggon. *Phys. Rev. B* **68**, 125316 (2003).
- [Per96] A. Peres. *Phys. Rev. Lett.* **77**, 1413 (1996).
- [Per00] N. Peranio, A. Rosenauer, D. Gerthsen, S. V. Sorokin, I. V. Sedova and S. V. Ivanov. *Phys. Rev. B* **61**, 16015 (2000).
- [Pik93] G. E. Pikus and F. G. Pikus. *J. of Lumin.* **54**, 279 (1993).
- [Pik94] G. E. Pikus and F. G. Pikus. *Solid State Commun.* **89**, 319 (1994).
- [Pop04] D. P. Popescu, P. G. Eliseev, A. Stintz and K. J. Malloy. *Semicond. Sci. Technol.* **19**, 33 (2004).
- [Pry97] C. Pryor, M.-E. Pistol and L. Samuelson. *Phys. Rev. B* **56**, 10404 (1997).

- [Pul99] J. Puls, M. Rabe, H.-J. Wünsche and F. Henneberger. Phys. Rev. B **60**, 16303R (1999).
- [Rab98] M. Rabe, M. Lowisch and F. Henneberger. J. Crystal Growth **184-185**, 248 (1998).
- [Ree86] M. A. Reed, R. T. Bate, K. Bradshaw, W. M. Duncan, W. M. Frensley, J. W. Lee and D. H. Smith. J. Vac. Sci. Technol. B **4**, 358 (1986).
- [Reu05] D. Reuter, P. Kailuweit, A. D. Wieck, U. Zeitler, O. Wibbelhoff, C. Meier, A. Lorke and J. C. Maan. Phys. Rev. Lett. **94**, 026808 (2005).
- [Rez02] A. Reznitsky, A. Klochikhin, S. Permogorov, L. Tenishev, I. Sedova, S. Sorokin, S. Ivanov, M. Schmidt, H. Zhao, E. Kurtz, H. Kalt and C. Klingshirn. phys. stat. sol. (b) **229**, 509 (2002).
- [Rho00] H. Rho, L. M. Robinson, L. M. Smith, H. E. Jackson, S. Lee, M. Dobrowolska and J. K. Furdyna. Appl. Phys. Lett. **77**, 1813 (2000).
- [Roc32] H. P. Rocksby. J. Soc. Glass Technol. **16**, 171 (1932).
- [Saa89] A. S. Saada. *Elasticity: Theory and applications* (Robert E. Krieger Publishing Co., Florida, 1989).
- [Sch03a] M. Scheibner, G. Bacher, A. Forchel, T. Passow and D. Hommel. J. of Superconductivity: Incorporating Novel Magnetism **16**, 395 (2003).
- [Sch03b] M. Scheibner, G. Bacher, S. Weber, A. Forchel, T. Passow and D. Hommel. Phys. Rev. B **67**, 153302 (2003).
- [See05] J. Seebeck, T. R. Nielsen, P. Gartner and F. Jahnke. Phys. Rev. B **71**, 125327 (2005).
- [Seg05] R. Seguin, A. Schliwa, S. Rodt, K. Pötschke, U. W. Pohl and D. Bimberg. Phys. Rev. Lett. **95**, 257402 (2005).
- [Sei96] W. Seifert, N. Carlsson, M. Miller, M.-E. Pistol, L. Samuelson and L. R. Wallenberg. Prog. Cryst. Growth Charact. Mater. **33**, 423 (1996).
- [Sem03] Y. G. Semenov and S. M. Ryabchenko. Phys. Rev. B **68**, 045322 (2003).
- [Sho94] A. Shor. *Proceedings of the 35th Annual Symposium on the Foundations of Computer Science* (IEEE Press, Los Alamitos, 1994).
- [Sta00] T. Stauber, R. Zimmermann and H. Castella. Phys. Rev. B **62**, 7336 (2000).
- [Sta03] T. M. Stace, G. J. Milburn and C. H. W. Barnes. Phys. Rev. B **67**, 085317 (2003).

-
- [Ste06a] S. Steen, S. J. McNab, L. Sekaric, I. Babich, J. Patel, J. Bucchignano, M. Rooks, D. M. Fried, A. W. Topol, J. R. Brancaccio, R. Yu, J. M. Hergenrother, J. P. Doyle, R. Nunes, R. G. Viswanathan, S. Purushothaman and M. B. Rothwel. *Microelec. Eng.* **83**, 754 (2006).
- [Ste06b] R. M. Stevenson, R. J. Young, P. Atkinson, K. Cooper, D. A. Ritchie and A. J. Shields. *Nature* **439**, 179 (2006).
- [Ste06c] R. M. Stevenson, R. J. Young, P. See, D. G. Gevaux, K. Cooper, P. Atkinson, I. Farrer, D. A. Ritchie and A. J. Shields. *Phys. Rev. B* **73**, 033306 (2006).
- [Sti97] O. Stier and D. Bimberg. *Phys. Rev. B* **55**, 7726 (1997).
- [Sti99] O. Stier, M. Grundmann and D. Bimberg. *Phys. Rev. B* **59**, 5688 (1999).
- [Sun00] S. J. Sun and Y.-C. Chang. *Phys. Rev. B* **62**, 13631 (2000).
- [Tak00] T. Takagahara. *Phys. Rev. B* **62**, 16840 (2000).
- [Tar04] A. I. Tartakovskii, J. Cahill, M. N. Makhonin, D. M. Whittaker, J.-P. R. Wells, A. M. Fox, D. J. Mowbray, M. S. Skolnick, K. M. Groom, M. J. Steer and M. Hopkinson. *Phys. Rev. Lett.* **93**, 057401 (2004).
- [Tho90] D. B. T. Thoai, Y. Z. Hu and S. W. Koch. *Phys. Rev. B* **42**, 11261 (1990).
- [Tse06] A. Tsekoun, R. Go, M. Pushkarsky, M. Razeghi and C. K. N. Patel. *PNAS* **103**, 4831 (2006).
- [Tsu82] D. C. Tsui, H. L. Störmer and A. C. Gossard. *Phys. Rev. Lett* **48**, 1559 (1982).
- [Val94] F. Valle. *Phys. Rev. B* **49**, 2460 (1994).
- [Vas04] M. I. Vasilevskiy, E. V. Anda and S. S. Makler. *Phys. Rev. B* **70**, 035318 (2004).
- [Ver02] O. Verzelen, R. Ferreira and G. Bastard. *Phys. Rev. Lett.* **88**, 146803 (2002).
- [vK80] K. von Klitzing, G. Dorda and M. Pepper. *Phys. Rev. Lett.* **45**, 494 (1980).
- [vK90] H. W. van Kesteren, E. C. Cosman, W. A. J. A. van der Poel and C. T. Foxon. *Phys. Rev. B* **41**, 5283 (1990).
- [Vog83] P. Vogl, H. P. Hjalmarson and J. D. Dow. *J. Phys. Chem. Solids* **44**, 365 (1983).
- [Wan94] G. Wang, S. Fafard, D. Leonard, J. E. Bowers, J. L. Merz and P. M. Petroff. *Appl. Phys. Lett.* **64**, 2815 (1994).
- [Wan99] L.-W. Wang and A. Zunger. *Phys. Rev. B* **59**, 15806 (1999).
- [Wel86] H. Weller, H. M. Schmidt, U. Koch, A. Fojtik, S. Baral, A. Henglein, W. Kunath, K. Weiss and E. Diemann. *Chem. Phys. Lett.* **124**, 557 (1986).

- [Wer89] J. Werner, E. Kapon, N. G. Stoffel, E. Colas, S. A. Schwarz and N. Andreadakis. *Appl. Phys. Lett.* **55**, 540 (1989).
- [Wil00] A. J. Williamson, L. W. Wang and A. Zunger. *Phys. Rev. B* **62**, 12963 (2000).
- [Win62] W. L. Winterbottom and J. P. Hirth. *J. Chem. Phys.* **37**, 784 (1962).
- [Wog97] U. Woggon. *Optical Properties of Semiconductor Quantum Dots* (Springer Tracts in Modern Physics 136, Springer, Berlin, 1997).
- [Wog03] U. Woggon, D. Miller, F. Kalina, B. Gerlach, D. Kayser, K. Leonardi and D. Hommel. *Phys. Rev. B* **67**, 045204 (2003).
- [Wol01] S. A. Wolf, D. D. Awschalom, R. A. Buhrman, J. M. Daughton, S. von Molnár, M. L. Roukes, A. Y. Chtchelkanova and D. M. Treger. *Science* **294**, 1488 (2001).
- [Xu02] S. Xu, A. A. Mikhailovsky, J. A. Hollingsworth and V. I. Klimov. *Phys. Rev. B* **65**, 045319 (2002).
- [You05] R. J. Young, R. M. Stevenson, A. J. Shields, P. Atkinson, K. Cooper, D. A. Ritchie, K. M. Groom, A. I. Tartakovskii and M. S. Skolnick. *Phys. Rev. B* **72**, 113305 (2005).
- [Yu03] P. Y. Yu and M. Cardona. *Fundamentals of Semiconductors* (Springer Verlag Berlin Heidelberg, 2003).
- [Zib04] E. A. Zibik, L. R. Wilson, R. P. Green, G. Bastard, R. Ferreira, P. J. Phillips, D. A. Carder, J.-P. R. Wells, J. W. Cockburn, M. S. Skolnick, M. J. Steer and M. Hopkinson. *Phys. Rev. B* **70**, 161305(R) (2004).

Acknowledgements

As with any scientific work of the extent of this thesis, many people contributed in various stages of the ongoing research process and I would like to express my gratitude for their support.

- My greatest thanks goes to Professor Dr. Wolfgang Ossau, my advisor, whose knowledge and ingenuity in Physics along with his straight and honest way funneled my efforts into the completion of this work.
- Very special thanks to Dr. Georgy Astakhov, whose deep understanding of optical experiments in general and optics of low-dimensional semiconductor systems in particular have been an inspiration throughout the entirety of this work. Late evenings of measurements and discussions with him form the basic backbone of what you hold in hands.
- My fellow lab mates who have been giving me a hand in the day to day business and made working in the optical spectroscopy group a very enjoyable experience. In chronological order: Helge Hoffman, Sonja Schüler, Jan-Henrik Quast, Jürgen Schwittek and Fanny Greullet.
- Special thanks to Professor Dr. Laurens W. Molenkamp for giving me full access to the truly impressive infrastructure of his chair at all times. Without the critical mass of the EP3 this work could not have been conducted at all.
- A big thank you to the MBE group of the EP3 for the steady supply of high quality samples and the particularly good and uncomplicated communication. Close collaboration with Dr. Suddhasatta Mahapatra, Alexander Frey, Dr. Claus Schumacher and Professor Dr. Karl Brunner was a prerequisite for this work.
- Professor Dr. Jean Geurts, Utz Bass, Christian Kehl, Sven Issing, Marcel Schumm and Martin Kördel from the Raman spectroscopy group of the EP3 for their accompanying work and discussions on phonon scattering in QDs.
- The “Russian mafia” and in particular Dr. Alexei V. Platonov for theoretical advice and input on the phonon relaxation in QDs and the $\mathbf{k}\cdot\mathbf{p}$ -modelling.
- Bastian Büttner, Volkmar Hock, Dr. Tatjana Borzenko and Professor Dr. Georg Schmidt for introducing me to the art of lithographic nano-patterning and general support in the EP3 clean-room labs.

- Roland Ebert, Rainer Brauner, Hans Eggermann and the entire team of the Wissenschaftliche Werkstätten des Physikalischen Instituts for technical input and their craftsmanship whenever I came with something insane that I felt was needed to be part of my experimental setup. Special thanks to Roland Ebert for providing tons of liquid helium at even the most unholy times (this Christmas thing is overrated anyways ...)
- Dr. Charles Gould for proofreading the final version of the manuscript and tracing down typos and stylistic issues that a certain software of a company from Redmond, WA, USA would not find.
- Financial support from the DFG (SFB 410 and OS98/8-1) is gratefully acknowledged.
- My parents for unquestioning support in wherever I may roam.
- Last but not least I wholeheartedly thank my wife Simone for her never ending patience with me. “Taking a day off” and “coming home early tonight” were not exactly phrases commonly met in my everyday vocabulary over the last years and I promise to change that in the future (at least a little bit....honestly!).

Curriculum Vitae

Tobias Kießling

geboren in Würzburg am 12. Dezember 1979

verheiratet, keine Kinder

- September 1986 bis Juli 1990 Besuch der Grundschule Heuchelhof in Würzburg
- September 1990 bis Juni 1999 Besuch des Friedrich-König Gymnasiums in Würzburg
Abschluß Abitur
- September 1999 bis Juli 2000 Grundwehrdienst
AVZ StKpPzBrig 36
AusbUstgVb 1. Kontingent SFOR/KFOR
- Oktober 2000 bis Juli 2003 Studium Physik an der
Julius-Maximilians-Universität, Würzburg
Vordiplom im Oktober 2002
- August 2003 bis September 2004 Studium Physik an der
State University of New York at Buffalo
Abschluß Master of Science
- Januar 2005 bis Dezember 2007 Promotionsstudium
am Physikalischen Institut (Prof. Dr. W. Ossau)
der Julius-Maximilians-Universität, Würzburg
- seit Januar 2008 Wissenschaftlicher Mitarbeiter
am Lehrstuhl EP3 (Prof. Dr. L. W. Molenkamp)
der Julius-Maximilians-Universität, Würzburg

Ehrenwörtliche Erklärung
gemäß §5 Abs. 1 Ziff. 2 und 5
der Promotionsordnung der
Fakultät für Physik und Astronomie
der Universität Würzburg

Hiermit erkläre ich ehrenwörtlich, dass ich die Dissertation selbständig und ohne Hilfe eines Promotionsberaters angefertigt und keine weiteren als die angegebenen Quellen und Hilfsmittel benutzt habe.

Die Dissertation wurde bisher weder vollständig noch teilweise einer anderen Hochschule mit dem Ziel, einen akademischen Grad zu erwerben, vorgelegt.

Am 01. September 2004 wurde mir von der State University of New York at Buffalo der akademische Grad *Master of Science* verliehen. Weitere akademische Grade habe ich weder erworben noch versucht zu erwerben.

Würzburg,

Tobias Kießling

